Astronomy & Astrophysics manuscript no. PlanckMission2013
March 22, 2013

Planck 2013 results. I. Overview of products and scientific results

Planck Collaboration: P. A. R. Ade[93], N. Aghanim[65], C. Armitage-Caplan[99], M. Arnaud[79], M. Ashdown[76,6], F. Atrio-Barandela[20], J. Aumont[65], C. Baccigalupi[92], A. J. Banday[103,11], R. B. Barreiro[72], M. Bartelmann[102,84], J. G. Bartlett[1,74], E. Battaner[105], K. Benabed[66,101], A. Benoît[63], A. Benoit-Lévy[27,66,101], J.-P. Bernard[11], M. Bersanelli[37,55], P. Bielewicz[103,11,92], J. Bobin[79], J. J. Bock[74,12], A. Bonaldi[75], J. R. Bond[9], J. Borrill[15,96], F. R. Bouchet[66,101], F. Boulanger[65], J. W. Bowyer[61], M. Bridges[76,6,69], M. Bucher[1], C. Burigana[54,35], R. C. Butler[54], B. Cappellini[55], J.-F. Cardoso[80,1,66], R. Carr[43], M. Casale[43], A. Catalano[81,78], A. Challinor[69,76,13], A. Chamballu[79,17,65], R.-R. Chary[62], X. Chen[62], L.-Y Chiang[68], H. C. Chiang[29,7], P. R. Christensen[88,40], S. Church[98], D. L. Clements[61], S. Colombi[66,101], L. P. L. Colombo[26,74], F. Couchot[77], A. Coulais[78], B. P. Crill[74,89], A. Curto[6,72], F. Cuttaia[54], L. Danese[92], R. D. Davies[75], R. J. Davis[75], P. de Bernardis[36], A. de Rosa[54], G. de Zotti[51,92], J. Delabrouille[1], J.-M. Delouis[66,101], F.-X. Désert[58], C. Dickinson[75], J. M. Diego[72], H. Dole[65,64], S. Donzelli[55], O. Doré[74,12], M. Douspis[65], J. Dunkley[99], X. Dupac[44], G. Efstathiou[69], T. A. Enßlin[84], H. K. Eriksen[70], E. Falgarone[78], F. Finelli[54,56], S. Foley[45], O. Forni[103,11], M. Frailis[53], E. Franceschi[54], M. Freschi[44], S. Fromenteau[1,65], T. C. Gaier[74], S. Galeotta[53], J. Gallegos[44], B. Gandolfo[45], K. Ganga[1], M. Giard[103,11], G. Giardino[46], Y. Giraud-Héraud[1], J. González-Nuevo[72,92], K. M. Górski[74,107], S. Gratton[76,69], A. Gregorio[38,53], A. Gruppuso[54], J. Haissinski[77], F. K. Hansen[70], D. Hanson[85,74,9], D. Harrison[69,76], G. Helou[12], S. Henrot-Versillé[77], C. Hernández-Monteagudo[14,84], D. Herranz[72], S. R. Hildebrandt[12], E. Hivon[66,101], M. Hobson[6], W. A. Holmes[74], A. Hornstrup[18], W. Hovest[84], K. M. Huffenberger[106], T. R. Jaffe[103,11], A. H. Jaffe[61], J. Jewell[74], W. C. Jones[29], M. Juvela[28], P. Kangaslahti[74], E. Keihänen[28], R. Keskitalo[24,15], T. S. Kisner[83], R. Kneissl[42,8], J. Knoche[84], L. Knox[31], M. Kunz[19,65,3], H. Kurki-Suonio[28,49], G. Lagache[65], A. Lähteenmäki[2,49], J.-M. Lamarre[78], A. Lasenby[6,76], R. J. Laureijs[46], C. R. Lawrence[74], M. Le Jeune[1], S. Leach[92], J. P. Leahy[75], R. Leonardi[44], J. León-Tavares[47,2], C. Leroy[65,103,11], J. Lesgourgues[100,91], M. Liguori[34], P. B. Lilje[70], M. Linden-Vørnle[18], M. López-Caniego[72], S. Lowe[75], P. M. Lubin[32], J. F. Macías-Pérez[81], B. Maffei[75], D. Maino[37,55], N. Mandolesi[54,5,35], M. Maris[53], D. J. Marshall[79], P. G. Martin[9], E. Martínez-González[72], S. Masi[36], S. Matarrese[34], F. Matthai[84], P. Mazzotta[39], A. McDonald[45], P. McGehee[62], P. R. Meinhold[32], A. Melchiorri[36,57], J.-B. Melin[17], L. Mendes[44], A. Mennella[37,55], M. Migliaccio[69,76], R. Miniscalco[45], S. Mitra[60,74], M.-A. Miville-Deschênes[65,9], A. Moneti[66], L. Montier[103,11], G. Morgante[54], D. Mortlock[61], A. Moss[94], D. Munshi[93], J. A. Murphy[87], P. Naselsky[88,40], F. Nati[36], P. Natoli[35,4,54], C. B. Netterfield[22], H. U. Nørgaard-Nielsen[18], C. North[93], F. Noviello[75], D. Novikov[61], I. Novikov[88], I. J. O'Dwyer[74], S. Osborne[98], C. A. Oxborrow[18], F. Paci[92], L. Pagano[36,57], F. Pajot[65], R. Paladini[62], D. Paoletti[54,56], B. Partridge[48], F. Pasian[53], G. Patanchon[1], D. Pearson[74], T. J. Pearson[12,62], O. Perdereau[77], L. Perotto[81], F. Perrotta[92], F. Piacentini[36], M. Piat[1], E. Pierpaoli[26], D. Pietrobon[74], S. Plaszczynski[77], P. Platania[73], E. Pointecouteau[103,11], G. Polenta[4,52], N. Ponthieu[65,58], L. Popa[67], T. Poutanen[49,28,2], G. W. Pratt[79], G. Prézeau[12,74], S. Prunet[66,101], J.-L. Puget[65], J. P. Rachen[23,84], W. T. Reach[104], R. Rebolo[71,16,41], M. Reinecke[84], M. Remazeilles[65,1], C. Renault[81], S. Ricciardi[54], T. Riller[84], I. Ristorcelli[103,11], G. Rocha[74,12], C. Rosset[1], M. Rossetti[37,55], G. Roudier[1,78,74], M. Rowan-Robinson[61], J. A. Rubiño-Martín[71,41], B. Rusholme[62], E. Salerno[10], M. Sandri[54], D. Santos[81], G. Savini[90], D. Scott[25], M. D. Seiffert[74,12], E. P. S. Shellard[13], G. F. Smoot[30,83,1], L. D. Spencer[93], J.-L. Starck[79], V. Stolyarov[6,76,97], R. Stompor[1], R. Sudiwala[93], R. Sunyaev[84,95], F. Sureau[79], D. Sutton[69,76], A.-S. Suur-Uski[28,49], J.-F. Sygnet[66], J. A. Tauber[46] *, D. Tavagnacco[53,38], D. Taylor[43], L. Terenzi[54], D. Texier[43], L. Toffolatti[21,72], M. Tomasi[55], M. Tristram[77], M. Tucci[19,77], J. Tuovinen[86], M. Türler[59], M. Tuttlebee[45], G. Umana[50], L. Valenziano[54], J. Valiviita[49,28,70], B. Van Tent[82], J. Varis[86], L. Vibert[65], P. Vielva[72], F. Villa[54], N. Vittorio[39], L. A. Wade[74], B. D. Wandelt[66,101,33], R. Watson[75], C. Watson[45], M. White[30], S. D. M. White[84], A. Wilkinson[75], D. Yvon[17], A. Zacchei[53], and A. Zonca[32]

(Affiliations can be found after the references)

Received XX, 2012; accepted XX, 2013

ABSTRACT

The European Space Agency's *Planck* satellite, dedicated to studying the early universe and its subsequent evolution, was launched on 14 May 2009 and has been surveying the microwave and submillimetre sky continuously since August 2009. In March 2013, ESA and the *Planck* Collaboration publicly released the initial cosmology products based on the the first 15.5 months of Planck operations, along with a set of scientific and technical papers and a web-based explanatory supplement. This paper describes the mission and its performance, and gives an overview of the processing and analysis of the data, the characteristics of the data, the main scientific results, and the science data products and papers in the release. The science products include a set of specialized maps of the cosmic microwave background, maps of Galactic and extragalactic extended foregrounds, a catalogue of compact Galactic and extragalactic sources, and a list of sources detected through the Sunyaev-Zeldovich effect. The likelihood code used to assess cosmological models against the *Planck* data and a lensing likelihood are described. Scientific results include robust support for the standard, six parameter ΛCDM model of cosmology and improved measurements for the parameters that define this model, including a highly significant deviation from scale invariance of the primordial power spectrum. The *Planck* values for some of these parameters and others derived from them are significantly different from those previously determined. Several large scale anomalies in the CMB temperature distribution detected earlier by *WMAP* are confirmed with higher confidence. *Planck*sets new limits on the number and mass of neutrinos, and has measured gravitational lensing of CMB anisotropies at 25σ. *Planck* finds no evidence for non-Gaussian statistics of the CMB anisotropies. There is some tension between *Planck* and *WMAP* results; this is evident in the power spectrum and results for some of the cosmology parameters. In general, Planck results agree well with results from the measurements of baryon acoustic oscillations. Because the analysis of Planck polarization data is not yet as mature as the analysis of temperature data, polarization results are not released. We do, however, graphically illustrate the robust detection of the E-mode polarization signal around CMB hot- and cold-spots.

Key words. Cosmology: observations — Cosmic background radiation — Surveys — Space vehicles: instruments — Instrumentation: detectors

1. Introduction

The *Planck* satellite[1] (Tauber et al. 2010a; Planck Collaboration I 2011) was launched on 14 May 2009, and has been scanning the sky stably and continuously since 12 August 2009. *Planck* carries a scientific payload consisting of an array of 74 detectors sensitive to a range of frequencies between ∼ 25 and ∼ 1000 GHz, which scan the sky simultaneously and continuously with an angular resolution varying between ∼30 arcminutes at the lowest frequencies and ∼5′ at the highest. The array is arranged into two instruments. The detectors of the Low Frequency Instrument (LFI; Bersanelli et al. 2010; Mennella et al. 2011) are pseudo-correlation radiometers, covering three bands centred at 30, 44, and 70 GHz. The detectors of the High Frequency Instrument (HFI; Lamarre et al. 2010; Planck HFI Core Team 2011a) are bolometers, covering six bands centred at 100, 143, 217, 353, 545 and 857 GHz. The design of *Planck* allows it to image the whole sky twice per year, with an combination of sensitivity, angular resolution, and frequency coverage never before achieved. The *Planck* satellite, its payload, and its performance as predicted at the time of launch, are described in 13 articles included in a special issue (Volume 520) of Astronomy & Astrophysics.

The main objective of *Planck*, defined in 1995, is to measure the spatial anisotropies of the temperature of the cosmic microwave background (CMB), with an accuracy set by fundamental astrophysical limits. Its level of performance was designed to enable *Planck* to extract essentially all the cosmological information embedded in the CMB temperature anisotropies. *Planck* was also designed to measure, to high accuracy, the polarization of the CMB anisotropies, which encodes not only a wealth of cosmological information, but also provides a unique probe of the early history of the Universe during the time when the first stars and galaxies formed. Finally, the *Planck* sky surveys produce a wealth of information on the properties of extragalactic sources and on the dust and gas in our own galaxy (see Fig. 1). The scientific objectives of *Planck* are described in detail in Planck Collaboration (2005). The results presented here and in a series of accompanying papers (see Fig. 2) have already allowed *Planck* to achieve many of its planned science goals.

This paper presents an overview of the main data products and associated scientific results of *Planck*'s second release[2], which covers data acquired in the period 12 August 2009 to 27 November 2010. In this Introduction, we briefly summarize some of these results, then return to discuss some of them in Sects. 7 and 8 below.

* Corresponding author: J. A. Tauber, jtauber@rssd.esa.int

[1] *Planck (http://www.esa.int/Planck)* is a project of the European Space Agency – ESA – with instruments provided by two scientific consortia funded by ESA member states (in particular the lead countries: France and Italy) with contributions from NASA (USA), and telescope reflectors provided in a collaboration between ESA and a scientific consortium led and funded by Denmark.

[2] In January of 2011, ESA and the *Planck* Collaboration released to the public a first set of scientific data, the Early Release Compact Source Catalogue (ERCSC), a list of unresolved and compact sources extracted from the first complete all-sky survey carried out by *Planck* (Planck Collaboration VII (2011)). At the same time, initial scientific results related to astrophysical foregrounds were published in a special issue of Astronomy and Astrophysics (Vol 520, 2011). Since then, 12 "Intermediate" papers have been submitted for publication to A&A containing further astrophysical investigations by the Collaboration.

1.1. Overview of 2013 Planck science results

Cosmology— A major goal of the *Planck* experiment is to determine with great precision the key cosmological parameters describing our Universe. A combination of high sensitivity, high angular resolution, and wide frequency coverage makes *Planck* ideal for this task. In particular, *Planck* is able to measure anisotropies on intermediate and small angular scales over the whole sky much more accurately than previous experiments. This translates directly into improved constraints on individual parameters, and the breaking of degeneracies between combinations of other parameters. *Planck*'s sensitivity and angular resolution also make the analysis less reliant on supplementary astrophysical data than that of previous CMB experiments. Our measurements of the cosmological parameters are presented and discussed in Sect. 9 and in Planck Collaboration XVI (2013).

The Universe observed by *Planck* is well-fit by a six parameter ΛCDM model, and we provide strong constraints on deviations from this model. The values of key parameters in this model are summarized in Table 9. In some cases we find significant changes compared to previous measurement, as discussed in detail in Planck Collaboration XVI (2013).

With the *Planck* data, we: (a) firmly establish a deviation from scale invariance for primordial matter perturbations, a key indicator of cosmic inflation; (b) detect with high significance lensing of the CMB by intervening matter, providing evidence for dark energy from the CMB alone; (c) find no evidence for significant deviations from Gaussianity in the statistics of CMB anisotropies; (d) find a low value of the Hubble constant, in tension with the value derived from the standard distance ladder; (e) find a deficit of power at low-ℓs with respect to our best-fit model; (f) confirm the anomalies at large angular scales first detected by *WMAP*; and (g) establish the number of neutrino species at three.

In summary, the *Planck* data are in remarkable accord with a flat ΛCDM model; however, there are tantalizing hints of tensions both internal to the *Planck* data and with other data sets. While such tensions are model-dependent, none of the extensions of the ΛCDM cosmology we explored resolve them. It is to be hoped that more data and further analysis will shed light on these areas of tension. Along these lines, we expect significant improvement in data quality and the level of systematic error control, plus the addition of polarization data, from *Planck* in the near future.

A more extensive summary of science results is given in Sect. 9.

Foregrounds—The astrophysical foregrounds measured by *Planck* hold a huge interest in their own right. The first foreground to be removed from the *Planck* frequency maps is compact and point-like sources, consisting mainly of extragalactic infrared and radio sources, and we release a catalogue of these sources. In addition, we provide an all-sky catalogue of sources detected via the Sunyaev-Zeldovich (SZ) effect, which will become the reference for studies of SZ-detected galaxy clusters.

Seven types of unresolved foregrounds must be removed or controlled for CMB analysis: dust thermal emission; dust anomalous emission (likely due to spinning tiny grains); CO rotational emission lines (significant in at least three HFI bands); free-free emission; synchrotron emission; the cosmic infrared background (CIB); and SZ secondary CMB distortion. For cosmological purposes we achieve robust separation of the CMB from foregrounds using only *Planck* data with multiple independent methods. We release maps of: thermal dust + residual

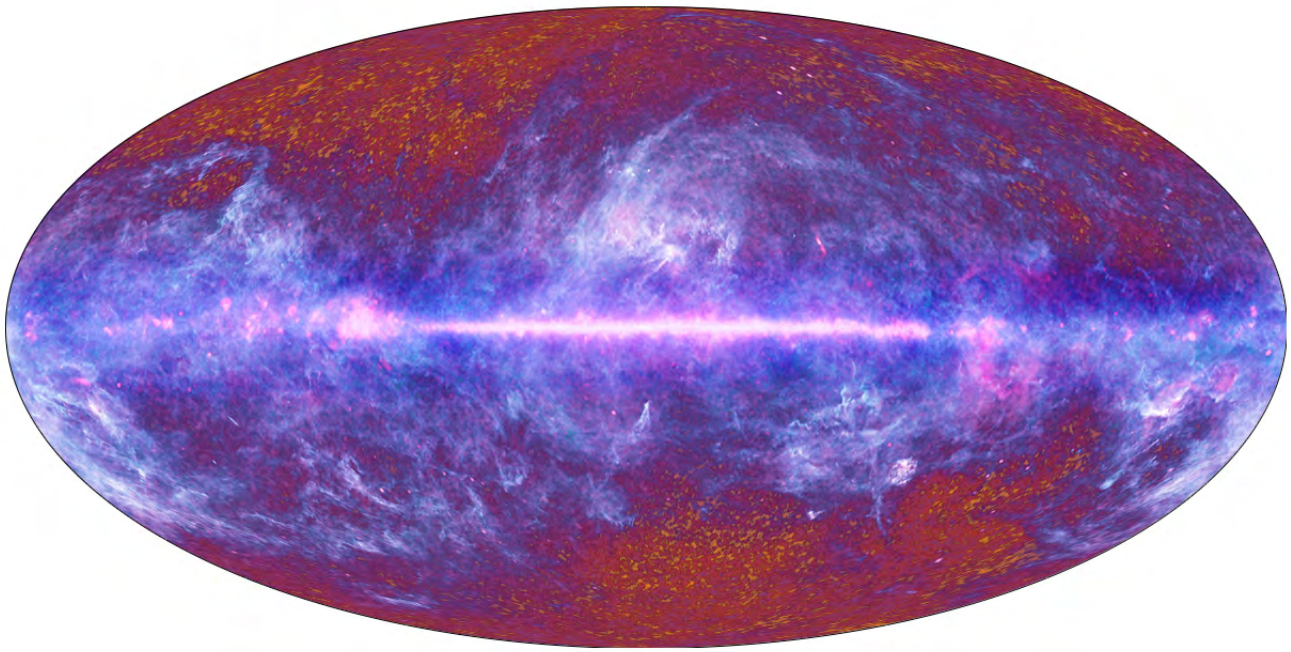

Fig. 1. The image of the entire sky released by *Planck* in 2010 is a composite of all the data gathered over the first nine months of the mission, and illustrates artistically the multitude of Galactic, extragalactic, and cosmological components that contribute to the radiation detected by its payload.

fluctuations of the cosmic infrared background; integrated emission of carbon monoxide; and synchrotron + free-free + spinning dust emission. They will provide a rich source for studies of the interstellar medium. Other maps are released that use ancillary data in addition to the *Planck* data to achieve more physically meaningful analysis.

These products are described in Sect. 8.

1.2. Features and strengths of the Planck mission

Planck has an unprecedented combination of sensitivity, angular resolution, and frequency coverage. For example, the *Planck* detector array at 143 GHz has instantaneous sensitivity and angular resolution 25 and 3 times better, respectively, than the *WMAP* V band (Bennett et al. 2003; Hinshaw et al. 2012a). Considering the final mission durations (9 years for *WMAP*, 29 months for *Planck* HFI, and an expected 50 months for *Planck* LFI), the white noise at map level is 12 times lower at 143 GHz for the same resolution. In harmonic space, the noise level in *Planck* power spectra is two orders of magnitude lower than in those of *WMAP* at angular scales where beams are unimportant ($\ell < 700$ for *WMAP* and 2500 for *Planck*). *Planck* measures 2.6 times as many independnt ℓ's as *WMAP*, corresponding to 6.8 times as many independent modes (l, m) when comparing the same leading CMB channels for the two missions. This increase in angular resolution and sensitivity results in a large gain for analysis of CMB non-Gaussianity and cosmological parameters. In addition, *Planck* has a large overlap in ℓ with the high resolution ground-based experiments ACT (Sievers et al. 2013) and SPT (Keisler et al. 2011). The noise spectra of SPT and *Planck* cross at around $\ell \sim 2000$, allowing an excellent check of the relative calibrations and transfer functions.

Increased sensitivity places *Planck* in a new situation. Earlier satellite (*COBE*/DMR (Smoot et al. 1992), *WMAP* (Bennett et al. 2012)) experiments were limited by detector noise more than by systematic effects and foregrounds. Recent ground-based and balloon-borne experiments ongoing or under development (e.g., ACT (Kosowsky 2003), SPT (Ruhl et al. 2004), SPIDER (Fraisse et al. 2011), EBEX (Reichborn-Kjennerud et al. 2010)), have far larger numbers of detectors and higher angular resolution than *Planck* but can survey only a fraction of the sky over a limited frequency range. They are therefore sensitive to foregrounds or limited to analysing only the cleanest regions of the sky. Considering the impact of cosmic variance, Galactic foregrounds are not a serious limitation for CMB temperature-based cosmology at the largest spatial scales over a limited part (<0.5) of the sky. Diffuse Galactic emissions have steep frequency and angular spectra, and are very bright at frequencies below 70 and above 143 GHz at low spatial frequencies. At small angular scales, extragalactic foregrounds such as unresolved compact sources (including the SZ effect from galaxy clusters and diffuse hot gas) and the correlated CIB, become important and cannot be ignored when carrying out CMB cosmology studies. *Planck*'s all-sky wide-frequency coverage becomes a key factor in this context, allowing it to measure these foregrounds and remove them to below intrinsic detector noise levels, but the contribution of higher resolution experiments to resolve foregrounds is also very important.

When detector noise is very low, systematic effects that arise from the instrument, telescope, scanning strategy, or calibration approach may dominate over noise in specific spatial, frequency, and/or ℓ ranges. The analysis of redundancy is the main tool used by *Planck* to understand and quantify the effect of systematics. Redundancy on short timescales comes from the scanning strategy — spinning at 1 rpm with the spin axis fixed for 45–80 minutes, depending on phase in the year — which has particular advantages in this respect, especially for the largest scales. When first designed, this strategy was considered ambitious because it required low $1/f$ noise near 0.0167 Hz (the spin frequency), and very stable instruments over the whole mission.

Redundancy on long timescales comes in two versions: 1 *Planck* scans approximately the same circle on the sky every six months, alternating in the direction of the scan; and 2 *Planck* scans exactly (within arcminutes) the same circle on the sky every one year. The ability to compare maps made in individual all-sky "surveys" (i.e., covering approximately six month intervals) and year-by-year is invaluable in identifying specific systematic effects and calibration errors. Although *Planck* was designed to cover the whole sky twice over, its superb in-flight performance has enabled it to complete nearly five full-sky maps with the HFI instrument, and it will complete eight full-sky maps with the LFI instrument later in 2013. The redundancy provided by such a large number of surveys is a major asset for *Planck*, allowing tests of the overall stability of the instruments over the mission and sensitive measurements of systematic residuals on the sky.

Redundancy of a different sort is provided by multiple detectors within frequency bands. HFI includes four independent pairs of polarization-sensitive detectors in each channel from 100 to 353 GHz, in addition to the four total intensity (spider web) detectors at all frequencies except at 100 GHz. The LFI includes six independent pairs of polarization-sensitive detectors at 70 GHz, with three at 44 GHz and two at 30 GHz. The different technologies used in the two instruments provide an additional powerful tool to identify and remove systematic effects.

Overall, the combination of scanning strategy and instrumental redundancy has allowed identification and removal of most systematic effects affecting CMB temperature measurements. This can be seen in the fact that additional surveys have led to significant improvements, at a rate greater than the square root of the integration time, in the signal-to-noise ratio achieved in the combined maps. Given that the two instruments have achieved their expected intrinsic sensitivity, and that most systematics have been brought below the noise (detector or cosmic variance) for intensity, it is a fact that temperature-based cosmology based on the *Planck* data is already being limited by the foregrounds, fulfilling one of the main objectives of the mission.

1.3. Status of Planck polarization measurements

The situation for CMB polarization, whose amplitude is typically 4 % of intensity, is less mature. At present *Planck*'s sensitivity to the CMB polarization power spectrum at low multipoles ($\ell < 20$) is significantly limited by residual systematics that are of a different nature than those of temperature because polarization measurement with *Planck* requires differencing between detector pairs. Furthermore, the component separation problem is different, on the one hand simpler because only three polarized foregrounds have been identified so far (diffuse synchrotron emission, thermal dust emission, and radio sources), on the other hand more complicated because the foregrounds are more highly polarized than the CMB, and therefore more dominant over a larger fraction of the sky. Moreover, no external templates of the polarized foregrounds exist. These factors are currently restricting *Planck*'s ability to meet its most ambitious goals, e.g., to measure or set stringent upper limits on cosmological B-mode amplitudes. Although this situation is being improved at the present time, the possibility remains that these effects will be the final limitation for cosmology using the polarized *Planck* data. The situation is much better at high multipoles where the polarization data are already close to being limited by the intrinsic detector noise.

These considerations have led to the strategy adopted by the *Planck* Collaboration for this first release of maps and associated science results, which concentrates on temperature mainly, using polarization data only as a validity check of the best cosmological model derived from temperature data. The signal-to-noise of CMB temperature anisotropies (including cosmic variance) is large enough in the best half of the sky that, for the estimation of CMB power spectra and the estimation of cosmological parameters, we can adopt a likelihood analysis at high multipoles that uses the cross-power spectra of individual detectors as inputs, simultaneously estimating the amplitude of remaining extragalactic foregrounds and other "nuisance parameters" (e.g., systematic effects, cross calibration) at the power spectrum level. For low multipoles, the likelihood estimation is based on a low-resolution CMB map obtained over a limited fraction of the sky by a component separation technique at map level. The analysis of CMB non-Gaussianity instead requires a clean high-resolution map over a fraction of the sky as large as possible, and for this purpose only we carry out a specific component separation exercise at map level at full resolution and on a large part of the sky.

Considering that the work on reduction of systematics for polarization is still unfinished, we use the *WMAP* polarization likelihood in addition to the *Planck* temperature likelihood at both low and high ℓ. This constrains τ_{reion}.

At high multipoles, the good quality of the *Planck* polarization data is well illustrated (see Sect. 9.3) by the use of stacking techniques on the peaks and troughs of the CMB intensity. This allows a direct and spectacular visualization of the E polarization induced by matter oscillating in the potential well of dark matter at recombination, illustrating the unprecedented power of *Planck* in polarization. A more complete cosmological analysis using the full data set, including polarization, will be published with the second major release of maps to take place in 2014.

Finally, we also note that the sensitivity and accuracy of *Planck*'s polarized maps is already well beyond that of any previous survey in this frequency range, and allows very new scientific investigations of diffuse Galactic polarized emissions and the magnetic fields that induce them. A preview of forthcoming publications is provided in Sect. 8.2.4.

2. Data products in the 2013 release

The 2013 distribution of released products, which can be freely accessed via the *Planck* Legacy Archive interface[3], is based on the data acquired by *Planck* during its "nominal" operations period from 12 August 2009 to 27 November 2010, and comprises:

- Maps of the sky at nine frequencies (Sect. 6).
- Many additional products that serve to quantify the characteristics of the maps to a level adequate for the science results being presented, such as noise maps, masks, instrument characteristics, etc.
- Three high-resolution maps of the CMB sky and accompanying characterization products (Section 7.1). Non-Gaussianity results are based on one of the maps; the others demonstrate the robustness of the results and their insensitivity to different methods of analysis.
- A low-resolution CMB map (Section 7.1) used in the low ℓ likelihood code, with an associated set of foreground maps produced in the process of separating the low-resolution CMB from foregrounds, with accompanying characterization products.

[3] *h*ttp://www.sciops.esa.int/index.php?project=planck&page=Planck_Legacy_

- Maps of foreground components at high resolution, including: thermal dust + residual CIB; CO; synchrotron + free-free + spinning dust emission, and maps of dust temperature and opacity (Section 8).
- A likelihood code and data package used for testing cosmological models against the *Planck* data including both the CMB (Section 7.3.1) and CMB lensing (Section 7.3.2) . The CMB part is based at $\ell < 50$ on the low-resolution CMB map just described and on the WMAP9 V-band polarized map (to fix τ), and at high ℓ on cross-power spectra of individual detector sets. The lensing part is based on the 143 and 217 GHz maps.
- The *Planck* Catalogue of Compact Sources (PCCS, Section 8.1.1), comprising lists of compact sources over the entire sky at the nine *Planck* frequencies.
- The *Planck* Catalogue of Sunyaev-Zeldovich Sources (PSZ, Section 8.1.2), comprising a list of sources detected by their SZ distortion of the CMB spectrum.

3. Papers accompanying the 2013 release

The characteristics, processing, and analysis of the *Planck* data as well as a number of scientific results are described in a series of papers released simultaneously with the data. The titles of the papers begin with "*Planck* 2013 results.", followed by the specific titles below. Figure 2 gives a graphical view of the papers, divided into product, processing, and scientific result categories.

I. Overview of products and results (*this paper*)
II. Low Frequency Instrument data processing
III. LFI systematic uncertainties
IV. LFI beams
V. LFI calibration
VI. High Frequency Instrument data processing
VII. HFI time response and beams
VIII. HFI calibration and mapmaking
IX. HFI spectral response
X. HFI energetic particle effects
XI. Consistency of the data
XII. Component separation
XIII. Galactic CO emission
XIV. Zodiacal emission
XV. CMB power spectra and likelihood
XVI. Cosmological parameters
XVII. Gravitational lensing by large-scale structure
XVIII. The gravitational lensing-infrared background correlation
XIX. The integrated Sachs-Wolfe effect
XX. Cosmology from Sunyaev-Zeldovich cluster counts
XXI. All-sky Compton-parameter map and characterization
XXII. Constraints on inflation
XXIII. Isotropy and statistics of the CMB
XXIV. Constraints on primordial non-Gaussianity
XXV. Searches for cosmic strings and other topological defects
XXVI. Background geometry and topology of the Universe
XXVII. Special relativistic effects on the CMB dipole
XXVIII. The Planck Catalogue of Compact Sources
XXIX. The Planck catalogue of Sunyaev-Zeldovich sources

In the next few months additional papers will be released concentrating on Galactic foregrounds in both temperature and polarization.

This paper contains an overview of the main aspects of the *Planck* project that have contributed to the 2013 release, and points to the papers (Fig. 2) that full descriptions. It proceeds in the following way:

- Section 4 summarizes the operations of *Planck* and the performance of the spacecraft and instruments.
- Sections 5 and 6 describe the processing steps carried out in the generation of the nine *Planck* frequency maps and their characteristics.
- Section 7 describes the *Planck* 2013 products related to the Cosmic Microwave Background, namely the CMB maps, the lensing products, and the likelihood code.
- Section 8 describes *Planck*'s 2013 astrophysical products, namely catalogues of compact sources, and maps of diffuse foreground emission.
- Section 9 describes the main cosmological science results based on the 2013 CMB products.
- Section 10 concludes with a summary and a look towards the next generation of *Planck* products.

4. The *Planck* mission

Planck was launched from Kourou, French Guiana, on 14 May 2009 by an Ariane 5 ECA launcher, together with the *Herschel* Space Observatory. After separation from the rocket and from *Herschel*, *Planck* followed a trajectory to the L_2 point of the Sun-Earth system, eventually being injected into a ~6-month Lissajous orbit around it. By early July 2009, *Planck* was in its final orbit (Fig. 3). Once in its final orbit, small manoeuvres are required at approximately monthly intervals (totalling ~1 m/s per year) to keep *Planck* from drifting away from L_2.

The first two months of operations focused on commissioning activities, during which *Planck* cooled down to the oprating temperatures of the coolers and the instruments. Calibration and verification activities (CPV phase) started during commissioning and ended on 12 August 2009 when routine operations and science observations began. More detailed information about the first phases of operations may be found in Planck Collaboration I (2011) and Planck Collaboration ES (2013).

4.1. Scanning strategy

Planck spins at 1 rpm about the symmetry axis of the spacecraft. The spin axis follows a cycloidal path across the sky in step-wise displacements of 2′ (Fig. 4). Since the projected position of the spin axis onto the ecliptic plane must advance steadily in longitude, the time interval between two manoeuvres varies between 2360 s and 3904 s. Details of the scanning strategy are given in Tauber et al. (2010a) and Planck Collaboration I (2011)).

The fraction of time used by the manoeuvers themselves (typical duration of five minutes) varies between 6 % and 12 %, depending on the phase of the cycloid. At present, the reconstructed position of the spin axis during manoeuvers has not been determined accurately enough for scientific work (but see Section 4.5), and the data taken during manoeuvers are not used in the analysis. Over the nominal mission, the total reduction of scientific data due to manoeuvers was 9.2 %.

The boresight of the telescope is 85° away from the spin axis. As *Planck* spins, the instrument beams cover nearly great circles in the sky. The spin axis remains fixed (except for a small drift

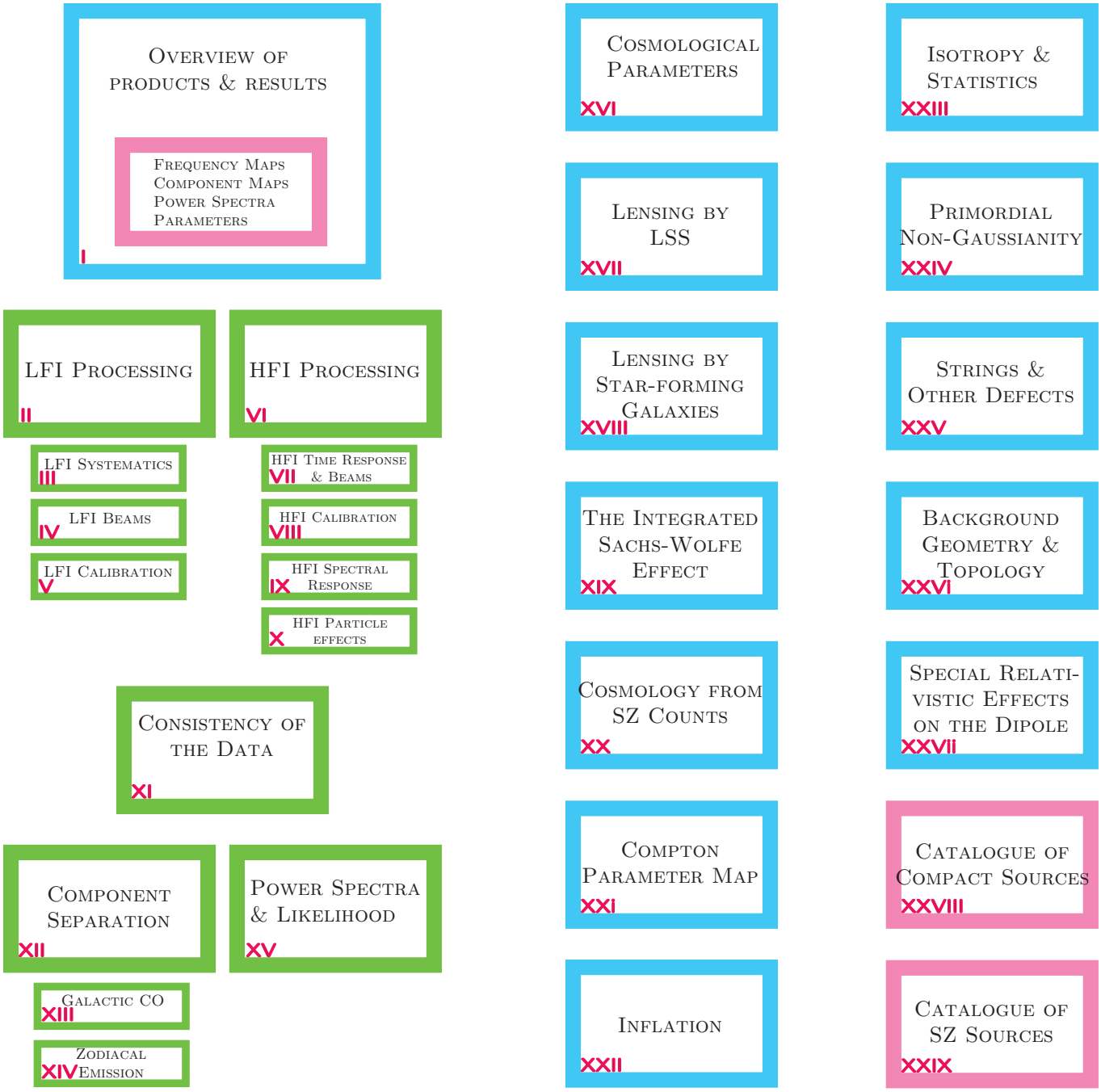

Fig. 2. The *Planck* papers published simultaneously with the release of the 2013 products. The title of each paper is abbreviated. The roman numerals correspond to the sequence number assigned to each of the papers in the series; references include this number. Green boxes refer to papers describing aspects of data processing and the 2013 *Planck* products. Blue boxes refer to papers mainly dedicated to scientific analysis of the products. Pink boxes describe specific 2013 *Planck* products.

due to solar radiation pressure) for between ~39 and ~65 spins (corresponding to the dwell times given above), depending on which part of the cycloid *Planck* is in. To high accuracy, any one beam covers precisely the same sky between 39 and 65 times. The set of observations made during a period of fixed spin axis pointing is often referred to as a "ring." This redundancy plays a key role in the analysis of the data, as will be seen below, and is an important feature of the scan strategy.

As the Earth and *Planck* orbit the Sun, the nearly-great circles that are observed rotate about the ecliptic poles. The amplitude of the spin-axis cycloid is chosen so that all beams of both instruments cover the entire sky in one year. In effect, *Planck* "tilts" to cover first one Ecliptic pole, then tilts the other way to cover the other pole six months later. If the spin axis stayed exactly on the ecliptic plane, the telescope boresight was perpendicular to the spin axis, the Earth was in a precisely circular orbit, and *Planck* had only one detector with a beam aligned precisely with the telescope boresight, that beam would cover the full sky in six months. In the next six months, it would cover the same sky, but with the opposite sense of rotation on a given great circle. However, since the spin axis is steered in a cycloid, the telescope is 85° to the spin axis, the focal plane is degrees wide, and the Earth's orbit is slightly elliptical, the symmetry of the scanning is (slightly) broken.

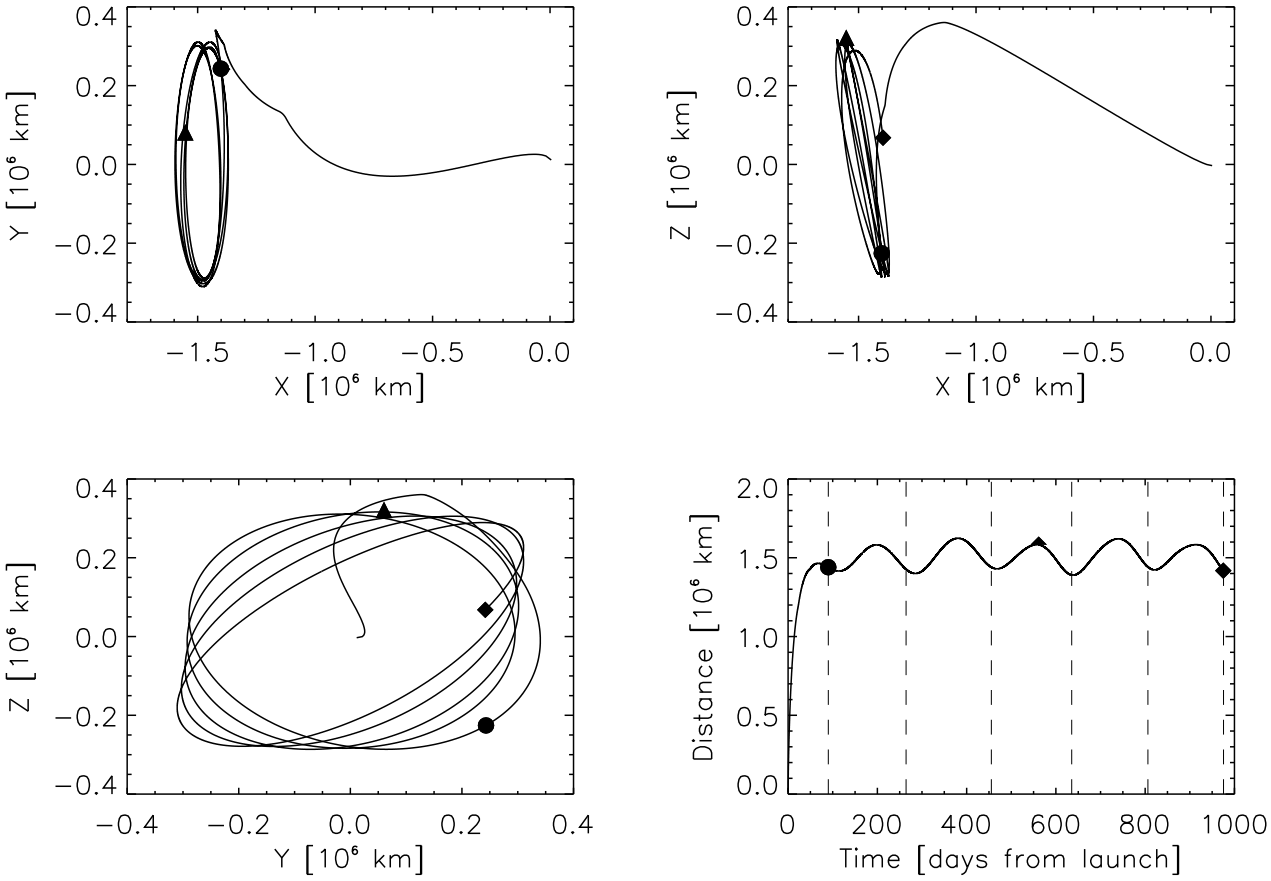

Fig. 3. The trajectory of *Planck* from launch until 13 January 2012, in Earth-centred rotating coordinates (X is in the Sun-Earth direction, and Z points to the North Ecliptic Pole). The symbols indicate the start of routine operations, the end of the nominal mission, and the end of HFI data acquisition. The orbital periodicity is ~ 6 months. The distance from the Earth-Moon barycentre is shown at bottom right together with survey boundaries.

Thus the *Planck* beams scan the entire sky exactly twice in one year, but scan only about 95 % of the sky in six months. For convenience, we call an approximately six month period a "survey" (see Table 1), and use it as a shorthand for one coverage of the sky. It is important to remember, however, that as long as the phase of the cycloid remains constant, one year corresponds to exactly two coverages of the sky, while one survey has a less exact meaning. Null tests between 1-year periods with the same cycloid phase are extremely powerful. Null tests between surveys are useful for many types of tests, but they have some limitations.

4.2. Routine scanning operations

Routine operations started on 12 August 2009. The start and end dates of each survey (as defined above) are listed in Table 1, which also shows the fraction of the sky covered by all frequencies in each of them. The fourth survey was shortened in order to start earlier with a slightly different scanning strategy (adopted for Surveys 5-8, see below). The coverage of the fifth survey is smaller than the others due to gaps in the coverage from time spent in "deep rings".

During routine scanning, the *Planck* instruments naturally observe objects of special interest for calibration purposes. These include Mars, Jupiter, Saturn, Uranus, and Neptune, as well as the Crab Nebula for calibration of polarizers. Different types of observations of these objects have been performed during the routine phase of the mission. These include:

- Normal scans on Solar System objects and the Crab Nebula for calibration purposes. The complete list of scanning dates of these objects can be found in Planck Collaboration ES (2013).
- "Deep rings." These special observations are performed on each passage of Jupiter and the Crab Nebula, from January 2012 onward. They consist of deeply and finely (step 0.′5) sampled observations with the spin axis along the Ecliptic plane, lasting typically two to three weeks. Since the Crab is crucial for calibration of both instruments, the average longitudinal speed of the pointing steps was increased before scanning the Crab, to improve operational margins and ease recovery in case of problems.
- "Drift scans." These special observations are performed on Mars, making use of its proper motion. They allow finely-samples measurements of the beams, particularly for HFI. The rarity of Mars observations during the mission gives them high priority.

At the end of the fourth Survey, the phase of the cycloid was shifted by 90°, modifying the scanning directions throughout the sky in such a way that the combination of surveys before and after the change improved the range of polarizer angles on the sky,

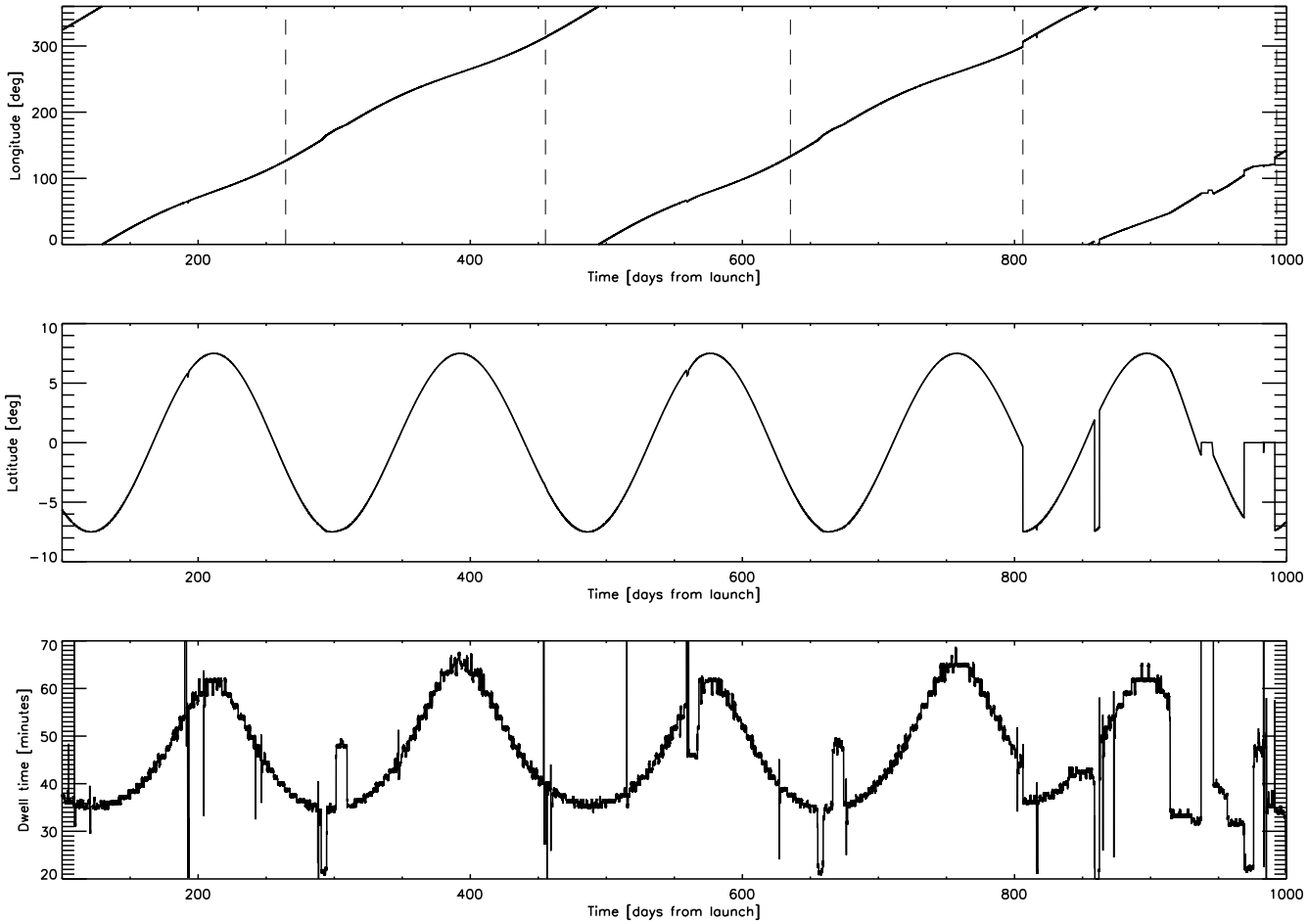

Fig. 4. Top two panels: the path of the spin axis of *Planck* (in ecliptic longitude and latitude) over the period 12 August 2009 to 13 January 2012. Bottom: the evolution of the dwell time during the same period. Periods of acceleration/deceleration (e.g., around observations of the Crab) are clearly visible as symmetric temporary increases and reductions of dwell time. Survey boundaries are indicated in the upper plot. The change in cycloid phase is clearly visible at operational day (OD) 807. The disturbances around OD 950 are due to the "spin-up campaign".

Table 1. *Planck* "surveys" (see Sect. 4.1 for the definition of a survey).

Survey	Instrument	Beginning	End	Coverage[a]
1	LFI & HFI	12 August 2009 (14:16:51 UT)	2 February 2010 (20:51:04 UT)	93.1 %
2	LFI & HFI	2 February 2010 (20:54:43)	12 August 2010 (19:27:20 UT)	93.1 %
3[b]	LFI & HFI	12 August 2010 (19:30:44)	8 February 2011 (20:55:55 UT)	93.1 %
4	LFI & HFI	8 February 2011 (20:59:10)	29 July 2011 (17:13:32)	86.6 %
5[c]	LFI & HFI	29 July 2011 (18:04:49)	1 February 2012 (05:26:29 UT)	80.1 %
6	LFI	14 January 2012	July 2012	
7	LFI	July 2012	Jan 2013	
8	LFI	Jan 2013	August 2013	

[a] Fraction of the sky covered by all frequencies
[b] End of Nominal period = 28 November 2010 (12:00:53 UT)
[c] End of data acquisition with HFI = 13 January 2012 (14:54:07 UT)

therefore helping in the treatment of systematic effects and improving polarization calibration. This change in scanning strategy applies to Surveys 5–8.

The set of products being delivered at the time this paper is submitted (referred to hereafter as the "2013 products") are based on the so-called "nominal mission", which ended on 28 November 2010 and includes 15.5 months of data acquired during Surveys 1, 2, and part of 3.

The HFI bolometers stopped producing useful scientific data on 13 January 2012 when the on-board supply of ^{3}He needed to cool them to 0.1 K ran out. This date marks the end of operations of the full payload of *Planck*. However, LFI continues to operate and acquire scientific data from the sky. The end of *Planck* operations is expected in the autumn of 2013. Data from the remaining part of Survey 3, Surveys 4 and 5 (both LFI and HFI), and Surveys 6–8 (LFI only) are being processed and will be released in 2014.

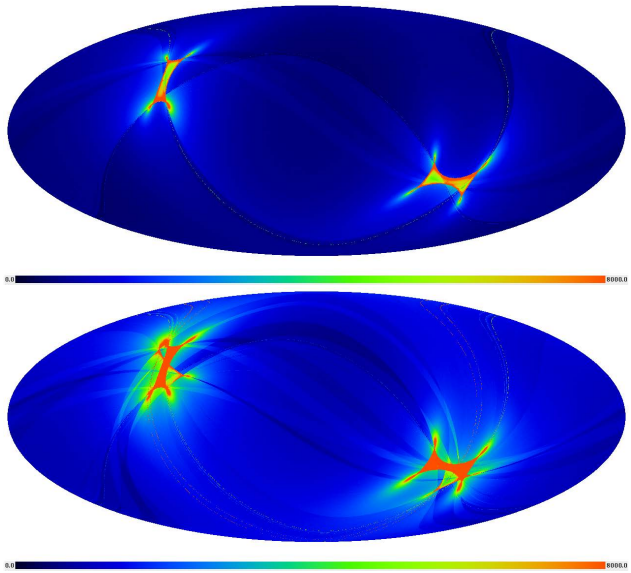

Fig. 5. Survey coverage for the "nominal" mission and the "cryogenic" mission. The colour scale represents total integration time varying between 50 and 8000 sec deg^{-2}) for the 353 GHz channel. The maps are Mollweide projections of the whole sky in Galactic coordinates, pixelised according to the HEALPix (Górski et al. 2005) scheme at $N_{\rm side}$ = 1024.

Routine operations were significantly modified only twice during the routine survey:

- The Sorption Cooler switchover from the nominal to the redundant unit took place on 11 August 2010, leading to an interruption of acquisition of useful scientific data for ∼2 days (one for the operation itself, and one for re-tuning of the cooling chain).
- The satellite's rotation speed was increased to 1.4 rpm between 8 and 16 December 2011. During this period the planet Mars was observed. This operation was implemented to measure systematic effects on the scientific data linked to the spin rate.

Scientific data was acquired during the above two periods but was not used for the generation of the 2013 products.

The resulting integration time after the completion of the "nominal" and "cryogenic" phases of the mission is illustrated in Fig. 5 for a representative frequency channel. More details can be found in the Explanatory Supplement (Planck Collaboration ES 2013).

Operations have been extremely smooth throughout the mission. The total time lost due to a few anomalies is about 5 days spread over the 15.5 months of the nominal mission.

4.3. Satellite environment

The physical environment of the satellite during the routine phase is illustrated in Fig. 6. The main long-timescale thermal modulation is a seasonal effect driven by the solar power absorbed by the satellite, which varies with the distance from the Sun. The thermal environment is sensitive to various satellite operations. For example, before day 257, the communications transmitter was turned on and off around every daily data transmission period, and caused a daily temperature variation clearly visible at all locations in the Service Module, see Fig. 6. Some operational events had a significant thermal impact, which can be appreciated in Fig. 6 and is detailed in Planck Collaboration ES (2013)[4].

The Sorption Cooler dissipates a large amount of power and its variations are seen at all levels within the satellite. The bottom panel of Fig. 6 shows the temperature evolution of the coldest of three stacked conical structures or V-grooves that radiatively isolate the warm service module (SVM) from the cold payload module. Most variations on this structure are due to quasi-weekly power input adjustments of the sorption cooler, which is heat-sunk to it. Many adjustments are seen in the ∼3 months leading up to switchover. After switchover, thermal instabilities were present in the newly operating sorption cooler, which required frequent adjustment, until they reduced significantly around day 750.

Fig. 6 also shows the radiation environment history. As *Planck* started operations, solar activity was extremely low, and Galactic cosmic rays (which produce sharp glitches in the HFI bolometer signals, see Sect. 4.4.2) were able to enter the heliosphere and hit the satellite. As the Sun progressed into solar maximum, the cosmic ray flux as measured by the onboard radiation monitor (SREM, Planck Collaboration ES (2013)) decreased correspondingly, but solar flares increased.

4.4. Instrument environment, operations, and performance

4.4.1. LFI

The front-end of the LFI array is cooled to 20 K by a sorption cooler system, which included a nominal and a redundant unit (Planck Collaboration II 2011). In early August of 2010, the gas-gap heat switch of one compressor element on the active cooler reached the end of its life. Although the cooler can operate with as few as four (out of six) compressor elements, it was decided to switch operation to the redundant cooler. On 11 August at 17:30 GMT the working cooler was commanded off, and the redundant one was switched on. Following this operation, an increase of temperature fluctuations in the 20 K stage was observed. The cause has been ascribed to the influence of liquid hydrogen remaining in the cold end of the inactive (previously operating) cooler. These thermal fluctuations produced a measurable effect in the LFI data, but they propagate to the power spectrum at a level more than four orders of magnitude below the CMB temperature signal (Planck Collaboration III 2013) and have a negligible effect on the science data. Furthermore, in February 2011 these fluctuations were reduced to a much lower level and have remained low ever since.

The behaviour of the 22 LFI radiometers has been extremely stable since the beginning of the observations (Planck Collaboration III 2013), with $1/f$ knee frequencies of order 50 mHz and white noise levels unchanging within a few percent. After optimization during the CPV phase, no changes to the bias of the front-end HEMT low-noise amplifiers and phase switches were required throughout the nominal mission.

The main disturbance to LFI data acquisition has been an occasional bit-flip change in the gain-setting circuit of the data acquisition electronics, probably due to cosmic ray hits (Planck Collaboration II 2013). Each of these events leads to a loss of a fraction of a single ring for the affected detector. The total level

[4] the most notable among these being: a) the "catbed" event between 110 and 126 days after launch; b) the "day *Planck* stood still" 191 days after launch; c) the sorption cooler switchover (OD 460); d) the change in the thermal control loop (OD 540) of the LFI radiometer electronics assembly box; and e) the spin-up campaign around OD 950.

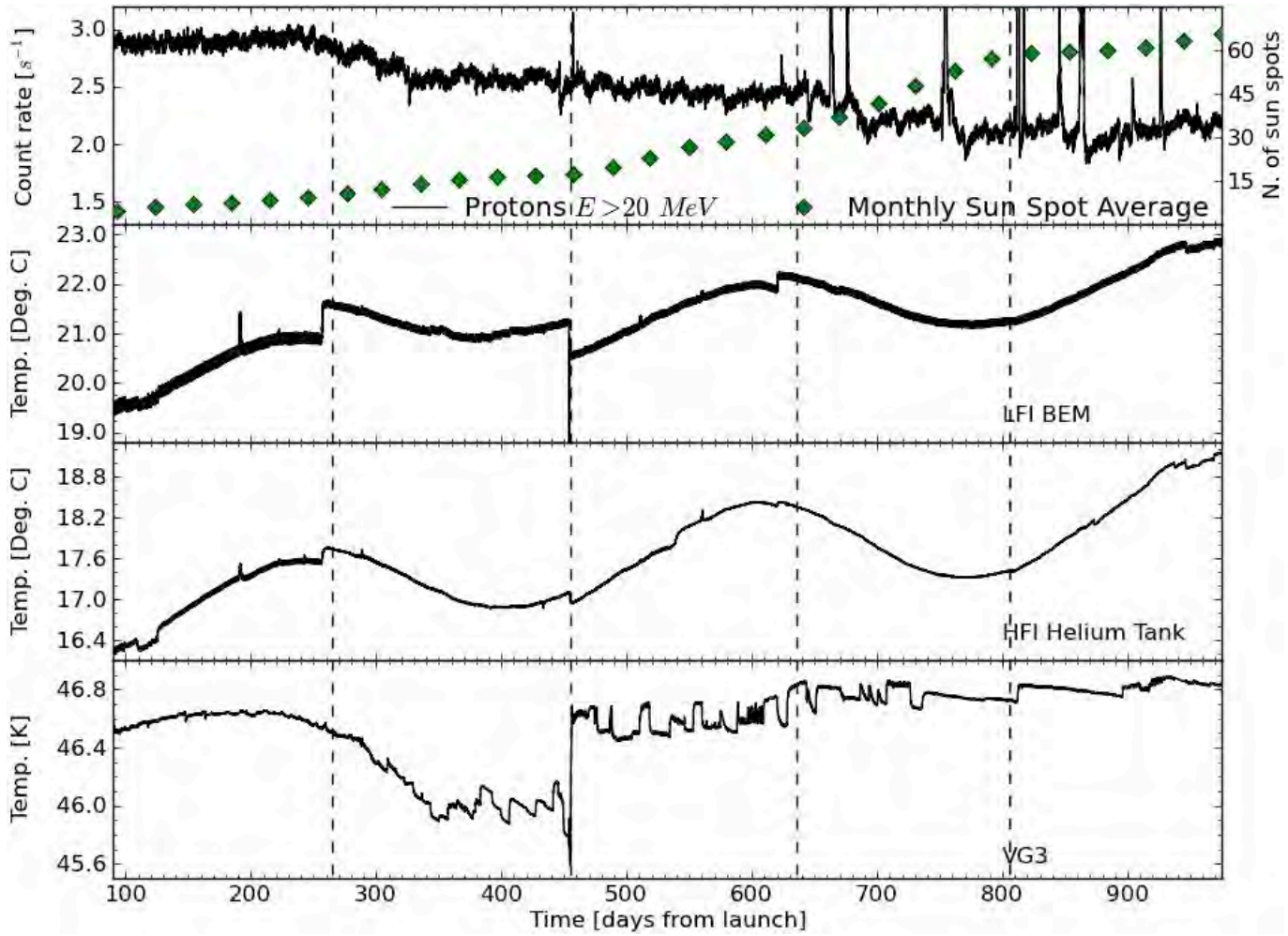

Fig. 6. The thermal and radiation environment of *Planck*. Vertical lines indicate boundaries between surveys. The top panel shows the cosmic ray flux as measured by the onboard SREM; its decrease over time is due to the corresponding increase in solar activity, indicated by the sunspot number, from *h*ttp://www.sidc.be/sunspot-data/. Solar flares show up as spikes in the proton flux. The second and third panels show the temperature variation at two representative locations in the room-temperature SVM, i.e., on one of the (HFI) Helium tanks and on one of the LFI back-end modules (BEM). The sine-wave modulation tracks the variation of distance from the Sun. The bottom panel shows the temperature evolution of VG3, the coldest of three so-called V-grooves, to which the sorption cooler is heat-sunk. The disturbances on the curve are due to adjustments of the operational parameters of this cooler.

of data loss experienced was extremely low, less than 0.12 % averaged over the whole mission.

4.4.2. HFI

The operations of HFI during the survey were extremely smooth. The instrument parameters were not changed after being set during the CPV phase.

The satellite thermal environment had no major impact on HFI. A drift of the temperature of the service vehicle module (SVM) due to the Earth's orbit eccentricity (Fig. 6) induced negligible changes of temperature of the HFI electronic chain; induced gain variations are of order 10^{-4} per degree K.

The HFI dilution cooler (Planck Collaboration II 2011) was operated at the lowest available gas flow rate, giving a lifetime twice the 15.5 months of the nominal mission. This was predicted to be possible following ground tests, and demonstrates how representative of the flight environment these very difficult tests were.

The HFI cryogenic system remained impressively stable over the whole mission. Figure 7 shows the temperature of the three cold stages of the ^{4}He-JT and dilution coolers during the whole mission. The stability of the 1.6 K and 4 K plates, which support the feed horns, couple detectors to the telescope, and support the filters, were well within specifications and produced negligible effects on the scientific signals. The dilution cooler showed the secular evolution of heat lift expected from the small drifts of the ^{3}He and ^{4}He flows as the pressure in the tanks decreased. The PID temperature regulation of the bolometer plate had a long time constant to avoid inducing fluctuations on the plate from cosmic-ray-induced glitches on the PID thermometers. As a result the PID was able to correct only a fraction of the temperature drifts. The main driver of the bolometer plate temperature drifts was the change in the cosmic ray hit rate modulated by the solar cycle, as described in Planck Collaboration II (2011), see also Fig. 7. These slow drifts did not induce any direct significant systematic effect on the scientific signals. The temperature fluctuations of the bolometer plate create steep low frequency noise correlated between detectors. This can be mostly removed using the measured temperatures, leaving a negligible residual at frequencies above the spin frequency of 0.016 Hz.

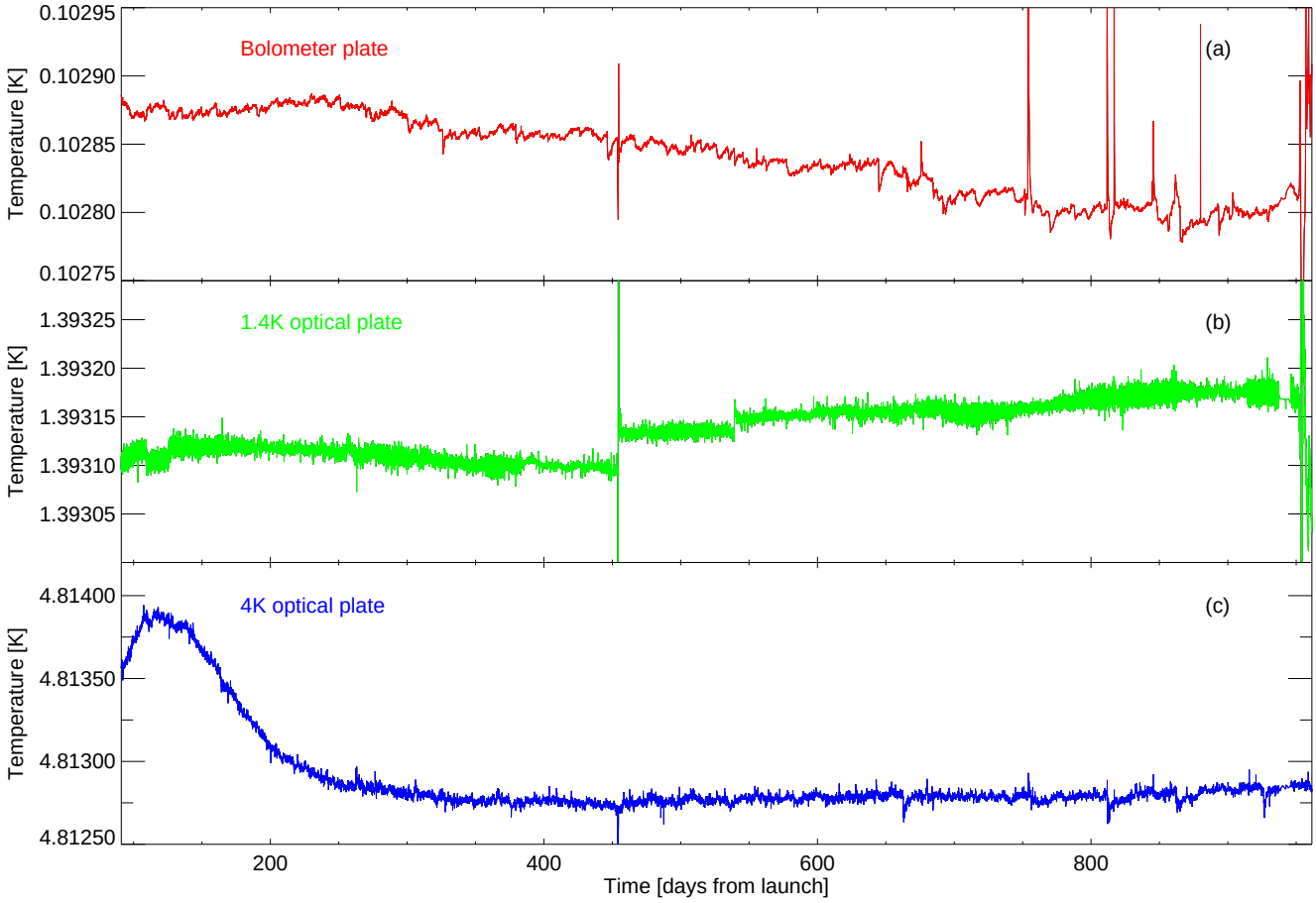

Fig. 7. The impressive stability of the HFI thermal stages during operations. Shown is the temperature evolution of the bolometer stage (*top*), the 1.6 K optical filter stage (*middle*) and the 4-K cooler reference load stage (*bottom*). The horizontal axis displays days since the beginning of the nominal mission.

The main effect of the cooling system on the scientific signals is an indirect one: the very slow drift of the detector temperature over periods of weeks or months changes the amplitude of the modulated signal that shifts the science signal on the analog to digital converters (ADCs) present on each detector and thermometer electronic chain. The non-linearities of these devices, especially in the middle of their dynamic range, where most of the scientific signal is concentrated, lead to a systematic effect that can only be corrected empirically using the redundancies in its first order effect — a gain change — in the data processing (details are given in Sect. 5.3.2).

Detector to detector cross-talk was checked in flight using Jupiter and strong glitches. The level of cross-talk between detectors in different pixels is very low; however, the level of cross-talk between the two polarization sensitive bolometers (PSB) of a PSB pair is significant, in line with ground based measurements. For temperature-only analysis, this effect is negligible.

Two of the HFI bolometers, one at 143 GHz and one at 545 GHz, suffer heavily from "random telegraphic noise" (Planck Collaboration VI 2013) and are not used. A third bolometer (at 857 GHz) was also affected by this problem, but some of the data were useable.

Cosmic rays induce short signal glitches in the scientific signal when they deposit energy either in the thermistor or on the bolometer grid. They were observed in flight at the predicted rate with a decay time constant equal to the one measured during ground testing. In addition, a different kind of glitches was observed, occurring in larger numbers but with lower amplitudes and long time constants; they are understood to be induced by cosmic ray hits on the silicon wafer of the bolometers (Planck Collaboration X 2013). The different kinds of glitches observed in the HFI bolometers are described in detail in Planck Collaboration X (2013). High energy cosmic rays also induce secondary particle showers in the spacecraft and in the vicinity of the focal plane unit, contributing to correlated noise (Planck Collaboration VI 2013).

A more detailed description of the performance of HFI is available in Planck Collaboration VI (2013).

4.4.3. Payload

An early assessment of the flight performance of *Planck*'s payload (i.e., two instruments and telescope) was given in Mennella et al. (2011, LFI) and Planck HFI Core Team (2011a, HFI), and summarized in Planck Collaboration I (2011). Updates based on the full nominal mission are given for LFI in Planck Collaboration II (2013), Planck Collaboration III (2013), Planck Collaboration IV (2013), and Planck Collaboration V (2013), and for HFI in Planck Collaboration VI (2013), Planck Collaboration VII (2013), Planck Collaboration VIII (2013), Planck Collaboration IX (2013), and Planck Collaboration X (2013).

None of the LFI instrument performance parameters has changed significantly over time. A complete analysis of sys-

tematic errors (Planck Collaboration III 2013) shows that their combined effect is more than three orders of magnitude (in μK^2) below the CMB temperature signal throughout the measured angular power spectrum. Similarly, the HFI performance in flight is very close to that measured on the ground, once the effects of cosmic rays are taken into account (Planck Collaboration X 2013; Planck Collaboration VI 2013).

Table 2 summarizes the slightly updated performance of *Planck*'s payload. All performance is well in line with and in some cases exceeding pre-launch expectations.

4.5. Satellite Pointing

The attitude of the satellite is computed on board from the star-tracker data and reprocessed daily on the ground. The result is a daily Attitude History File (AHF), which contains the filtered attitude of the three coordinate axes based on the star trackers with a maximum frequency of one record every 0.125 s during stable observations ("rings") and 0.25 s during re-orientation slews. The production of the AHF is the first step in the determination of the pointing of each detector on the sky (see Sect. 5.5).

Early on it was realized that there were some problems with the pointing solutions. First, the attitude determination during slews was much poorer than during periods of stable pointing. Second, the solutions were affected by thermoelastic deformations in the satellite driven by thermal variations driven by internal thermal control loops and the sorption cooler, as well as by the thermally-driven transfer of helium from one tank to another.

A significant effort was made to improve the ground processing capability to address the above issues. As a result, three different flavors of the AHF are now produced for the whole mission:

- the AHF: an optimised version of the initial (pre-launch) algorithm
- the GHF: an algorithm that uses, in addition to the star tracker data, angular rate measurements derived from the on-board fiber-optic gyro[5]
- the DHF: an algorithm that uses the star tracker data in conjunction with a dynamical model of the satellite that accounts for the existence of disturbances at known sorption cooler operation frequencies.

Both the GHF and DHF algorithms improve significantly the recovery of attitude during slews. Due to the deadlines involved, the optimised AHF algorithm has been used in the production of the 2013 release of *Planck* products. However, in the future we expect to use the improved algorithms, in particular enabling the use the scientific data acquired during slews (9.2 % of the total).

The pointing characteristics at AHF level are summarised in Table 3.

5. Critical steps towards production of the *Planck* maps

5.1. Overview and philosophy

Realization of the potential for scientific discovery provided by *Planck*'s combination of sensitivity, angular resolution, and frequency coverage places great demands on methods of analysis, control of systematics, and the ability to demonstrate correctness of results. Multiple levels and techniques of methods, comparisons, tests, redundancies, and cross-checks are necessary beyond what has been required in previous experiments. Among the most important are:

Redundancy in observations—As described in Sect.4.1, the scanning strategy provides two important levels of redundancy. First, multiple passes over the same sky are made by each detector at each position of the spin axis. (These are called "rings.") Differences of the data between halves of one ring (whether first and second half or interleaved halves) provide direct evidence of the actual noise of a given detector. This is possible because the sky signal subtracts out to high accuracy. Second, null tests on six-month surveys and on one-year intervals reveal important characteristics of the data.

Multiplicity of methods—Multiple, independent, methods have been developed for all important steps in the processing and analysis of the data. Comparison of results of independent methods provides a powerful test for bugs, insight into the effects of different techniques. Component separation provides a good example (Sect. 7.1; Planck Collaboration XII 2013).

Comparison of LFI and HFI—The two instruments are different and the systematics that affect them are different, but they scan the same sky in the same way. Especially at frequencies near the foreground minimum, where the CMB signal dominates over much of the sky, comparison of results from the two provides one of the most powerful demonstrations of data quality ever available in a CMB experiment.

Simulations—Simulations can be used to: 1) quantify the effects of systematics. We simulate data with a systematic effect included, process as we process the sky data, and measure residuals. 2) validate and verify tools used to measure instrument characteristics from the data. We simulate data with know instrument characteristics, apply the tools used on the sky data to measure the characteristics, and verify the accuracy of their recovery. 3) validate and verify data analysis algorithms and their implementations. We simulate data with known science inputs (cosmology and foregrounds) and instrument characteristics (beams, bandpasses, noise), apply the analysis tools used on the sky data, and verify the accuracy of recovered inputs. 4) support analysis of the sky data. We generate massive Monte Carlo simulation sets of the CMB and noise, and pass them through the analyses used on the sky data to quantify uncertainties and correct biases. The first two uses are instrument-specific; distinct pipelines have been developed and employed by LFI and HFI. The last two uses require consistent simulations of both instruments in tandem. Furthermore, the Monte Carlo simulation-sets are the most computationally intensive part of the *Planck* data analysis and require large computational capacity and capability.

5.2. Simulations

We simulate TOI for the full focal plane (FFP) for the nominal mission. Each FFP simulation comprises: a single "fiducial" realization (CMB, astrophysical foregrounds, and noise), together with separate Monte Carlo (MC) realizations of the CMB and noise. The first Planck cosmology results were supported primarily by the sixth FFP simulation-set, hereafter FFP6. The first five FFP realizations were less comprehensive and were primarily used for validation and verification of the Planck analysis

[5] The *Planck* fiber-optic gyro is a technology development instrument that flew on *Planck* as an opportunity experiment. It was not initially planned to use its data for computation of the attitude over the whole mission.

Table 2. *Planck* performance parameters determined from flight data.

Channel	$N_{detectors}$ [a]	ν_{center} [b] [GHz]	Scanning Beam [c] FWHM [arcm]	Scanning Beam [c] Ellipticity	Noise [d] Sensitivity [μK_{RJ} $s^{1/2}$]	Noise [d] Sensitivity [μK_{CMB} $s^{1/2}$]
30 GHz	4	28.4	33.16	1.37	145.4	148.5
44 GHz	6	44.1	28.09	1.25	164.8	173.2
70 GHz	12	70.4	13.08	1.27	133.9	151.9
100 GHz	8	100	9.59	1.21	31.52	41.3
143 GHz	11	143	7.18	1.04	10.38	17.4
217 GHz	12	217	4.87	1.22	7.45	23.8
353 GHz	12	353	4.7	1.2	5.52	78.8
545 GHz	3	545	4.73	1.18	2.66	0.0259[d]
857 GHz	4	857	4.51	1.38	1.33	0.0259[d]

[a] For 30, 44, and 70 GHz, each detector is a linearly polarized radiometer, and there are two orthogonally polarized radiometers behind each horn. Each radiometer has two diodes, both switched at high frequency between the sky and a blackbody load at ~ 4 K (Mennella et al. 2011). For 100 GHz and above, each detector is a bolometer (Planck HFI Core Team 2011a). Most of the bolometers are sensitive to polarization, in which case there are two orthogonally polarized detectors behind each horn. Some of the detectors are spider-web bolometers (one per horn) sensitive to the total incident power. Two of the bolometers, one each at 143 and 545 GHz, are not used as they are heavily affected by random telegraphic noise (Planck HFI Core Team 2011a). A third bolometer, at 857 GHz, is also affected, but some of its data are usable.

[b] Effective (LFI) or Nominal (HFI) center frequency of the N detectors at each frequency.

[c] Mean scanning beam properties of the N detectors at each frequency. FWHM ≡ FWHM of circular Gaussian with the same volume. Ellipticity gives the major axis to minor axis ratio for a best-fit elliptical Gaussian. In the case of HFI, the mean values quoted are the result of averaging the values of total-power and polarization-sensitive bolometers, weighted by the number of channels and after removal of those affected by random telegraphic noise. The actual point spread function of an unresolved object on the sky depends not only on the optical properties of the beam, but also on sampling and time domain filtering in signal processing, and the way the sky is scanned.

[d] The noise level reached in 1 s integration for the array of N detectors, given the noise and integration time in the released maps, for the array of N detectors, in Rayleigh-Jeans units and in thermodynamic CMB units for 30–353 GHz; in Rayleigh-Jeans units and in MJy sr^{-1} $s^{1/2}$ for 545 and 857 GHz. We note that for LFI the white noise level is within 1-2% of these values.

Table 3. Pointing performance over the nominal mission.

Characteristic	Median	Std. dev.
Spin rate [deg s^{-1}]	6.00008	0.00269
Small manoeuvre accuracy [arcsec]	5.1	2.5
Residual nutation amplitude after manoeuvre [arcsec]	2.5	1.2
Drift rate during inertial pointing [arcsec hr^{-1}]	12.4	1.7

codes and for cross-validation of the DPC and FFP simulation pipelines.

To mimic the sky data as closely as possible, FFP6 used the flight pointing, data flags and detector band-passes, beams and noise properties. For the fiducial realization, maps were made of the total observation (CMB, foregrounds and noise) at each frequency for the nominal mission. In addition, maps were made of each component separately, of subsets of detectors at each frequency, and of half-ring and single survey subsets of the data. The noise and CMB Monte Carlo realization-sets also include both full- and sub-sets of detectors at each frequency and full- and half-ring data sets for each detector combination. With about 125 maps per realization and 1000 realizations of both the noise and CMB, FFP6 totals some 250,000 maps — by far the largest simulation set ever fielded in support of a CMB mission.

5.3. Timeline processing

5.3.1. LFI

The processing of LFI data (Planck Collaboration II 2013; Planck Collaboration III 2013; Planck Collaboration IV 2013; Planck Collaboration V 2013) is divided into three levels. Level 1 retrieves information from telemetry packets and auxiliary data received each day from the Mission Operation Center (MOC) and transforms the scientific time-ordered information (TOI) and housekeeping (H/K) data into a form that is manageable by the Level 2 scientific pipeline. The Level 1 steps are:

- uncompress the retrieved packets;
- de-quantize and de-mix the uncompressed packets to retrieve the original signal in analog-to-digital unit (ADU);
- transform ADU data into volts;
- time stamp each sample;

The Level 1 software has not changed since the start of the mission. Detailed information is described in Zacchei et al. (2011) and Planck Collaboration II (2013). Following Level 1, Level 2 processes scientific and H/K information into data products. The highly stable behaviour of all 22 LFI radiometers means that very few corrections are implemented in the LFI data processing, both at TOI and map level. The main Level 2 steps are:

- Build the LFI reduced instrument model (RIMO) that contains all the main instrumental characteristics (beam size, spectral response, white noise etc);
- Remove some spurious effects at diode level. Small electrical disturbances, synchronous with the 1 Hz on-board clock, are removed from the 44 GHz data streams. For some channels (in particular LFI25M-01) non-linear behaviour of the

ADC has been identified and corrected for by analyzing the white noise level of the total power component. No corrections are applied to compensate for thermal fluctuations in the 4 K, 20 K, and 300 K stages of the instrument, since H/K monitoring and instrument thermal modelling confirm that their effect is below significance.
- Compute and apply the gain modulation factor to minimize the $1/f$ noise. The LFI timelines are produced by taking differences between the signals from the sky and from internal blackbody reference loads cooled to $\sim$ 4.5 K. Radiometer balance is optimized by introducing a gain modulation factor, typically stable to 0.04 % throughout the mission, which greatly reduces $1/f$ noise and improves immunity from a wide class of systematic effects.
- Combine the diodes to remove a small anti-correlated component in the white noise;
- Identify and flag periods of time containing anomalous fluctuations in the signal. A total of < 1 % of the data acquired during the nominal mission are flagged.
- Compute the corresponding detector pointing for each sample based on auxiliary data and the reconstructed focal plane geometry (Sect. 5.5);
- Calibrate the scientific timelines to physical units ($K_{\rm CMB}$) fitting the dipole convolved with a 4π representation of the beam (Sect. 5.6);
- Combine the calibrated TOIs into aggregate products as maps at each frequency (Sect. 6.2.1).

The Level 3 then collects instrument-specific (from both HFI and LFI) Level 2 outputs and derives various scientific products as maps of separated astrophysical components.

5.3.2. HFI

Following L1 processing similar to that of LFI, the HFI-specific data pipeline consists of TOI processing followed by map making/calibration, which are described for this 2013 release in a group of separate papers (Planck Collaboration VI 2013; Planck Collaboration VII 2013; Planck Collaboration VIII 2013; Planck Collaboration IX 2013; Planck Collaboration X 2013).

The HFI processing pipeline steps are:

- Demodulate as required by the AC square-wave polarization bias of the bolometers.
- Flag and remove cosmic-ray-induced glitches, including the long time-constant tails of glitches induced in the silicon wafer. More than 95 % of the acquired samples are affected by glitches. Glitch templates constructed from averages are fitted and subtracted from the timelines; the fast part of each glitch is rejected. The fraction of time-ordered data rejected due to glitches is 16.5 %[6] when averaged over the nominal mission.
- Correct for the slow drift of the bolometer response induced by the bolometer plate temperature variation described in Sect. 4.4.2. A baseline drift estimated from the signal from the dark bolometers on the same plate (smoothed over 60 s) is removed from each timeline.
- Deconvolve the bolometer complex time response, which is analyzed in detail in Planck Collaboration VII (2013).
- Remove the narrow lines induced by EMI-EMC interference from the ^{4}He-JT cooler, exploiting the fact that the cooler is synchronized with the HFI readout and operates at a harmonic of the sampling rate.
- Analyze the statistics of the time-scale of pointing periods and discard anomalous ones (less than 1 % of the data are discarded).

It was realized recently that some apparent gain variations, identified when comparing identical pointing circles one year apart, actually originate in non-linearities in the analog-to-digital converters (ADC) of the bolometer readout system. Lengthy onboard measurements of the non-linear properties of the ADCs have been carried out in 2012 and 2013 after the end of cryogenic operations, and algorithms to correct for these non-linearities have been developed. Although the direct effect of the parasitic ^{4}He-JT cooler lines is easily removed in the TOI processing (see above), it also induces a voltage on the modulated bolometer signals before they are digitized (by the ADC) and averaged onboard. As a consequence, it is more difficult to estimate the ADC non-linearity correction accurately for the detectors that are the most affected by the ^{4}He-JT lines.

The full ADC non-linearity correction is still in development as the present data products and papers are being prepared, and therefore it has not been applied to the data. Instead, a calibration scheme (see Sect. 5.6, Planck Collaboration VIII (2013)) is implemented that estimates a varying gain and corrects very well the first order impact of this systematic effect. A full correction will be implemented for the release of the polarization data, for which the higher order effects are not negligible.

5.4. Beams

As described in Planck Collaboration IV (2013), the main beam parameters of the LFI detectors and the geometry of the focal plane were determined using Jupiter as a source. By combining four Jupiter transits (around days 170, 415, 578, and 812) the beam shapes were measured down to -20 dB from peak at 30 and 44 GHz, and -25 dB at 70 GHz. The FWHM of the beams is determined with a typical uncertainty of 0.3 % at 30 and 44 GHz, and 0.2 % at 70 GHz. The alignment of the focal plane and the location of each detector's phase centre were varied until co-polar and cross-polar *model* patterns were obtained (using the GRASP physical optics software) that reproduce the measurements to high accuracy. To estimate the uncertainties in the determination of the in-flight beam models, a set of optical models representative of the measured LFI scanning beams was found, using GRASP to randomly distort the wavefront error of the physical model of telescope and detectors, then rejecting those distorted models whose predicted patterns fell outside the error envelope of the measured ones.

Sidelobe pick-up by the LFI has been simulated by coupling the GRASP models over 4π with the main celestial sources, i.e., solar dipole and diffuse Galactic emission (Planck Collaboration III 2013). Null tests between even and odd surveys, to enhance the effect of the inverted symmetry in the coupling, were systematically used as diagnostics. At 30 GHz (where straylight effects are larger due to higher Galactic emission), straylight contamination is detected at the $\sim 10\,\mu$K level. This contamination was removed by fitting it to a model that incorporates the radiometer band shape and the optical response variation across the band, then removing the model. Residual straylight effects in the maps are estimated to be less than $\sim 2\,\mu$K at all frequencies.

The in-flight scanning beams[7] of HFI (Planck Collaboration VII 2013) were measured using observations of Mars.

[6] varying from 10 to 26.7 % depending on the bolometer.

[7] The term "scanning beam" refers to the angular response of a single detector to a compact source including both the optical beam and the effects of time domain filtering. In the case of HFI, a Fourier filter de-

Observations of Saturn and Jupiter are used to estimate the near sidelobes and other residuals. The HFI bolometers have a complex time response which includes long time constants. To obtain a compact scanning beam, this time behaviour must be deconvolved from the measured timelines. The deconvolution algorithm is iterative, allowing an estimate of the parameters of the bolometer transfer function, and forcing the resulting scanning beams to be more compact. A spline representation of the beams is used, allowing capture of the near-sidelobe structure. Stacking of multiple crossings of Jupiter allows us to obtain high signal-to-noise ratio maps of these near sidelobes, and to quantify the level of unmodelled effects. Such images also reveal clearly sharp "grating lobes", which are due to so-called dimpling of the telescope reflectors caused by its honeycomb structure. The amplitude of these lobes is larger than predicted, indicating mechanical changes in the reflectors after launch; however, the total power contained in these lobes remains negligible in terms of impact on the scientific data, and therefore they are ignored in the scanning beam model.

The uncertainties in the estimation of the HFI scanning beams and other systematic effects effects in the maps are determined at window function level, using realistic Monte-Carlo simulations that include pointing effects, detector noise, and measurement effects. Additional estimates are made of the effect of planet emission variability, beam colour corrections, and more. The total uncertainties in the scanning beam solid angles are 0.53 %, 0.14 %, 0.11 % at 100, 143, and 217 GHz respectively.

Galactic emission entering the HFI bolometers through the far sidelobes due to the primary reflector spillover (Tauber et al. 2010b) is clearly seen (Planck Collaboration XIV 2013) in survey difference maps at 545 and 857 GHz at times when the central part of the galactic plane is aligned with the elongated far sidelobe. Physical models of the sidelobes (based on 4π GRASP simulations) are fit to odd-even survey difference maps to estimate sidelobe levels for each detector. The level of these is highly variable between the 857 GHz detecors, illustrating how the difficult it is to predict spillover levels for the high frequency channels. A model of the sidelobe from the primary reflector spillover signal can then be removed from the time-ordered data before proceeding to mapmaking at the frequencies where it has been detected; being close to the spin axis, they are largely unmodulated by the spinning motion, and are mostly removed by the destriping map-making code. The secondary reflector spillover far sidelobes — detected (Planck Collaboration XIV 2013) at roughly the levels expected from optical modelling (Tauber et al. 2010b) — is composed of two parts, the direct spillover on the sky, and a part which reflects on the telescope baffle and is spread into a very large diffuse pattern. The direct spillover results in a sidelobe between 5° and 20° from the main beam. This part of the far sidelobes affects mainly the calibration on the solar dipole (see Sect. 5.6). The impact of sidelobe effects on both the gain calibration factors and the associated spatial frequency (multipole) transfer function (discussed in Planck Collaboration VII (2013); Planck Collaboration VIII (2013); Planck Collaboration VI (2013)), is of order 1.3×10^{-3} and has been neglected in this release, as there are other systematic effects of larger amplitude.

The HFI far sidelobe signals and zodiacal light are removed at TOI level in the same pipeline. Two different sets of maps are produced by HFI Planck Collaboration VI (2013). In the default set, no attempt is made to remove either far sidelobes or zodiacal light; a second set of maps does include the removal of both types of signals.

convolves the bolometer/electronics time response and lowpass-filters the data. In the case of LFI, the sampling tends to smear signal in the time domain.

5.5. Focal Plane Geometry and Pointing

The time-dependent pointing direction of each detector in *Planck* is initially based on the filtered star tracker data provided in the daily Attitude History Files (see Sect. 4.5). Corrections to the AHF are applied based on the estimated "wobble angles", which reflect changes in the inertial tensor of the satellite resulting from fluid depletion, but also spurious effects from time varying thermoelastic deformations of structures between the star tracker and the telescope boresight. Stellar aberration is also corrected. The measured in-flight focal plane geometry is then used to estimate the corrected pointing timestream for each detector.

The focal plane geometry[8] of LFI was determined independently for each Jupiter crossing (Planck Collaboration IV 2013). The solutions for the first two crossings agree to 2 arcsec, and so do the third and fourth. However, a shift of ∼15 arcsecs (largely in the in-scan direction) is found between the first two and the second two crossings. For this reason, the focal plane geometry is assumed constant over time, with the exception of a single step-function change on OD 540.

The focal plane geometry of the HFI detectors was also measured using planet observations (Planck Collaboration VI 2013; Planck Collaboration VII 2013). The relative location of individual detectors differs from the ground prediction typically by 1′, mainly in the in-scan direction, indicating some de-alignment of the HFI focal plane and/or telescope in flight. The high signal-to-noise ratio available on Jupiter allows us to estimate pointing "errors" on one minute timescale; these measurements show the presence of thermo-elastic deformations of the star tracker mounting structure that are well correlated with a known onboard thermal control cycle. This specific cycle was changed on OD 540, leading to a reduction in this "error" from 3″ to 1″. These small high-frequency effects are not taken into account at the present time. However, larger (up to 15 arcseconds) slow pointing variations are observed with time scales of order 100 days using measurements of bright compact radio sources. The HFI focal plane geometry variation with time is corrected for this trend, leaving an estimated total pointing reconstruction error of a few arcseconds rms.

5.6. Calibration

The photometric (gain) calibration of LFI and HFI is achieved by comparing the measured data against the expected signal from the solar and orbital dipoles. The solar dipole parameters are assumed to be those determined by WMAP7 (Jarosik et al. 2011). In the future, a *Planck*-determined dipole will replace the WMAP7 dipole, which during the initial period of *Planck* analysis has provided a convenient, stable, and accurate starting point. The orbital dipole is determined from the measured satellite orbital motion so in principle it can provide an independent absolute calibration.

In the LFI pipeline (Planck Collaboration V 2013), an iterative fit outside a galactic mask plus low-frequency filtering yields a single calibration constant for each pointing period (or ring). For 44 and 70 GHz, an adaptive smoothing function removes the

[8] i.e., the relative location on the sky of all detectors

effect of low-frequency noise stripes from the time series of ring gains. The 30 GHz data are more affected by sidelobe signals, and for this channel only it has been found more effective to estimate the relative changes in the ring (see Sect. 4.1) gains over time by using the total power variations of the 4-K reference loads measured by each radiometer. This relative estimation is carried out over three different time periods (which account for significant thermal changes in the 20 K and 4 K stages due to operational events). The estimated gains are applied to the acquired data in the time domain. The solar and orbital dipole signals are then removed from the time-ordered data before proceeding into mapmaking.

At the present stage, the overall uncertainty in the LFI calibration relative to the *WMAP* solar dipole is of order 0.4%, plus the 0.25% intrinsic uncertainty in the *WMAP* calibration, which we conservatively add linearly (Table 6). The LFI uncertainty is dominated by the beam uncertainty over the band (0.1-0.4% depending on the frequency), sidelobe convolution (about 0.2%), and residual systematics (0.1-0.2%).

As mentioned in section 5.6 (and described in more detail in Planck Collaboration V, 2013), preliminary results on the orbital dipole as measured by LFI are in quite good agreement with WMAP results (consistency is < 0.2 % at 70 GHz and < 0.1 % at 44 GHz). This indicates very good consistency of LFI and WMAP calibrations at $\ell = 1$. This independent measurement of the solar dipole by the LFI combined with the inter-calibration described above extends this consistency to the HFI CMB channels.

In the HFI pipeline (Planck Collaboration VIII 2013), a pencil beam is assumed when comparing data to the expected signals. In this process, the far sidelobe due to the direct spillover (see Section 5.4), which is the dominant correction for the dipole calibration, has been neglected. Its contribution to the solar dipole signal is estimated to be 0.13 % after destriping. LFI (Planck Collaboration V 2013) uses instead a full 4π beam convolution of the dipole; however, it has been verified a posteriori that the net effect of the convolution produces calibrated maps that are very close (to within 10^{-4}) to those obtained with a pencil beam approximation. It is therefore legitimate to assume a pencil beam model for both LFI and HFI. Second order corrections (of order ∼0.1–0.2 % for CMB channels) are not removed at this stage of the analysis and contribute to the overall calibration uncertainty. To fully correct these effects, it will be necessary to introduce in the data processing pipeline an effective efficiency of the scanning strategy as a function of the distance from the spin axis, as proposed for HFI in Planck Collaboration IX (2013); Planck Collaboration VIII (2013). Such a correction has not been implemented for this 2013 release because it is smaller than other systematic effects that are not yet corrected, e.g., ADC non-linearity second order effects for HFI (see Sect. 5.3.2), or beam uncertainty over the band for LFI (Planck Collaboration V 2013).

Fitting for the HFI gains is done at ring level, including a spatial model of Galactic emission based on HFI maps, and excluding the Galactic plane. It yields three parameters per ring: a dipole gain, a Galactic gain, and an offset. An initial gain model consists of a fixed gain averaged over a contiguous set of 4000 rings where the ring-to-ring dispersion is less than 1 %. An iterative scheme is then applied to the 100–217 GHz channels that fits for relative variations of the gain over the whole mission. This scheme is not applied to the 353 GHz channel because intra-pixel emission gradients cause instability in the iterations. Remaining residuals in the calibrated rings are estimated by comparisons between detectors, and are of order 0.3 % for 100–217 GHz and 1 % at 353 GHz. Once the HFI rings are calibrated, they are converted to maps using a destriping algorithm (see Sect. 6.2.2), and the WMAP7 dipole is removed from the maps.

The current calibration scheme of HFI has been checked against an independent algorithm based on the orbital dipole only (Tristram et al. 2011). Relative variations are typically about 0.1 %, and always smaller than 0.2 %, except for a systematic bias of 0.5–1 % believed to be due to the (currently uncorrected) ADC non-linearities (Sect. 5.3.2), which affect the two methods differently. The total gain calibration accuracy, as evaluated from the ring-to-ring variability, overestimates the real accuracy since part of the variability is being corrected.

A better estimate of the final calibration accuracy can be obtained by measuring the relative calibration between individual detectors and between frequency bands directly on the CMB dipole and anisotropies. Such comparisons (Section 6.5, Planck Collaboration XI (2013)) have been made with LFI and HFI maps, and show a relative calibration accuracy of better than 0.2 % for the CMB channels (see Fig. 11. Inter-frequency checks within each instrument, and the evaluation of solar dipole residuals, provide limits to the quality of LFI and HFI calibration process with repect to their common reference, i.e., the *WMAP* solar dipole.

In summary, the relative calibration accuracy of all *Planck* channels between 44 and 217 GHz is better than 0.2 %, whereas the 30 and 353 GHz channels are within 0.8 % of the CMB channels. Combining this relative estimate with the accuracy of the determination of the orbital dipole obtained with the 44 GHz LFI channel, the calibration of the *Planck* CMB channels with respect to the *WMAP* dipole is estimated to be better than 0.3%. The absolute calibration is limited by the accuracy of the CMB temperature (an uncertainty of 0.2%), leading to an absolute calibration of the *Planck* CMB channels of better than 0.4%. Significant improvements are expected for the next release, when orbital dipole analysis is planned to be fully implented for both instruments.

The calibration philosophy for the two submillimetre channels of HFI (545 and 857 GHz) has been modified from what was initially planned and reported in Planck HFI Core Team (2011b). The original approach was to compare the HFI maps to Galactic emission maps observed by *COBE*/FIRAS Mather et al. (1999). In the previous work, this comparison was done only at high Galactic latitudes because the narrow Galactic ridge led to a calibrated level that was incompatible (too high) with the CMB dipole calibration at 353 GHz. However, a more detailed investigation of the FIRAS-based calibration led to a number of inconsistencies that are discussed in Planck Collaboration VIII (2013). Therefore, the calibration scheme at 545 and 857 GHz is now based on fitting the HFI measurements of the flux density of Uranus and Neptune to planetary emission models, which have an absolute accuracy of about 5 % but a relative accuracy of ∼2 %. This process is described in detail in Planck Collaboration VIII (2013). The overall estimated accuracy of the gain calibration with this method is estimated at 10 %.

6. Frequency Maps

6.1. Beam representation

As described in Sect. 5.4, the LFI scanning beams are represented by GRASP models fitted to observations of Jupiter, whereas the HFI scanning beams are represented by B-spline surfaces fitted to observations of Mars. The *Planck* frequency

Table 4. Statistics of spatial distribution of effective beam parameters: FWHM, ellipticity and beam solid angle

Band	FWHM[a] [arcmin]	Ellipticity	Ω [arcmin^2]
30	32.239 ± 0.013	1.320 ± 0.031	1189.51 ± 0.84
44	27.01 ± 0.55	1.034 ± 0.033	833 ± 32
70	13.252 ± 0.033	1.223 ± 0.026	200.7 ± 1.0
100	9.651 ± 0.014	1.186 ± 0.023	105.778 ± 0.311
143	7.248 ± 0.015	1.036 ± 0.009	59.954 ± 0.246
217	4.990 ± 0.025	1.177 ± 0.030	28.447 ± 0.271
353	4.818 ± 0.024	1.147 ± 0.028	26.714 ± 0.250
545	4.682 ± 0.044	1.161 ± 0.036	26.535 ± 0.339
857	4.325 ± 0.055	1.393 ± 0.076	24.244 ± 0.193

[a] Mean of best-fit Gaussians to the effective beams.

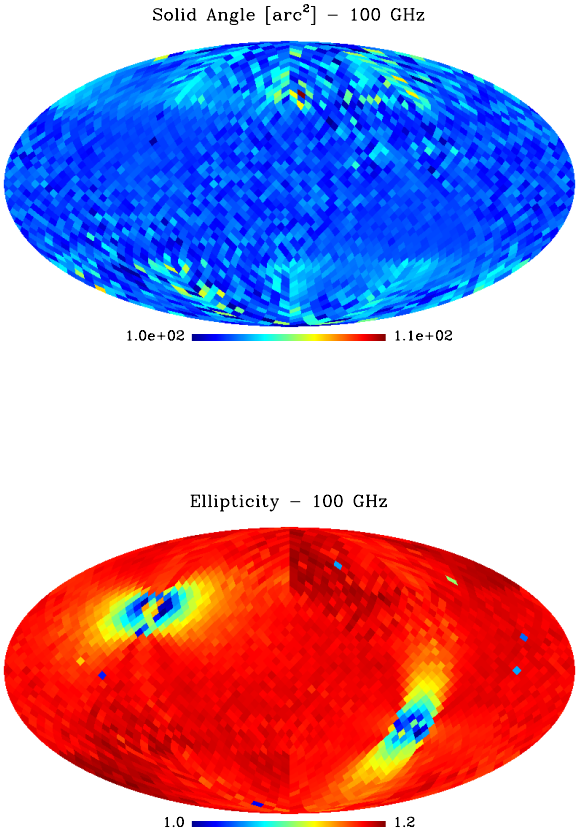

Fig. 8. This figure shows the distribution across the sky of the solid angle (top) and ellipticity of the effective beams at 100 GHz. The distribution is typical for all channels.

maps are of course constructed from many detectors that sample each pixel at different angles. Therefore the scanning beams do not represent well the point spread function at map level. Instead, "effective beams" are computed for each pixel and frequency using the FEBeCoP algorithm (Mitra et al. 2011).

FEBeCoP calculates the effective beam at a position in the sky by computing the real space average of the scanning beam over all observed crossing angles at that sky position. Table 4 summarizes the distribution across the sky of a set of parameters representing the beams, and Fig. 8 shows, in the 100 GHz case, their variation across the sky. We note that the effective beams include pixelization effects (essentially the HEALpix pixelization window function). The effective beam window function for LFI is calculated by FEBeCoP using an ensemble of signal-only simulations convolved with the effective beams. For HFI, the quickbeam harmonic space effective beam code (Planck Collaboration VII 2013) is used to calculate the effective beam window function given the scan history and the scanning beam.

To estimate the uncertainty of the effective beams, the ensemble of allowed LFI GRASP models (Sect. 5.4) was propagated through FEBeCoP and used to determine window function errors. For HFI, quickbeam is used to propagate an ensemble of simulated Mars observations to harmonic space, constructing effective beam window function errors. The total uncertainties in the effective beam window function (in B_ℓ^2 units) at $\ell = 600$ are 2 % at 30 GHz and 1.5 % at 44 GHz. At $\ell = 100$ they are 0.7 %, 0.5 %, 0.2 %, and 0.2 % for 70, 100, 143, and 217 GHz respectively (Planck Collaboration IV 2013; Planck Collaboration VII 2013).

6.2. Mapmaking

6.2.1. LFI

The calibrated TOI of each LFI radiometer are used as input to the Madam mapmaking code (Keihänen et al. 2010) together with the corresponding pointing data, in the form of the Euler angles (θ, ϕ, ψ). Madam implements a polarized destriping approach to mapmaking; the noise is modelled as white noise plus a set of offsets, or baselines. The algorithm estimates in a maximum-likelihood fashion the amplitudes of the baselines, subtracts them from the actual TOI, and then simply bins the result into a map. The output consists of pixelized maps of the three Stokes parameters (T, Q, U). The LFI temperature maps being released at this time are shown as the first three maps in Fig. 9.

One of the key parameters in the Madam algorithm is the baseline length that represents the time scale at which the baseline approximation of low-frequency noise is applied. We choose baseline lengths corresponding to an integer number of samples (33, 47, and 79 at 30, 44, and 70 GHz respectively) such that the total integration time over the baseline corresponds approximately to one second. This selection is based on a compromise between computational load and map quality, and we find that shortening the baselines below one second has practically no effect on the residual noise.

In order to create maps in the maximum-likelihood approach, the noise covariance matrix of the problem has to be specified. In general, we use a white noise covariance matrix. The pipeline allows the use of different user-defined weighting schemes. The maps being released are made using the horn-uniform weighting scheme with

$$C_w^{-1} = \frac{2}{\sigma_M^2 + \sigma_S^2}\,, \qquad (1)$$

where σ_M and σ_S are the white noise sensitivities of the Main and Side radiometers of a given horn, and these radiometers are weighted equally.

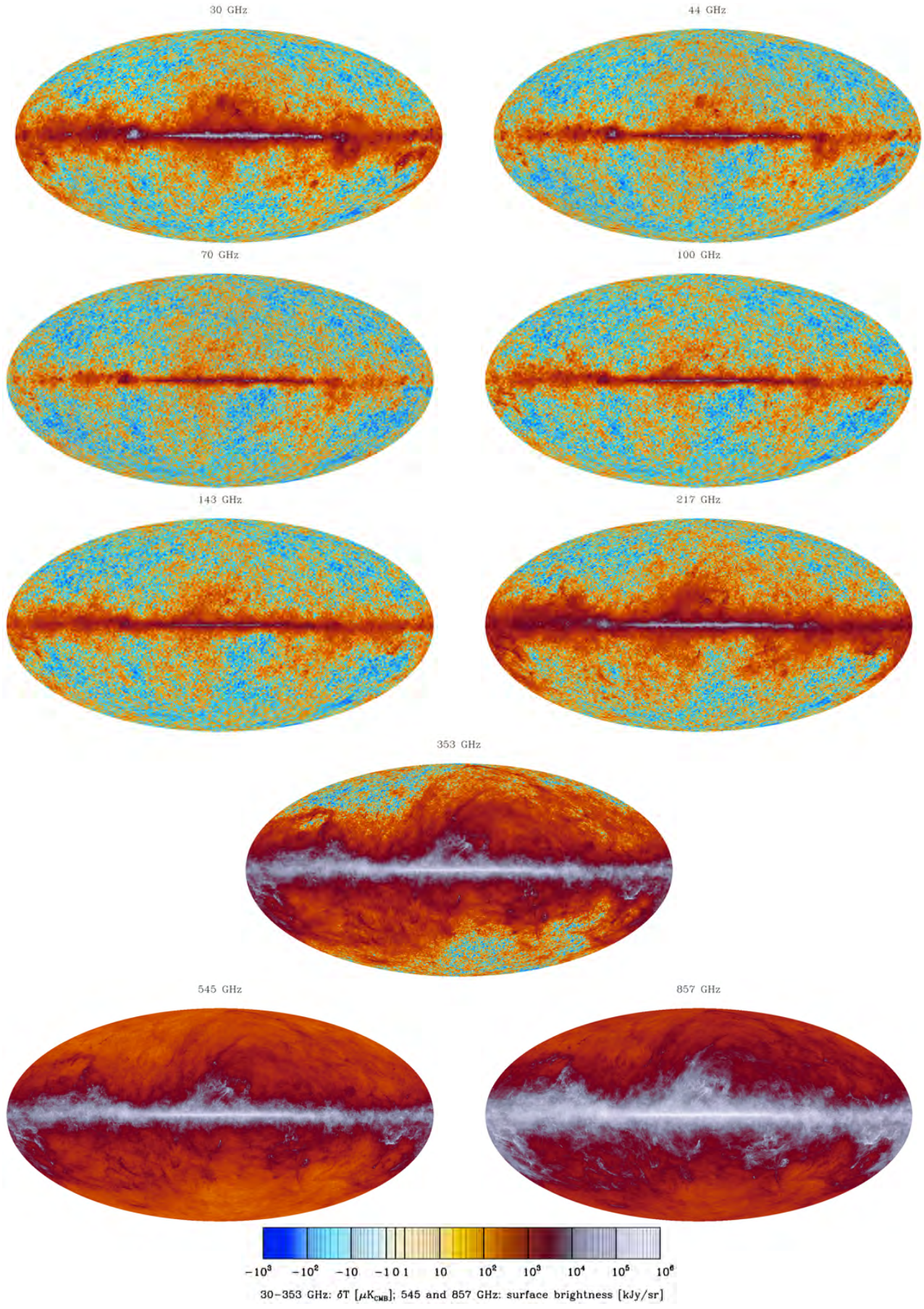

Fig. 9. The nine *Planck* frequency maps show the broad frequency response of the individual channels. The color scale (shown below) has been tailored to show the full dynamic range of the maps.

We also create half-ring maps[9] using the same algorithm as for the released maps. A time-weighted difference between the first-half and second-half ring maps captures the noise properties directly from the data, but only for noise components whose frequency is $f \gtrsim 2/20\mathrm{min} = 1.7\,\mathrm{mHz}$, i.e., half the duration of the pointing period.

A zero level is determined for each LFI map in two independent ways:

- a cosecant model of latitudinal Galactic emission is fitted to the region $-90° < b < -15°$.
- the CMB from a clean patch of the sky is removed, and the remaining level is set to zero.

The two methods yield consistent results, and the level estimated from the first method is subtracted from the LFI maps (see Table 6).

6.2.2. HFI

The maps for the HFI channels are made by projecting the processed HEALPix rings built from the TOIs (Sect. 5.3.2) onto a HEALPix map (Planck Collaboration VI 2013; Planck Collaboration ES 2013). First, maps of individual rings are created by averaging filtered and baseline-subtracted TOIs into HEALPix pixels. Second, these ring maps are used for the photometric calibration of each detector (see Sect. 5.6). Then, these calibrated ring maps are combined via a least-squares destriping procedure (Planck Collaboration VIII 2013) that estimates a constant offset per ring using the cross-linking of the *Planck* scan strategy. Various maps are produced, corresponding to individual detectors, subsets of detectors at each frequency, and all the detectors at a given frequency. Half-ring maps are also built, using only the first and second halves of all rings, to monitor the statistical and systematic noise properties of the maps.

Because of its rotation and orbit, contributions to the *Planck* TOI from far-sidelobe pickup (mostly of the Galaxy at high frequencies) and of the Zodiacal light do not project directly onto fixed sky coordinates, and are a significant contaminant at 353 GHz and above. Hence, they must be estimated and removed separately (Planck Collaboration XIV (2013) and Planck Collaboration ES (2013)). In this release we provide two sets of HFI maps:

- a "default" set of maps from which neither far-sidelobe straylight nor zodiacal emission has been removed. These default maps are the ones that we use for extraction of the CMB map to search for non-Gaussianity. The rationale for not removing zodiacal emission is that it has been shown to produce artifacts during component separation (Planck Collaboration XII 2013). For CMB extraction, it is more effective to let the the component separation method (Sect. 7.1) remove zodiacal emission.
- a second set of maps from which an estimate of far-sidelobe straylight and zodiacal emission have been removed (Planck Collaboration XIV 2013). To achieve this, the zodiacal emission is estimated by fitting to the *COBE* emission model (Kelsall et al. 1998) and subtracted from the TOI before mapmaking. Zodiacal emission is removed at all frequencies. Far-sidelobe emission is estimated and removed at 545 and 857 GHz only. This is the set of maps which should be used for work related to diffuse foregrounds.

[9] A half-ring map is built from data acquired from either the first half or the second half of the total duration of each ring.

The 2013 HFI maps contain significant Galactic CO emission. Specific component separation pipelines yield separate estimates of it (see Sect. 8.2.2 and (Planck Collaboration XIII 2013)) optimized for different scientific uses.

The HFI frequency maps contain an offset that arises from two different components, the diffuse interstellar medium and the cosmic infrared background. The offset level due to the diffuse interstellar medium is estimated by correlating the HFI maps with a map of the column density of neutral hydrogen. This offset (reported in Table 6) should be removed from the released maps before carrying out scientific analysis of Galactic emission. The mean level contributed by the cosmic infrared background at each frequency is estimated by means of an empirical model that fits the current data. For analysis of total emission, the CIB level (see Planck Collaboration VIII (2013)) must be added to the released maps after readjustment for the interstellar medium offset described above.

The resulting HFI maps are shown in Fig. 9.

6.3. Map Units

Broad-band detection instruments like those carried by *Planck* measure radiative power through a filter or pass-band: either the flux density times effective area for unresolved sources, or the intensity times throughput (collecting area times solid angle) for extended emission. The calibration source for *Planck* is the CMB dipole, except for the two highest frequency channels (545 and 857 GHz), for which planets are used. If the target source has the same Spectral Energy Distribution (SED) within the pass-band as the calibrator, we can simply find the true brightness from the ratio between the response to the target and the response to the calibrator. In practice only CMB anisotropies satisfy this condition; in general target and calibrator have different SEDs. The raw brightness values in the maps cannot then be taken as monochromatic values; rather, they represent the integral of the detected power weighted by the bandpass.

To allow comparison with other measurements and with models, the brightness of the CMB-calibrated channels is given as differential CMB temperature, $\Delta T_{\mathrm{CMB}} = \Delta I_\nu / (dB_\nu/dT)_{T_0}$, where B_ν is the Planck function, $T_0 = 2.7255\,\mathrm{K}$ (Fixsen 2009), and ν is a specified reference frequency for each channel[10].

The 545 and 857 GHz channel maps are instead given in intensity units ($\mathrm{MJy\,sr^{-1}}$), assuming the reference SED $I_\nu = I_0 \times (\nu_0/\nu)$ (used previously by *IRAS* and *COBE*-DIRBE). Thus for all *Planck* channels the intensity (or flux density for unresolved sources) is always attached to a choice of both a reference frequency and an assumed SED.

Each foreground observed in the *Planck* band has a different SED (power law, modified black body, SZ distortion, CO lines). To evaluate intensities for these SEDs, e.g., for component separation, we provide unit conversions and colour corrections for each band (also available as a downloadable code), where the corrected values are such that the power integrated in the spectral bandpass and throughput is equal to the measured power. They are described for LFI in Planck Collaboration V (2013), which tabulates conversion from the CMB fluctuation SED to power-laws with various indices, and for HFI in Planck Collaboration IX (2013), which gives conversions between the two standard HFI SEDs (CMB fluctuation and *IRAS* standard), and also the Compton y_{sz} parameter. In addition, a unit con-

[10] Our definition of ΔT_{CMB} is linearized, and deviates significantly from the true variation in the equivalent blackbody temperature in the brightest regions of the 217 and 353 GHz maps.

version and colour correction software tool (UcCC) covering all *Planck* bands is provided as part of the data release and described in Planck Collaboration IX (2013). Users are cautioned to read the detailed descriptions carefully, as in general a sequence of steps is required to convert from the units and assumed SED of the map calibration to the those appropriate for a given foreground. Our colour conversions are uniformly cast as a multiplicative correction, yielding the brightness at the standard band reference frequency for the required SED. It would also have been possible in most cases to quote an "effective frequency" at which the numerical value of the map brightness applies to the required SED, but this is less practical in general and cannot be applied at all to line emission.

6.4. Map characterization

Null tests are a powerful way to evaluate the quality of LFI and HFI maps. Among these are half-ring difference maps (which capture noise properties), and survey-to-survey differences (which capture different types of systematic signals). Simulation of known systematics is also a viable way to validate the effects seen in the real data, especially in survey-to-survey differences. Comparison of angular cross-power spectra of maps made with individual detectors within a frequency band, and of maps at different frequencies, is used to give confidence in the results. Many such tests have been implemented, as described in Planck Collaboration II (2013); Planck Collaboration III (2013); Planck Collaboration IX (2013); Planck Collaboration V (2013) for LFI and Planck Collaboration VI (2013); Planck Collaboration VII (2013); Planck Collaboration VIII (2013) for HFI. Table 5 summarises the sources contributing to uncertainties at map level, and the actual uncertainty levels associated to each map are summarised in Table 6. For residual systematic levels, we refer the reader to Planck Collaboration III (2013) (LFI) and Planck Collaboration VI (2013) (HFI).

Finally, comparison of data at map and power spectrum level obtained independently by LFI and HFI provides an important check on the results; such tests are described in detail in Planck Collaboration XI (2013).

6.5. Consistency tests

In Planck Collaboration XI (2013) the agreement between the *Planck* HFI and LFI data is analyzed, showcasing the advantage of having employed two different detector technologies on the same telescope and satellite platform.

First we compare sky maps by pairs of frequencies from 44 to 217 GHz, then we investigate the power spectra of these maps in various ways for a more refined quantitative comparison.

Long-term stability in CMB experiments is necessary to avoid large scale artifacts in the maps. *Planck* maps are free from serious large- to intermediate-scale imperfections: extensive examination of difference maps between different frequency channels consistently demonstrates that we achieve deep nulling of the CMB anisotropy signal, and reveals in an immediate and interesting manner the foreground residuals. Figure 10 shows this spectacularly in the case of the key comparison between 70 and 100 GHz, the closest frequencies between the two instruments, and the closest to the foreground minimum. The CMB structure at high galactic latitude disappears in the difference made in $K_{\rm cmb}$ units as shown by the green (very close to zero) uniform background. Of course the Galactic emission (primarily from CO in the 100 GHz channel) stands out at low latitudes with its different SED from the CMB.

Spectral analysis allows a more quantitative assessment. In Planck Collaboration XI (2013) we carry out detailed cross-spectrum comparisons between neighbouring channels at 70, 100, and 143 GHz, thus checking consistency between LFI and HFI, and agreement between the main CMB channels overall. The comparisons are in terms of cross-spectra computed on half ring maps, both sum and difference, in which the CMB signal should disappear from the difference maps if the relative calibration is perfect. These results are compared to direct differences between power spectra, and the combination of methods allows quantitative comparison with the expected levels of residual foregrounds, and overall provides a confirmation of the expected level of calibration uncertainty and foreground residual levels. The results demonstrate a spectral consistency between the LFI 70 GHz and HFI 100 GHz channels of a few tenths of a percent, displaying one of the best agreements achieved to date between different CMB instruments, and achieved with instruments employing quite different technology.

As described in Section 5.6, residual dipoles in the calibrated maps test the quality of calibration with respect to the *WMAP* dipole. These residuals are less than 0.1 % for the HFI CMB channels (Planck Collaboration VIII 2013) and 0.2 % to 0.3 % for LFI (Planck Collaboration II 2013). Recalibration of the CMB channels on the CMB anisotropies with respect to a common reference (143 GHz) is shown in Fig. 11, for two ranges of multipoles (50–300 and 300–700). The recalibration coefficients for the bands 70 to 217 GHz are all within 0.2% (44 and 353 GHz are at the 0.8 % level). This test again demonstrates excellent inter-calibration both within the HFI CMB channels and between these and the 70 GHz LFI channel, which, once again, uses a different detector technology and is subject to different instrumental systematic effects and data processing.

We can extend the spectral comparisons of neighbouring *Planck* channels to power spectra of component-separated CMB maps from *Planck* and from *WMAP*. Fig. 12, taken from Planck Collaboration XV (2013), shows that the *WMAP* spectrum lies systematically above the *Planck* spectra, with the difference being of order $20\,\mu{\rm K}^2$ at $\ell < 25$, and possibly rising slowly with ℓ (see Planck Collaboration XI (2013)). At higher multipoles, the comparison between *WMAP* and *Planck* is discussed in Appendix A of Planck Collaboration XVI (2013), and shows that a multiplicative factor of 0.976 applied to the *WMAP* U+V spectrum brings it into a remarkable point-by-point agreement with the *Planck* 100×100 GHz spectrum over the range $50 < \ell < 400$.

Figure 12 also shows that at low multipoles, the transfer functions in Planck are very stable with respect to *WMAP* for $\ell < 60$. Figure 17 of Planck Collaboration XV (2013) shows very consistent residuals in the whole high ℓ range from the three HFI CMB channels when the best *Planck* CMB and foreground model is removed. This shows that the transfer functions are closely consistent with each other.

7. CMB Science Products

With *Planck* we can study the millimetre- and submillimetre-wave sky in greater detail than previously possible. Component separation - the process of separating the observed sky emission into its constituent astrophysical sources - is consequently a central part of our data analysis. It is a necessary step to reach the mission's goal of measuring the primary CMB temperature anisotropies to a precision limited mainly by uncertainty

Table 5. Contributors to uncertainties at map level

Uncertainty	Applies to	Method used to assess uncertainty	
		LFI	HFI
Gain calibration standard	All sky	*WMAP* dipole	100–353 GHz: *WMAP* dipole 545–857 GHz: Planet model
Zero level	All sky	Galactic cosecant model Comparison with *WMAP*	Galactic zero: correlation to HI CIB: empirical model
Beam uncertainty	All sky	GRASP models via Febecop	Beam MC realizations via `Quickbeam`
Color corrections	non-CMB emission	Comparison of ground/flight bandpass leakages	Ground measurements
Beam Color corrections	non-CMB emission	GRASP models	GRASP models
Residual systematics	All sky	Null tests	Null tests

Table 6. Properties of the *Planck* maps[a]

Property	Applies to	Frequency [GHz]								
		30	44	70	100	143	217	353	545	857
Effective frequency [GHz]	Mean	28.4	44.1	70.4	100	143	217	353	545	857
Noise rms per pixel [μK_{CMB}]	Median	9.2	12.5	23.2	11	6	12	43	...	...
[MJy sr^{-1}]	Median	...	...	...	...	...	...	...	0.0149	0.0155
Gain calibration uncertainty[b]	All sky	0.82 %	0.55 %	0.62 %	0.5 %	0.5 %	0.5 %	1.2 %	10 %	10 %
Zero level[c] [MJy sr^{-1}]	All sky	0	0	0	0.0047	0.0136	0.0384	0.0885	0.1065	0.1470
Zero level uncertainty [μK_{CMB}]	All sky	±2.23	±0.78	±0.64	...	...	...	...	...	...
[MJy sr^{-1}]	All sky	...	...	...	±0.0008	±0.001	±0.0024	±0.0067	±0.0165	±0.0147
Color correction unc.[d]	non-CMB emission	0.1β %	0.3β %	0.2β %	$0.11\Delta\alpha$ %	$0.031\Delta\alpha$ %	$0.007\Delta\alpha$ %	$0.006\Delta\alpha$ %	$0.020\Delta\alpha$ %	$0.048\Delta\alpha$ %
Beam Color correction unc.[e]	non-CMB emission	0.5 %	0.1 %	0.3 %	<0.3 %	<0.3 %	<0.3 %	<0.5 %	<2.0 %	<1.0 %

[a] The HFI default maps do not include removal of zodiacal emission.

[b] Includes the absolute uncertainty (0.24 %) of the calibration standard used, which is the CMB dipole estimated by WMAP7 (Hinshaw et al. 2009).

[c] A zero level has been removed from the LFI maps (−300.84, −22.83, and −28.09 μK_{CMB} at 30, 44, and 70 GHz), but not from the HFI maps. The value given in this table corresponds to an estimate zero level of Galactic emission (Planck Collaboration VIII 2013) in the maps which include zodiacal emission. For total emission studies, the level contributed by the Cosmic Infrared Background must be added (Planck Collaboration VIII 2013).

[d] β is the temperature spectral index of the source, see Planck Collaboration IV (2013). $\Delta\alpha$ is the difference in source spectral index from −1 (i.e., νI_ν = constant for $\alpha = -1$ following the IRAS convention), see Planck Collaboration IX (2013). No uncertainties are assumed on α and β.

[e] For the HFI channels, we show the upper limit in solid angle change due to color correction from a planet spectrum source (roughly ν^2) to *IRAS* convention (ν^{-1}).

in foreground subtraction, and also to produce maps of foreground components for astrophysical studies. To take full advantage of *Planck*'s exceptional data set, we apply a variety of component separation techniques, some developed specifically for the *Planck* analysis.

A number of Galactic and extragalactic emissions contribute to the observed sky over the frequency range spanned by *Planck*. Synchrotron radiation, caused by cosmic ray electrons spiraling in the Galactic magnetic field, dominates the Galactic emission at the lowest frequencies (30, 44 GHz), falling with a spectrum approximating a power law in brightness temperature as $T \sim \nu^\alpha$ with $\alpha \approx -3$. Free-free emission from ionized interstellar gas and HII regions is also prominent, decreasing with a power-law index $\alpha = -2.15$. Anomalous microwave emission (AME), potentially due to the de-excitation of rotating dust grains spun up by photons in the interstellar radiation field, has a spectrum that peaks somewhere below 30 GHz, and falls rapidly with frequency through the *Planck* bands. At frequencies above 70 GHz, thermal emission from dust grains heated to near 20 K becomes the dominant Galactic emission, rising with frequency according to a gray-body spectrum with emissivity $\epsilon \propto \nu^{1.5-2}$. In addition, we observe line emission from CO at 100, 217 and 353 GHz.

In the best half of the sky at high Galactic latitudes, foregrounds in our favoured CMB channels (70–217 GHz), are dominated at $\ell < 50$ by dust in the Milky Way, and at $\ell > 200$ by extragalactic radio sources at low frequencies and infrared sources at 217 GHz. Some of these sources are seen as individual objects by *Planck*, while most form an unresolved background. In the case of IR sources, this is the CIB, which has a spectrum close to that of Galactic thermal dust. There is also a contribution from secondary CMB anisotropies, notably the Sunyaev-Zeldovich effect produced by galaxy clusters. The strongest clusters are detected as individual compact sources, but the weakest contribute to an unrersolved Sunyev-Zeldovich foreground.

The extraction of cosmological information from the *Planck* maps follows two main paths: the search for spatial non-Gaussianities of the anisotropies, and the estimation of the parameters of models of the Universe. For the former, it is crucial to preserve the spatial shape of the anisotropies over the largest possible area of the sky; however, astrophysical foregrounds are important contaminants over a significant fraction of the sky. It is therefore unavoidable for the study of non-Gaussianities to remove foregrounds at map level. This is not necessarily the best route for the determination of cosmological model parameters, which are based on fitting model predictions of the angular power spectra of the anisotropies; for this purpose, it is also possible to separate astrophysical foregrounds at high-ℓ at the power spectrum level over a more limited fraction of the sky.

In summary, the path that we follow in the 2013 release of *Planck* results is:

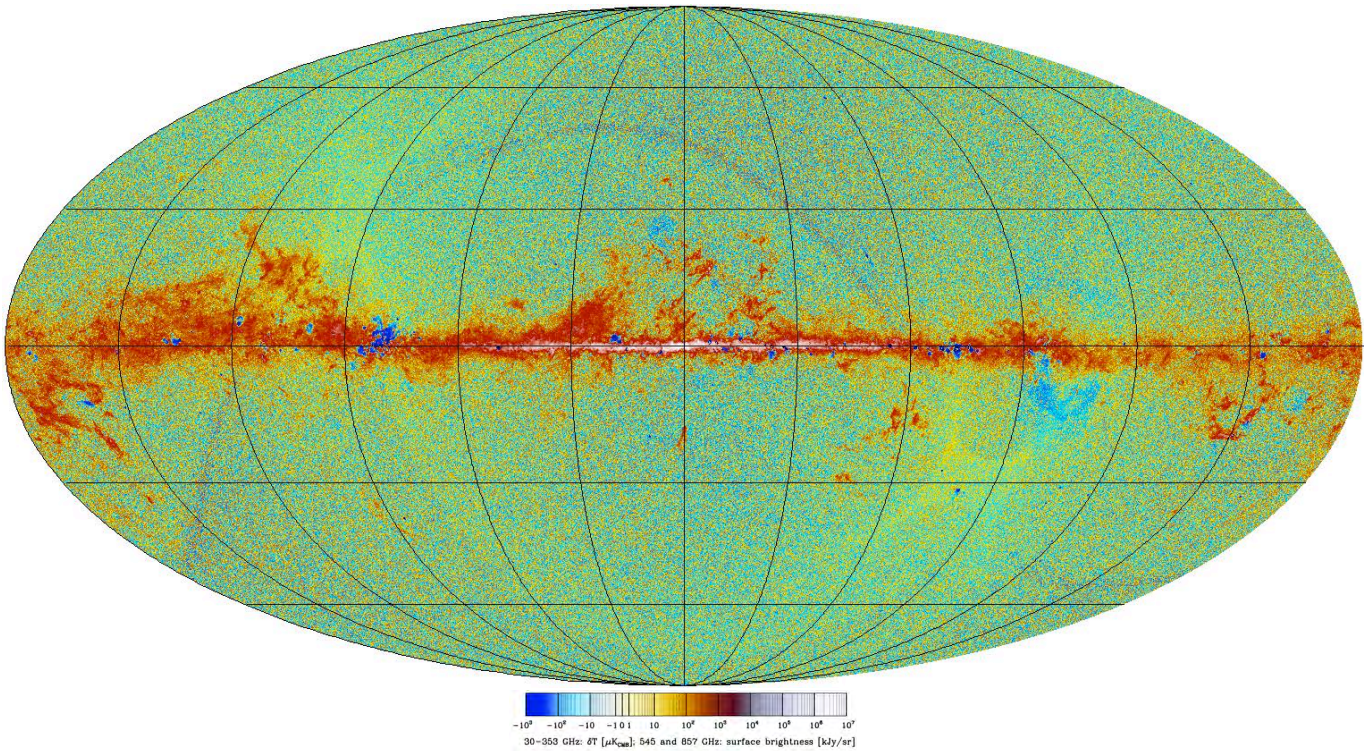

Fig. 10. One panel of Figure B.2 from (Planck Collaboration XI 2013), showing the difference map 100 GHz − 70 GHz.

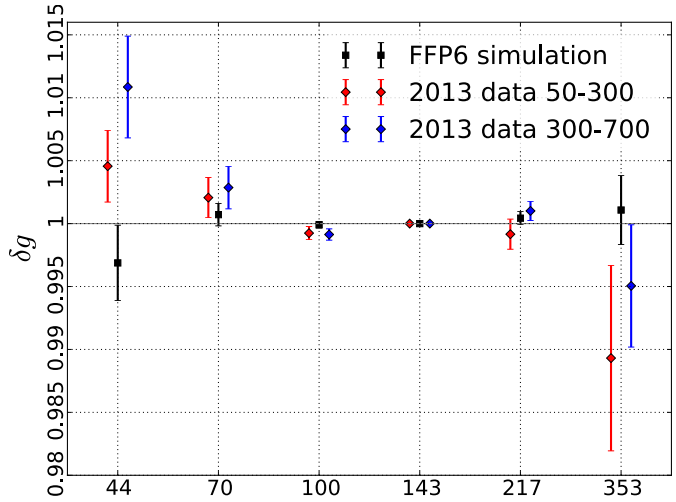

Fig. 11. Recalibration factor maximizing the CMB consistency in in simulations (black) and in the data considering different multipole ranges (red and blue), at each Planck frequency in GHz given on the horizontal axis. This is Figure 35 from (Planck Collaboration VI 2013).

- for non-Gaussianity analysis, we use a component-separated map of the anisotropies (see Sect. 7.1, Planck Collaboration XII (2013))
- for parameter estimation, we use a likelihood code (Planck Collaboration XV 2013) based at low-ℓ on a component-separated CMB map, and at high-ℓ on a self-consistently determined set of parameters of physically-motivated foreground models simultaneously with the best-fit CMB model (see Sect. 7.3.1).

The generation of the *Planck* CMB-science products is illustrated in Fig. 13.

7.1. CMB map extraction

Our approach to component separation for *Planck*, and more specifically to extraction of a CMB map, is described in detail in Planck Collaboration XII (2013). A single component separation technique cannot extract the maps for all the known intensity diffuse components (CMB and foregrounds) as the number of parameters needed to describe them even minimally exceeds the number of frequency channels. Four different methods were optimized to produce a CMB map based on the *Planck* maps alone, i.e., without the addition of any other external data: SMICA, an implementation of independent component analysis of power spectra; NILC, a needlet-based version of internal linear combination; Commander-Ruler, a pixel-based version of parameter and template fitting; and SEVEM, template fitting using the lowest and highest freuqency bands.

The use of several methods giving consistent results is a useful cross-validation tool, and demonstrates the robustness of the CMB map obtained by *Planck*. All three algorithms were run on the FFP6 simulations of *Planck* data (see Sect. 5.2). Based on this comparison and on statistical tests conducted on the real *Planck* data (consistency with *Planck* likelihood, correlation with external templates, local distribution of skewness and kurtosis, and more), one method (SMICA) was selected to extract a CMB map useful for non-Gaussianity and related searches on the largest possible fraction of the sky; this is the map used as the main source in a wide variety of analysis presented in this release (Planck Collaboration XXIII 2013; Planck Collaboration XXIV 2013; Planck Collaboration XXVI 2013; Planck Collaboration XXV 2013; Planck Collaboration XVII 2013; Planck Collaboration XIX 2013). However, we find that all three methods yield CMB maps that are adequate for similar analysis, although their performance varies from method to method (Planck Collaboration XII 2013), and some may be more suitable for specific studies. We therefore release all three maps,

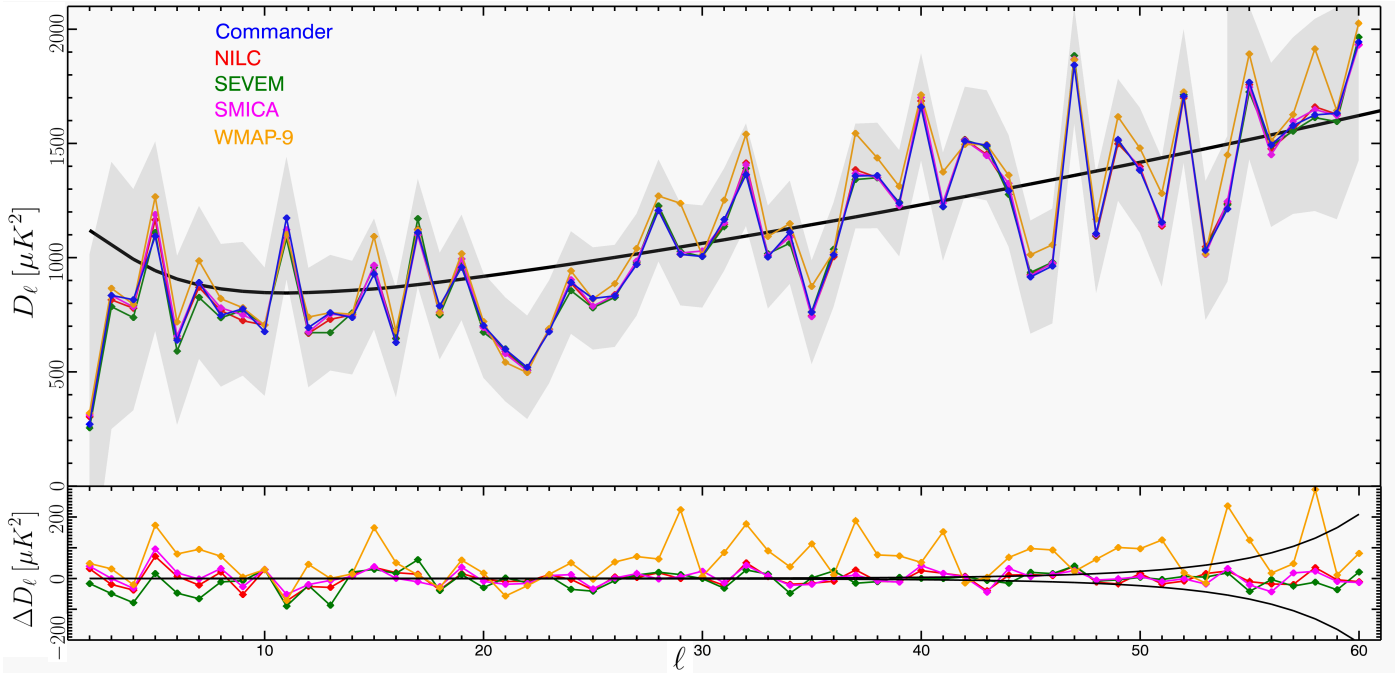

Fig. 12. Top panel: temperature power spectra evaluated from downgraded *Planck* maps, estimated with `Commander`, `NILC`, `SEVEM`, or `SMICA`, and the 9-year *WMAP* ILC map, using the `Bolpol` quadratic estimator. The grey shaded area indicates the $1\,\sigma$ Fisher errors while the solid line shows the *Planck* ΛCDM best fit model. Bottom panel: Power spectrum differences for each algorithm/data set relative to the `Commander` spectrum, estimated from the spectra shown in the panel above. The black lines show the expected $1\,\sigma$ uncertainty due to (regularization) noise. This is Fig. 34 of Planck Collaboration XV (2013)

to offer the users a grasp of the uncertainties and level of robustness associated to the different assumptions made in these methods.

The SMICA map (see Fig. 14) estimates the CMB over about 97 % of the sky, with the remaining area replaced with a constrained Gaussian realization. It has an angular resolution of 5′, but its harmonic content is cut off for $\ell > 4000$. In the pixel domain, the noise has an average RMS of about 17 μK (for the cut off at $\ell = 4000$), but its distribution is highly inhomogeneous (see Fig. 15).

Figure 16 illustrates the signal-to-noise ratio reached by *Planck* for the CMB signal. It shows, for the SMICA rendering, the angular spectrum of the estimated CMB map, of the associated half-ring noise and their difference (both raw and smoothed) after beam correction. The latter noise-corrected spectrum shows the CMB spectrum plus any remaining contamination. Note how the seventh acoustic peak is visible and how the SNR reaches unity (for single multipoles) at $\ell \sim 1700$.

All three methods used yield also a set of "residual" maps that contain astrophysical foregrounds and other sources of noise. As noted previously, the problem of component separation for intensity is such that these methods are not suitable to extract physically meaningful individual components, unless ancillary information is included in the process. Nonetheless, we do release the residual maps for analysis in conjunction with the extracted CMB maps.

Two additional CMB maps based on *Planck* data have been produced. They have been subjected to the same characterization as the three maps described above (Planck Collaboration XII 2013). They are:

- a low-resolution (∼1°) CMB map that is used within the *Planck* likelihood code as the input for low-ℓ (pixel-based) part of the code. The map was produced with the Commander algorithm (Planck Collaboration XII 2013), which incorporates physically-motivated parametric foreground models. In contrast to the other schemes developed to extract the CMB (see Sect. 7.1), it provides direct samples of the likelihood posterior. The Commander CMB map is not ideal for non-Gaussianity studies, due to its lower angular resolution, but it is good for the low-ℓ likelihood, which does not require high resolution and tolerates a high level of masking. This map is not provided separately in the 2013 release, but is packaged into the input data required by the code.
- a CMB map (at ∼7 arcmin resolution) is extracted using the Commander-Ruler algorithm together with a set of astrophysical components (see Sect. 8.2.3, and Planck Collaboration XII (2013)). The algorithm was not optimised only for CMB extraction but for also for recovery of astrophysical foregrounds. Nonetheless, it performs comparably well to the other CMB maps up to $\ell \sim 1500$ in terms of power spectrum estimations and extraction of cosmological parameters, as is shown in Planck Collaboration XII (2013) and Planck Collaboration XV (2013).

7.2. CMB Lensing products

The high-resolution CMB fluctuations measured by *Planck* are perturbed by gravitational lensing, primarily sourced by the structure of the Universe on very large scales (near the peak of the matter power spectrum at 300 Mpc comoving) at relatively high redshifts (with a kernel peaking at $z \sim 2$). Lensing blurs the primary CMB fluctuations, slightly washing out the acoustic peaks of the CMB power spectrum (Planck Collaboration XV 2013; Planck Collaboration XVI 2013). Lensing also introduces several distinct non-Gaussian statistical signatures into our maps, which are studied in detail in Planck Collaboration XVII

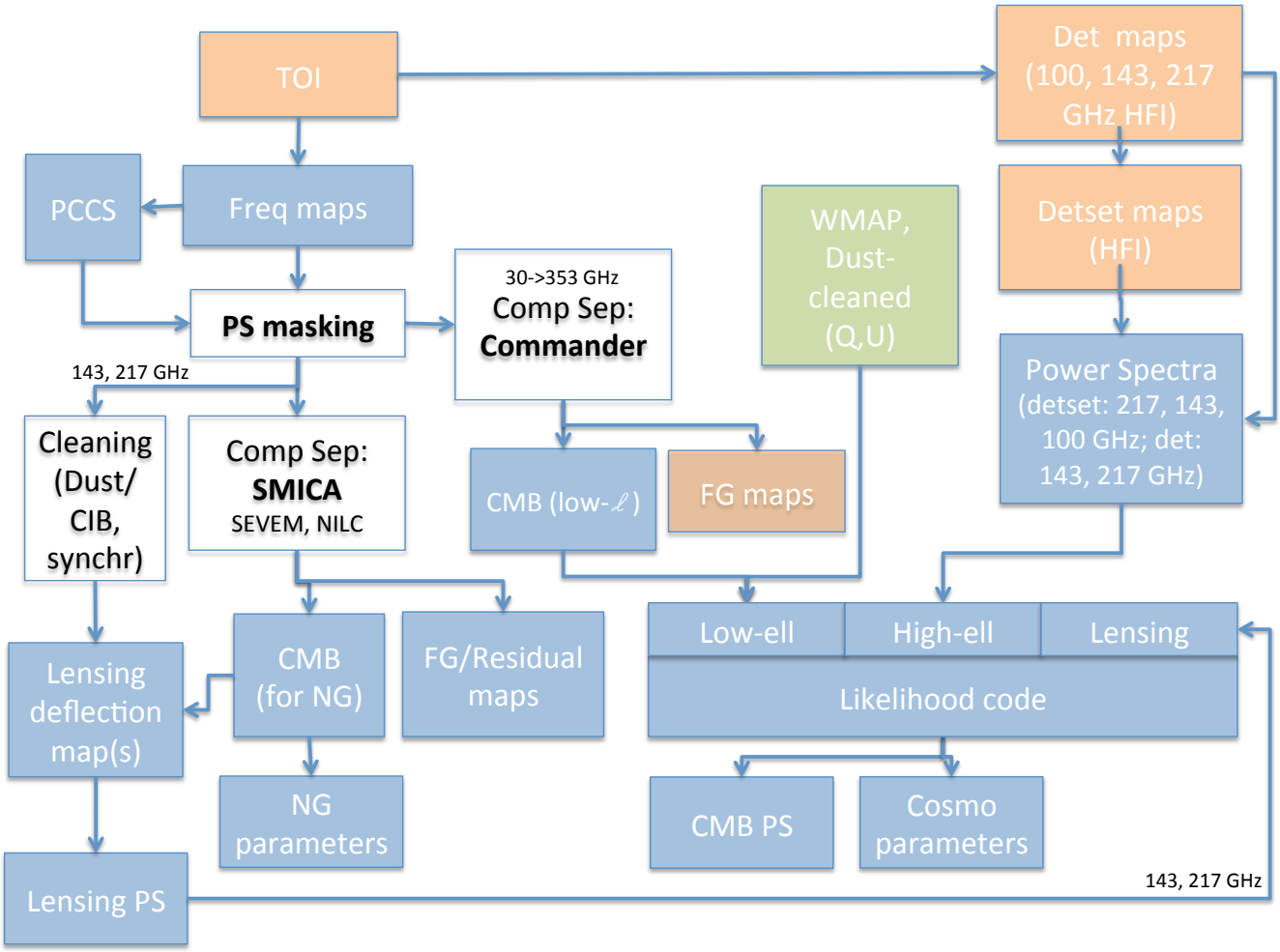

Fig. 13. This diagram outlines the generation of the CMB-science products being delivered by *Planck* (in blue). Products in green are external, and products in orange are not being delivered in the current release. Each product delivered is accompanied by specific data characterizing it (not shown on the diagram). This diagram does not include other data used for parameter estimations, either from *Planck* itself (lensing, CIB, SZ) , or from other CMB experiments (SPT, ACT, etc).

(2013). The deflections caused by lensing on such large scales are weak, with an RMS of $\sim 2.5'$, and their effect may be represented as a remapping by the gradient of a lensing potential $\phi(\hat{n})$ as

$$T(\hat{n}) = \tilde{T}(\hat{n})(\hat{n} + \nabla\phi(\hat{n})), \quad (2)$$

where $\hat{n}$ is the direction vector, and $\tilde{T}$ is the unlensed CMB. In Planck Collaboration XVII (2013) we reconstruct a map of the lensing potential $\phi(\hat{n})$, as well as estimates of its power spectrum $C_L^{\phi\phi}$. Although noisy, the *Planck* lensing potential map represents a projected measurement of all dark matter back to the last scattering surface, with considerable statistical power. In Fig. 7.2 we plot the *Planck* lensing map, and in Fig. 18 we show an estimate of its signal power spectrum.

As a tracer of the large scale gravitational potential, the *Planck* lensing map is significantly correlated with other tracers of large scale structure. We show several representative examples of such correlations in Planck Collaboration XVII (2013), including the NVSS quasar catalog (Condon et al. 1998), the MaxBCG cluster catalog (Koester et al. 2007), luminous red galaxies from SDSS Ross et al. (2011), and a survey of infrared sources from the WISE satellite (Wright et al. 2010). The strength of the correlation between the *Planck* lensing map and such tracers provides a fairly direct measure of how they trace dark matter; from our measurement of the lensing potential, the *Planck* maps provide a mass survey of the intermediate redshift Universe, in addition to a survey of the primary CMB temperature and polarization anisotropies.

7.3. Likelihood code

7.3.1. CMB likelihood

We follow a hybrid approach to construct the likelihood for the *Planck* temperature data, using an exact likelihood approach at large scales, $\ell < 50$, and a pseudo-C_ℓ power spectrum at smaller scales, $50 < \ell < 2500$. This follows similar analyses in, e.g., Spergel et al. (2007). The likelihood is described more fully in (Planck Collaboration XV 2013); here we summarize its main features.

On large scales, the distribution for the angular power spectrum cannot be assumed to be a multivariate Gaussian, and the Galactic contamination is most significant. We use the multi-frequency temperature maps from LFI and HFI, in the range $30 < \nu < 353$ GHz, to separate Galactic foregrounds. This procedure uses a Gibbs sampling method to estimate the CMB map and the probability distribution of its power spectrum, $p(C_\ell|d)$,

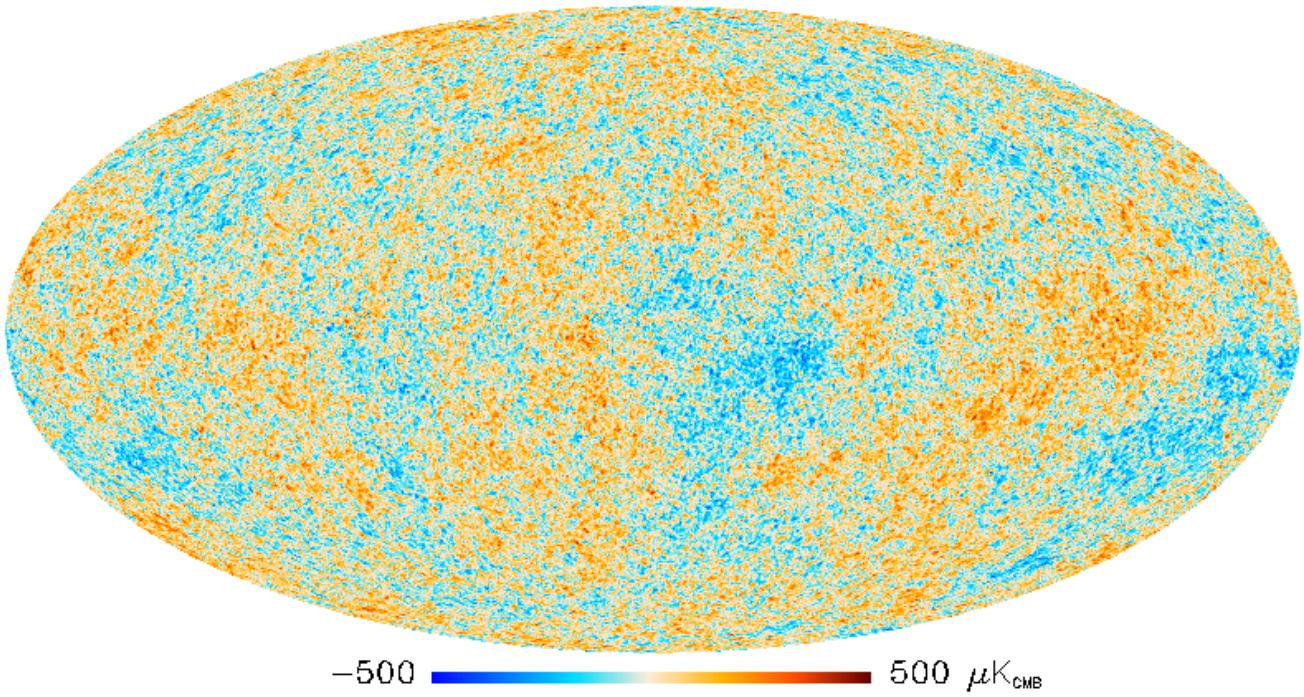

Fig. 14. The SMICA CMB map (with 3 % of the sky replaced by a constrained Gaussian realization).

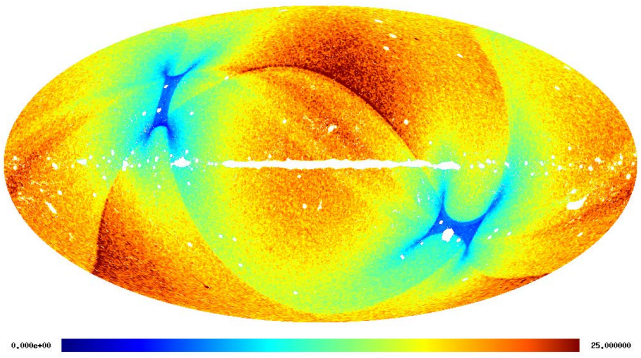

Fig. 15. Spatial distribution of the noise RMS on a color scale of 25 μK for the SMICA CMB map. It has been estimated from the noise map obtained by running SMICA through the half-ring maps and taking the half-difference. The average noise RMS is 17 μK. SMICA does not produce CMB values in the blanked pixels. They are replaced by a constrained Gaussian realization.

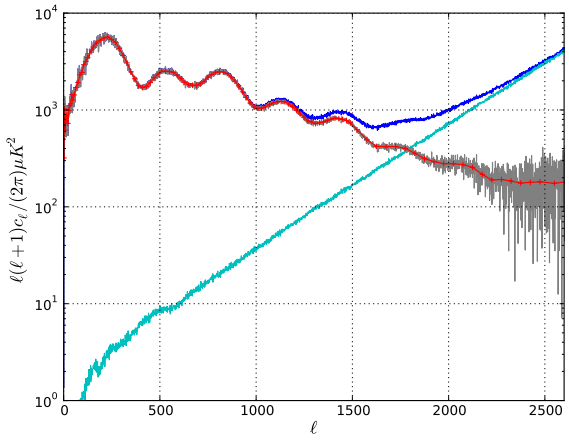

Fig. 16. Angular spectra for the SMICA CMB products, evaluated over the confidence mask, and after removing the beam window function: spectrum of the CMB map (dark blue), spectrum of the noise in that map from the half-rings (magenta), their difference (grey) and a binned version of it (red).

for bandpowers at $\ell < 50$, using the cleanest 87 % of the sky. We supplement this 'low-ℓ' temperature likelihood with the pixel-based polarization likelihood at large-scales ($\ell < 23$) from the *WMAP* 9-year data release (Bennett et al. 2012). These need to be corrected for the dust contamination, for which we use the *WMAP* procedure. However, we have checked that switching to a correction based on the 353 GHz *Planck* polarization data, the parameters extracted from the likelihood are changed by less than 1σ.

At smaller scales, $50 < \ell < 2500$, we compute the power spectra of the multi-frequency *Planck* temperature maps, and their associated covariance matrices, using the 100, 143, and 217 GHz channels, and cross-spectra between these channels[11]. Given the limited frequency range used in this part of the analysis, the Galaxy is more conservatively masked to avoid contamination by Galactic dust, retaining 58 % of the sky at 100 GHz, and 37 % at 143 and 217 GHz.

[11] interband calibration uncertainties have been estimated by comparing directly the cross spectra and found to be within 2.4 and 3.4×10^{-3} respectively for 100 and 217 GHz with respect to 143 GHz

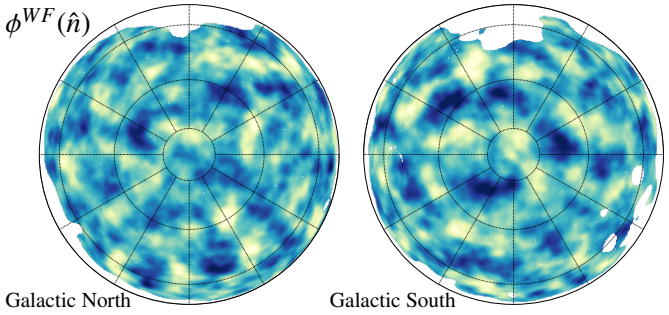

Fig. 17. Wiener-filtered lensing potential estimate reconstruction, in Galactic coordinates using orthographic projection. The reconstruction was bandpass filtered to $L \in [10, 2048]$. Note that the lensing reconstruction, while highly statistically significant, is still noise dominated for every individual mode, and is at best $S/N \approx 0.7$ around $L = 30$.

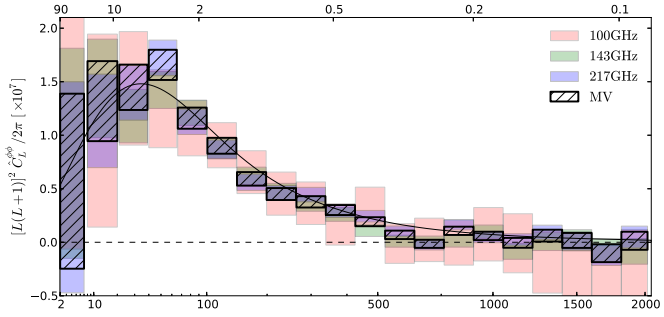

Fig. 18. Fiducial lensing power spectrum estimates based on the 100, 143, and 217 GHz frequency reconstructions, as well as the minimum-variance reconstruction that forms the basis for the *Planck* lensing likelihood.

Bright extragalactic point sources are also masked, using sources detected in the frequency range 100 to 353 GHz. Even after masking, power from unresolved extragalactic sources and thermal and kinetic Sunyaev-Zel'dovich effects make a significant contribution to the power spectra at the smallest angular scales probed by *Planck*. We model this excess power as the sum of multiple emission components, following similar analyses for previous CMB experiments (e.g. Sievers et al. (2013), Dunkley et al. (2011), Reichardt et al. (2012), Dunkley et al. (2013)).

In this 'high-ℓ' *Planck* likelihood, we model the total theoretical power as the sum of the lensed CMB, and a set of parameterized foreground emission spectra. Parameters are also introduced describing the beam uncertainties. We then simultaneously marginalize over all the additional "nuisance" parameters when estimating cosmological model parameters. This approach is designed to allow easy combination with data from the ACT and SPT experiments, which measure the mm-wave spectra from scales of $\ell \sim 200$ to $\ell < 10000$.

Unresolved extragalactic point sources are modelled as a Poisson power spectrum with one amplitude per frequency. The power spectra of the anisotropies associated with the correlated infrared background and the thermal and kinetic Sunyaev-Zeldovich are described by 4 amplitudes and power law indices and one correlation coefficients. In the mask used for the cosmology analysis, the CIB dominates at 217 GHz over the Galactic dust and the extragalactic foregrounds above $\ell \sim 500$. At higher ℓs (above 2500 at 217 GHz (and above 4000 at 143 GHz), the Poisson part dominates over the CMB. The foreground parameter values recovered in the likelihood analysis (Planck Collaboration XV 2013) are all compatible with cuurent knowledge of source counts and with the new *Planck* determination of the cosmic infrared background (Planck Collaboration XXXII 2013) and the thermal Sunyev-Zeldovich (Planck Collaboration XXI 2013), taking into account the rather large distribution of uncertainties for these weak foregrounds at the highest ℓs.

Removing the best-fitting extragalactic foreground model, and combining the multiple frequencies, we obtain the CMB temperature power spectrum shown in Fig. 19. *Planck* has now measured the first seven acoustic peaks to high precision. For comparison, we show in Fig. 20 a power spectrum estimated from the SMICA CMB map discussed in Section 7.1.

To test the robustness of the *Planck* power spectrum, we perform null tests between different detectors within a frequency band, between different surveys, and between frequency bands. To test the likelihood formalism, we perform a suite of tests modifying aspects including the foreground modeling, beam treatment, and angular range considered; we check that they have minimal effect on cosmological parameters. We also check that the same results are obtained using an independent power spectrum pipeline.

The most current version of the *Planck* likelihood software is made available with the 2013 data release, together with the multi-frequency power spectra, the best-fitting CMB power spectrum, and the maps and masks used to construct the power spectrum and likelihood.

7.3.2. Lensing likelihood

Based on our measurement of the lensing power spectrum described above in Sec. 7.3.1 and plotted in Fig. 18, we construct a simple Gaussian likelihood for bins of $C_L^{\phi\phi}$ from $40 \le L \le 400$ cut into 8 uniformly sized bins with $\Delta L = 45$. The bin size is such that we maintain some parameter leverage from the power spectrum shape information, while reducing the covariance between bins, thus allowing us to neglect it. We analytically marginalize over the beams, diffuse point source and first order bias uncertainty and include them in the covariance. The cosmological uncertainty on the normalization is accounted for by a first order correction. Our power spectrum measurement constrains the amplitude of a single amplitude parameter to a precision of ±4 %, corresponding to a 2 % constraint on the overall amplitude matter fluctuations σ_8. The construction of the lensing likelihood is described in Planck Collaboration XVII (2013), and its cosmological implications are discussed in detail in Planck Collaboration XVI (2013).

8. Astrophysical products

The generation of the *Planck* astrophysical products is outlined in Fig. 21.

8.1. The Planck catalogues

Many types of compact sources are expected in the *Planck* data: Galactic sources, radio galaxies, infrared galaxies, and clusters of galaxies. In January of 2011, the *Planck*Early Release Compact Source Catalogue (ERCSC) was published (Planck Collaboration XIV 2011), which included a catalogue of compact sources extracted independently from each map, a list of sources detected via the Sunyaev-Zeldovich effect, and a list of Galactic cold cores selected by temperature. In this 2013 release, an important advance is made for the first two of these lists.

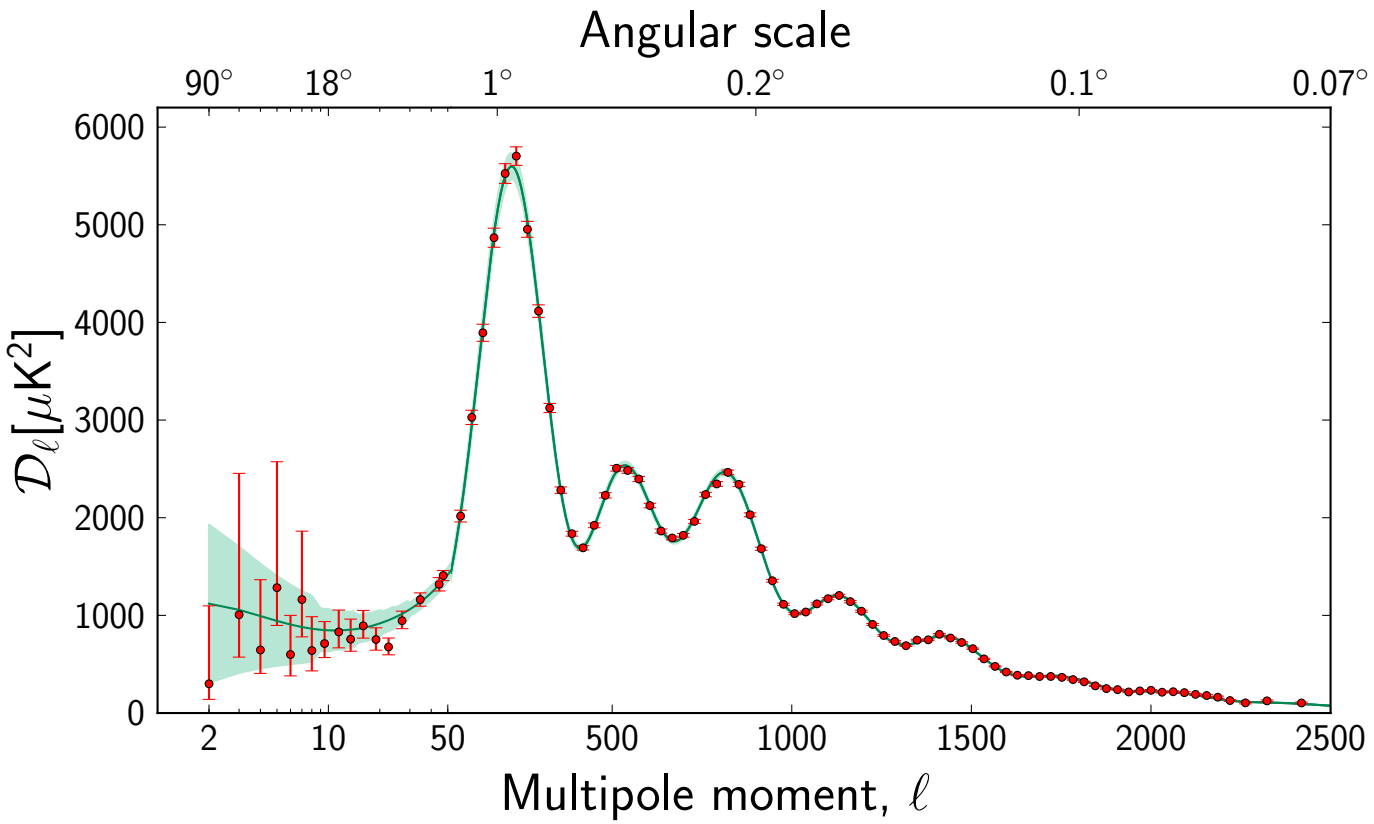

Fig. 19. The temperature angular power spectrum of the primary CMB from *Planck*, showing a precise measurement of seven acoustic peaks, that are well fit by a simple six-parameter ΛCDM theoretical model (the model plotted is the one labelled [Planck+WP+highL] in Planck Collaboration XVI (2013)). The shaded area around the best-fit curve represents cosmic variance, including the sky cut used. The error bars on individual points also include cosmic variance. The horizontal axis is logarithmic up to $\ell = 50$, and linear beyond. The vertical scale is $\ell(\ell+1)C_l/2\pi$. The measured spectrum shown here is exactly the same as the one shown in Fig. 1 of Planck Collaboration XVI (2013), but it has been rebinned to show better the low-ℓ region.

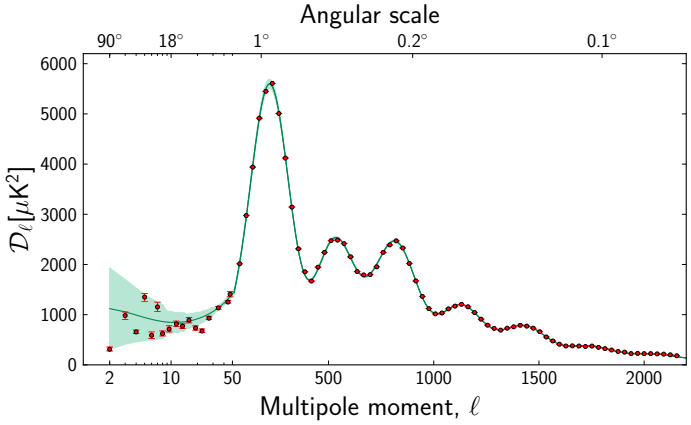

Fig. 20. The temperature angular power spectrum of the CMB, estimated from the SMICA *Planck* map. The model plotted is the one labelled [Planck+WP+highL] in Planck Collaboration XVI (2013). The shaded area around the best-fit curve represents cosmic variance, including the sky cut used. The error bars on individual points do not include cosmic variance. The horizontal axis is logarithmic up to $\ell = 50$, and linear beyond. The vertical scale is $\ell(\ell+1)C_l/2\pi$. The binning scheme is the same as in Fig. 19.

8.1.1. Main catalogue

The *Planck* Catalogue of Compact Sources (PCCS, Planck Collaboration XXVIII (2013)) is a list of compact sources detected by *Planck* over the entire sky, and which therefore contains both Galactic and extragalactic objects. No polarization information is provided for the sources at this time. The PCCS differs from the ERCSC in its extraction philosophy: more effort has been made on the completeness of the catalogue, without reducing notably the reliability of the detected sources, whereas the ERCSC was built in the spirit of releasing a reliable catalog suitable for quick follow-up (in particular with the short-lived *Herschel* telescope). The greater amount of data, different selection process and the improvements in the calibration and map-making processing (references) help the PCCS to improve the performance (in depth and numbers) with respect to the previous ERCSC.

The sources were extracted from the 2013 *Planck* frequency maps (Sect. 6), which include data acquired over more than two sky coverages. This implies that the flux densities of most of the sources are an average of three or more different observations over a period of 15.5 months. The Mexican Hat Wavelet algorithm (López-Caniego et al. 2006) has been selected as the baseline method for the production of the PCCS. However, one additional methods, MTXF (González-Nuevo et al. 2006) was implemented in order to support the validation and characterization of the PCCS.

The source selection for the PCCS is made on the basis of Signal-to-Noise Ratio (SNR). However, the properties of the background in the *Planck* maps vary substantially depending on frequency and part of the sky. Up to 217 GHz, the CMB is the

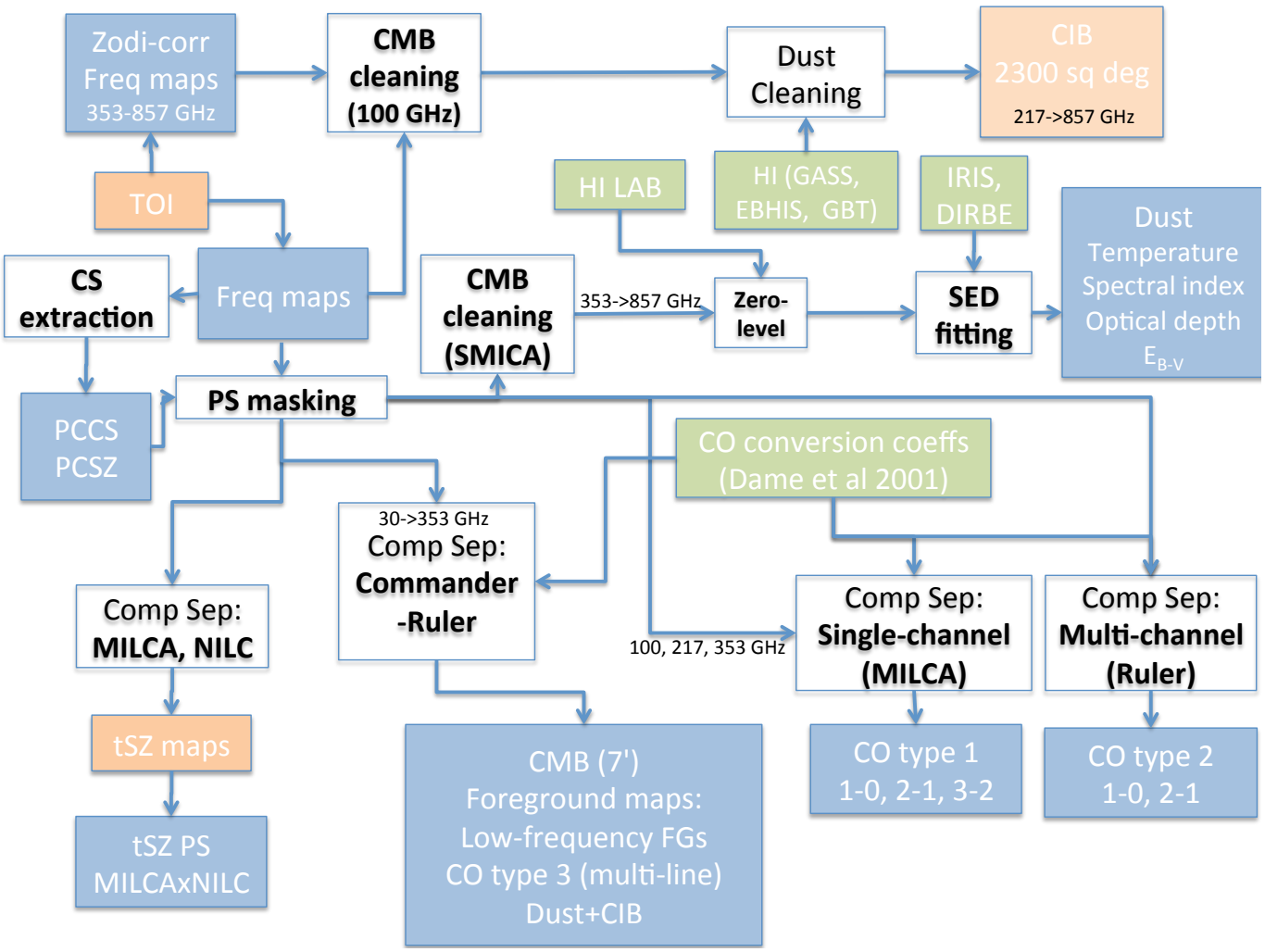

Fig. 21. This diagram outlines the generation of the Astrophysical products being delivered by *Planck* (in blue). Products in green are external, and products in orange are not being delivered in the current release. Each product delivered is accompanied by specific data characterizing it (not shown on the diagram). Note: the CIB analysis uses maps corrected for zodiacal emission beween 353-857 GHz - for simplicity this is not reflected in the diagram.

dominant source of confusion at high Galactic latitudes. At high frequencies, confusion from Galactic foregrounds dominates the noise budget at low Galactic latitudes, and the cosmic infrared background at high Galactic latitudes. The SNR has therefore been adapted for each particular case. More specifically, we use two detection thresholds at frequencies above 353 GHz: one in the brightest 52 % of the sky (a proxy for the Galactic sky, called Galactic zone), and a different one in the cleanest 48 % of the sky (a proxy for the extragalactic sky, called extragalactic zone). This strategy ensures interesting depth and good reliability in the extragalactic zone, but also high reliability in the Galactic zone. The actual thresholds used are listed in Table 7.

Because the sky properties vary so widely from low to high frequencies, the PCCS contains more than one estimate of the flux density of each source. The choice of the most accurate measure to use depends on frequency and foreground surface brightness as well as the solid angle subtended by the source: these choices are discussed in detail in Planck Collaboration XXVIII (2013).

The PCCS has been subject to *external* and *internal* validation:

1. At the three lowest (LFI) frequencies of *Planck* it is possible to validate most source identifications, completeness, reliability, positional accuracy and in some cases flux density accuracy using external data sets, particularly large-area radio surveys. This "external validation" was undertaken using the following catalogues and surveys: (1) full sky surveys and catalogues: the Early version of the *Planck* catalogue (ERCSC; Planck Collaboration XIV (2011)) and the NEWPS catalogue, based on *WMAP* results (Massardi et al. 2009); (2) in the southern hemisphere the AT20G survey at 20 GHz (Murphy et al. 2010); (3) in the northern hemisphere, where no large-area, high-frequency survey covering the frequency range of AT20G is available, we used CRATES (Healey et al. 2007). These catalogues have similar frequency coverage and source density as the PCCS.
2. The higher (HFI) frequency channels have been validated through an internal Monte-Carlo quality assessment (QA) process that uses large numbers of (artificial) source injection and detection loops to characterise the detection properties. The outcome of the detection code, for each channel, are statistical quantities describing the quality of detection, photometry and astrometry. The detection is described by the completeness and reliability of the catalogue. Completeness is a function of intrinsic flux density, the selection threshold applied to detection (SNR) and location. The reliability of

Table 7. PCCS characteristics.

Characteristic	Channel [GHz]								
	30	44	70	100	143	217	353	545	857
Frequency [GHz]	28.4	44.1	70.4	100.0	143.0	217.0	353.0	545.0	857.0
Wavelength [μm]	10561	6807	4260	3000	2098	1382	850	550	350
Beam FWHM [arcmin]	32.38	27.10	13.30	9.65	7.25	4.99	4.82	4.68	4.33
S/N threshold									
Full sky	4.0	4.0	4.0	4.6	4.7	4.8	...	...	...
Extragactic zone[b]	...	...	...	...	...	...	4.9	4.7	4.9
Galactic zone[b]	...	...	...	...	...	...	6.0	7.0	7.0
Number of sources									
Full sky	1256	731	939	3850	5675	16070	13613	16933	24381
$\|b\| > 30°$	572	258	332	845	1051	1901	1862	3738	7536
Flux densities									
Minimum[c] [mJy]	461	825	566	266	169	149	289	457	658
90 % completeness [mJy]	575	1047	776	300	190	180	330	570	680
Uncertainty [mJy]	109	198	149	61	38	35	69	118	166
Position uncertainty[d] [arcmin]	1.8	2.1	1.4	1.0	0.7	0.7	0.8	0.5	0.4

[a] FEBeCoP band averaged effective beam: $FWHM_{eff} = \sqrt{\frac{\Omega_{eff}}{2\pi} 8 \log 2}$, where Ω_{eff} is the FEBeCoP band averaged effective solid angle (see Planck Collaboration IV (2013) and Planck Collaboration VII (2013) for a full description of the *Planck* beams). This table shows the exact values that were adopted for the PCCS. When we constructed the PCCS, for the LFI channels we used a value of the effective FWHM that is slightly different (by $\ll 1$ %) from the final values specified in Planck Collaboration IV (2013) paper. A correction will be made in later versions of the catalogue.

[b] See text.

[c] Minimum flux density of the catalogue at $|b| > 30°$ after excluding the faintest 10 % of sources.

[d] Positional uncertainty derived by comparison with PACO sample up to 353 GHz and with Herschel samples in the other channels.

extragalactic sources is a function only of the detection SNR. The reliability of sources detected within cirrus clouds has been shown to relatively lower because of the higher probability to detect fluctuations of the structure of the diffuse interstellar medium rather than actual individual sources. The quality of photometry and astrometry is assessed through direct comparison of detected position and flux parameters. A comparison has also been performed with ACT (Gralla and members of the ACT team, in preparation), *Herschel*-SPIRE (Griffin et al. 2010), and with H-ATLAS (Eales et al. 2010), as discussed in Planck Collaboration XXVIII (2013).

Table 7 summarises the characteristics of the PCCS. The sources detected by *Planck* are dominated in number at low frequencies by radio galaxies (mainly through their synchrotron emission) and at high frequencies (i.e., above 217 GHz) by infrared galaxies (through the thermal emission of the dust), in agreement with previous findings based on the ERCSC (Planck Collaboration VII 2011; Planck Collaboration 2011; Planck Collaboration XIII 2011; Planck Collaboration Int. VII 2013). The large spectral range covered by LFI and HFI gives a unique view of the two populations and their relative weight as a function of frequency, e.g., through the evolution of the spectral indices (Planck Collaboration XXVIII 2013).

8.1.2. Cluster catalogue

Planck's all-sky coverage and broad frequency range are designed to detect the SZ signal of galaxy clusters across the sky. An early catalogue of *Planck* SZ-detected clusters was released in January 2011 (ESZ, Planck Collaboration VIII 2011). In 2013, *Planck* is releasing the largest ensemble of SZ selected sources detected from an all-sky survey (Planck Collaboration XXIX 2013) deeper and six times larger than the ESZ sample.

The *Planck* SZ catalogue of clusters and candidates includes 1227 sources detected from three adapted SZ-finder algorithms down to a signal-to-noise ratio of 4.5 distributed over 83.7 % of the sky (Table 8, Fig. 22). The statistically characterized catalogue of SZ detections was validated using external X-ray and optical/NIR data, and a multi-frequency follow-up programme for confirmation. A total of 861 SZ detections are associated with *bona fide* clusters, of which 178 are brand new *Planck*-discovered clusters. The remaining cluster candidates are divided into three classes according to their reliability, i.e., the quality of evidence that they are likely to be *bona fide* clusters. Only 142 of them are in the lowest reliability class.

The *Planck* SZ catalogue is and will be for years the deepest all-sky catalogue spanning the broadest cluster-mass range. The information derived from the validation of the *Planck* SZ detections and included in the released catalogue, in particular the SZ-based mass estimate, provides high value to the catalogue, and will make it a reference for studies of cluster physics. Considering that only a small fraction of the new *Planck* cluster candidates have been followed up with other observatories to date, it should also motivate multi-wavelength follow-up efforts.

Using an extended sub-sample of the *Planck* SZ clusters with high-quality XMM-Newton data, the scaling relation between SZ and X-ray properties was reassessed and updated, and we propose a new reference in this sense (Planck Collaboration XXIX 2013). With a better quality data and thus a higher precision, we show excellent agreement between SZ and X-ray measurements of the intra-cluster gas properties. The mean of

Table 8. Summary of the external validation and confirmation from follow-up observations. In each category, the figure represents the total number of *Planck* candidates identified exclusively with previously known X-ray, optical or SZ clusters. The category X-ray clusters covers identifications from the updated MCXC meta-catalogue. The category optical clusters covers identification from the Abell, Zwicky, and SDSS-based catalogues only. The category SZ clusters covers identification from SPT and ACT catalogues only. Confirmations from follow-up do not cover the observations performed by the *Planck* collaboration to measure the missing redshifts of known clusters. Confirmation from archival data covers X-ray data from Chandra, *XMM*, and ROSAT PSPC pointed observations only.

Category	N	n		Source
Previously known	**683**			
from:		472	X-ray:	MCXC meta-catalogue
		182	Optical:	Abell, Zwicky, SDSS
		16	SZ:	SPT, ACT
		13	Misc:	NED & SIMBAD
New confirmed	**178**			XMM, ENO, WFI, NTT, AMI, SDSS
New candidate	**366**			
reliability:		54	High	
		170	Medium	
		142	Low	
Total *Planck* SZ catalogue	**1227**			

Y_{500} to Y_X is very well constrained with a precision of 2.5 %, $\log(Y_{SZ}/Y_X) = -0.027 \pm 0.010$.

To date, a total of 813 *Planck* clusters have measured redshifts, ranging from $z = 0.01$ to ∼1 with two thirds of the clusters lying below $z = 0.3$. For all the *Planck* clusters with redshifts, we have used the Compton Y measure to estimate masses, which range between ∼0.1 and $1.6 \times 10^{15}\,M_\odot$.

Except at low redshifts, the *Planck* cluster distribution exhibits a nearly redshift-independent mass limit. Owing to this nearly mass-limited selection function and to its all-sky nature, *Planck* detects new clusters in a region of the mass-redshift plane that is sparsely populated by the RASS catalogues (e.g., Böhringer et al. 2000, 2004; Burenin et al. 2007; Ebeling et al. 2007). Furthermore, *Planck* has the unique capability of detecting the most massive clusters, $M \geq 5 \times 10^{14}\,M_\odot$, at high redshifts, $z \geq 0.5$, in the exponential tail of the cluster mass function, which are the best clusters for cosmological studies.

The *Planck* catalogue of SZ sources serves to define samples for cosmological studies. A first step in this direction consists of the selection of a sub-sample consisting of 189 clusters detected above a signal-to-noise ratio of 7 and with measured redshifts (see Sect. 9.7), which have been used to constrain the cosmological parameters (Planck Collaboration XXI 2013).

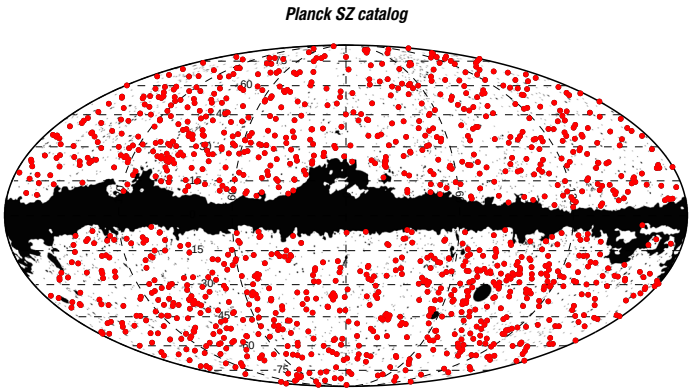

Fig. 22. Distribution of the 1227 *Planck* clusters and candidates across the sky (red thick dots). The masked point-sources (black thin dots), the Magellanic clouds (large black areas) and the Galactic mask used by the detection algorithms to detect SZ sources are also shown.

8.2. Diffuse emission

In this Section we describe briefly the extraction of some of the extended emission components from the *Planck* maps using optimized techniques which in some cases exploit the availability of external information (e.g., ancillary maps tracing specific astrophysical components, or prior knowledge of the spectral energy distribution or of the power spectrum), to yield astrophysically meaningful foregrounds.

In intensity, seven types of diffuse foregrounds have been identified that must be removed or controlled for CMB analysis: dust thermal emission, dust anomalous emission (rotation of small grains), three CO rotational lines, free-free, synchrotron, CIB not fully correlated between frequencies, the two diffuse Sunyaev-Zeldovich secondary CMB distortions, and the background of unresolved radio sources.

8.2.1. Thermal emission from Galactic dust

The CMB fades toward higher frequencies, whereas the thermal dust emission spectrum increases, and so dust becomes the dominant signal in the submillimetre. The HFI instrument on *Planck* has multifrequency sensitivity in the "dust channels" covering the spectral range where this transition occurs up to 857 GHz for which the angular resolution is highest (Table 2). Dust emission is seen extending to high Galactic latitude, the wispy "cirrus" represented in bluish tones in Fig. 1.

Understanding both the frequency dependence and spatial fluctuations of the (polarized) intensity from thermal dust is important in refining the separation of this foreground contamination of the CMB, and as an all-sky measure of column density. This has motivated the development of a model, which quantifies the foreground component in the *Planck* maps arising from thermal dust emission from the Galaxy. This *Planck* dust model is described in detail in Planck Collaboration (2013) and the data processing pipeline is outlined in Fig. 21. The use of a range of available ancillary data distinguishes this model

from the dust component extracted using component separation techniques and frequencies below 353 GHz, described in the Sect. 8.2.3.

The *Planck* dust model is based on the intensity maps for the three highest *Planck* bands, 353, 545, and 857 GHz, and *IRAS* 100 μm (3000 GHz, from the *IRIS* product, Miville-Deschênes & Lagache 2005). As described in Planck Collaboration VI (2013), the zero level of these maps can be set such that there is no dust emission where there is no atomic HI gas column density (according to the LAB survey Kalberla et al. (2005)). Determination of T_d is made possible by the multi-frequency coverage, through fitting the greybody spectral energy distribution (SED) of I_ν.

The brightness I_ν for optically-thin thermal dust emission is given by $I_\nu = \tau_\nu B_\nu(T_d)$, where τ_ν is the dust optical depth of the column of material and $B_\nu(T_d)$ is the Planck function for dust temperature T_d. In the *Planck* dust model there are three parameters, T, τ_{353} at 353 GHz, and β, the exponent of the assumed power-law frequency dependence of τ_ν. A conversion of τ_{353} to $E_{\rm B-V}$ has been obtained by correlating the submillimetre optical depth with SDSS reddening measurements of quasars, a very similar approach to the one adopted by Schlegel et al. (1998).

All-sky maps of T_d and τ from *Planck* were first presented by Planck Collaboration XIX (2011) using a fixed β. In the new *Planck* dust model (Planck Collaboration 2013), the maps of T_d and τ_{353} are at 5′ resolution while β is estimated at 35′. This provides a much more detailed description of the thermal dust emission than the Finkbeiner et al. (1999) model, which assumed constant β and used a T_d map with an angular resolution of several degrees.

The high resolution of the *Planck* product is a major improvement which results in a much more detailed mapping of column density structure, especially in denser regions of the ISM where the equilibrium temperature of big dust grains changes on small angular scales due to attenuation of the radiation field and also, it appears, to changes in the intrinsic dust opacity (and its ability to emit). Because of the increase in sensitivity, a better control of systematic effects, and the combination of four intensity maps at 5′ resolution spanning the peak of the SED and into the Rayleigh-Jeans region, the new *Planck* $E_{\rm B-V}$ product also provides a more precise estimate of the dust column density even in the diffuse ISM where T_d is not varying as strongly on small scales.

8.2.2. CO extraction

Rotational line emission from carbon monoxide (CO) in the Galactic interstellar medium is present in all of the HFI bands except at 143 GHz, most significantly at 100, 217, and 353 GHz (due to the CO J=1→0, J=2→1, and J=3→2 rotational CO transitions at ∼115, 230, and 345 GHz respectively). CO emission arises from the denser parts of the interstellar medium, and is concentrated at low and intermediate Galactic latitudes. Considering that the part of the sky used for estimation of cosmological parameters is a large fraction of the high Galactic latitude (<60 %), and that the CO emission intensity is only significant in a small fraction(< 1 %) of the high-latitude sky, it is better for CMB likelihood-based analysis to mask these regions rather than to correct the whole map for CO. However, if one wishes to obtain a clean CMB map over a significantly larger fraction of the sky (for e.g., non-Gaussianity analysis), the HFI maps need to be corrected for this emission.

Three approaches to estimate the CO emission have been evaluated and are described in Planck Collaboration XIII (2013).

- One of these techniques (so-called TYPE 1) relies on the fact that each bolometer has a different responsivity to CO largely due to their specific passband shapes. The transmission at the frequency of each CO transition has been accurately measured on the ground, and can also be estimated by comparison to surveys made with dedicated observatories. Knowledge of the relative bolometer spectral responses allows us to extract all-sky maps of each CO line independently of the others and of any ancillary data. This method yields CO line emission maps that have relatively low SNR bacause they are extracted from single-bolometer data. The benefit, however, is that these maps do not suffer from contamination from other HFI channels and are thus useful to obtain unbiased CO-free frequency maps.
- the so-called TYPE 2 maps are obtained using a multi-frequency component separation approach. Three frequency channel maps are combined to extract independently the J=1→0 (100, 143 and 353 GHz channels) and J=2→1 (143, 217 and 353 GHz channels) CO maps from the average transmission in each channel. Because channels are combined, the spectral behaviour of other foregrounds (free-free and dust) are needed as extra constraints to allow as clean a CO extraction as possible. The TYPE 2 CO maps produced in this way have a higher SNR than Type-1 maps at the cost of residual contamination from other diffuse foregrounds. These maps constitute a unique product for astrophysics that provides the possibility to get the excitation ratio for all parts of the sky where the CO intensity is strong enough.
- The a-priori specification of the J=2→1/J=1→0 and J=3→2/J=2→1 line ratios yields a map of combined CO emission (aka as TYPE 3) that has very high SNR, and can be used as a sensitive finder chart for low-intensity diffuse CO emission over the whole sky. This map is extracted using the full Commander-Ruler component separation pipeline (see Sect. 8.2.3). The line ratios can be determined from ground-based observations, or from a first iteration of the component separation algorithm with simplified assumptions; the latter is the route used by *Planck*.

All three types of CO maps have been extensively compared and cross-checked internally.

8.2.3. Astrophysical foregrounds from component separation

The wide frequency range of *Planck* allows us to use component separation techniques based on *Planck* data only to derive tight constraints on several astrophysical components in addition to the primary CMB fluctuations. Specifically, in Planck Collaboration XII (2013) we present individual maps of: 1) a combined high-frequency component accounting for Galactic thermal dust emission and the integrated thermal dust emission of the CIB; 2) Galactic carbon monoxide (CO TYPE 3, see 8.2.2); and 3) a combined low-frequency component accounting for synchrotron, free-free, and anomalous microwave emission (AME, almost certainly emission from microscopic spinning dust grains; Fig. 23). Only *Planck* frequencies between 30 and 353 GHz are included, as the systematics of 545 and 857 GHz are less well understood than those of the lower ones, and the dust signal is already strongly dominant at 353 GHz.

The astrophysical components are derived by a standard Bayesian parameter estimation approach, in which an explicit parametric model is fitted to the raw observations within the bounds of physically motivated priors. This process is implemented in two stages. In the first, the frequency maps are

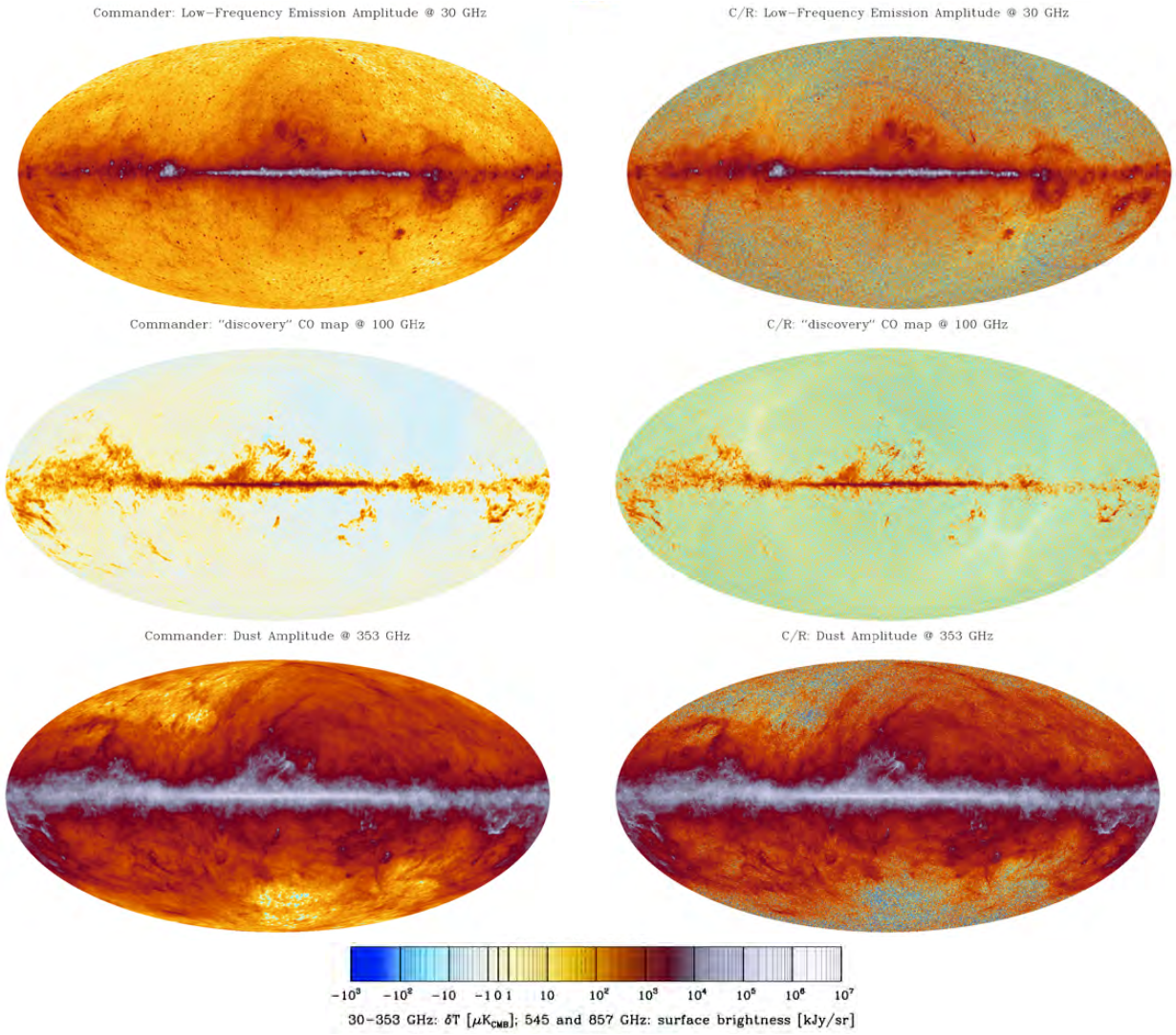

Fig. 23. Some of the foreground maps produced by Commander (on the left, resolution ∼1 degree) and by Commander-Ruler (on the right, resolution ∼7 arcminutes). At the top, a map of the amplitude of low-frequency foregrounds at 30 GHz (which include synchrotron, free-free, and anomalous emission). In the middle, a map of the integrated intensity of CO TYPE 3. In the bottom panel, a map of the amplitude of high-frequency foregrounds at 353 GHz (dust thermal emission and the cosmic infrared background).

smoothed to a common resolution of 40′ FWHM, pixelized at $N_{\rm side} = 256$), and all model parameters (signal amplitudes and spectral parameters) are fitted jointly by the CMB Gibbs sampler Commander. The CMB samples produced by this code form the basis of the low-ℓ *Planck* CMB temperature likelihood, as described in (Planck Collaboration XV 2013). In the second stage, the spectral parameters from the low-resolution fit are formally upgraded to $N_{\rm side} = 2048$, and full-resolution CMB and thermal dust amplitudes are estimated using a generalized least-squares fit (see Planck Collaboration XII (2013) for details.). The low-resolution foreground components are limited by the angular resolution of the lowest frequencies, and the products from the low-resolution stage are therefore retained for these.

The thermal dust emission is modelled as a one-component gray-body with a free emissivity, $\beta_{\rm dust}$, and dust temperature, $T_{\rm d}$, per pixel. Since we only include frequencies up to 353 GHz here, the dust temperature is largely unconstrained in our fits, and we therefore adopt a tight prior around the commonly accepted mean value of $T_{\rm d} = 18 \pm 0.05$ K. The only reason it is not fixed completely at 18 K is to allow for modelling errors near the Galactic center. The dust emissivity prior is set to $\beta_{\rm d} = 1.5 \pm 0.3$, where the mean is once again set by a dedicated MCMC run. Because the CIB is a statistically isotropic signal, it can be well-approximated by a dominant monopole plus a small spatially varying fluctuation, analogous to the CMB itself. Further, as shown by Planck Collaboration CIB In preparation, the CIB frequency spectrum follows very nearly a one-component gray-body function with similar parameters to those of the Galactic thermal dust component. The current model therefore accounts for the CIB component without introducing an additional and dedicated CIB parameter, simply by first subtracting off a best-fit monopole at each frequency, and, second, through the free dust parameters (amplitude and spectral parameters) for each pixel. The dust amplitude map shown in Fig. 23 therefore contains both Galactic thermal dust and extragalactic CIB fluctuations. The CIB fluctuations are strongly sub-dominant everywhere on the sky except in the very cleanest regions.

The CO component is modelled in terms of a mean amplitude per pixel at 100 GHz, which is then extrapolated to 217 and 353 GHz through a spatially constant overall factor per frequency called a "line ratio." To minimize parameter degeneracies, the default line ratios are estimated in a dedicated prelim-

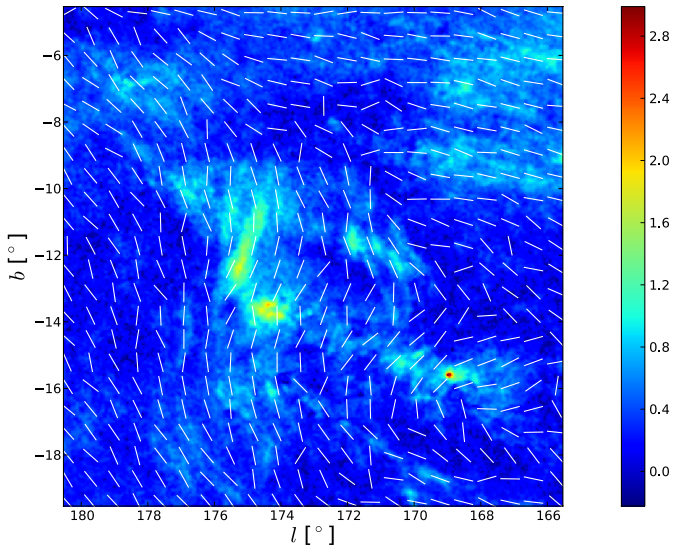

Fig. 24. Polarised intensity at 353 GHz (in mK_{CMB}) and polarization orientation indicated as segments of uniform length, in the Taurus region.

inary run using only the pixels with the highest CO-to-thermal-dust ratio (0.5 % of the sky), and holding the dust and synchrotron spectral indices spatially constant. This fit results in line ratios of 0.60 at 217 GHz and 0.30 at 353 GHz, in excellent agreement with those derived from the "Type-2" analysis described in Planck Collaboration XIII (2013). The TYPE 3 CO map maximizes the signal-to-noise ratio, and it can be seen as a discovery map for new potential CO clouds; however; it combines the information about the single line transition into a total intensity one.

The low-frequency component is modelled as a straight power-law in intensity units, with a free spectral index per pixel. We adopt a prior of $\beta = -3 \pm 0.3$ for the low-frequency spectral index; this is mostly relevant only at high Galactic latitudes where the signal-to-noise ratio is low and the dominant foreground component is expected to be synchrotron emission. In the signal-dominated AME and free-free regions at low latitudes, the data are sufficiently strong that the prior becomes irrelevant.

In addition, we require all (low-resolution) foreground amplitudes to be positive; computational cost prohibits us from imposing the same constraint at high resolution. Fig. 23 shows the resulting component maps.

In the 2013 data release, we adopt the posterior mean as our signal estimate, and the posterior RMS as the corresponding uncertainty. Mean and RMS maps are provided for each signal component and for each per-pixel spectral parameter. Two caveats are in order regarding use of these products for further scientific analysis. First, significant systematic uncertainties are associated with several of these estimates. One example is the correlated HFI noise, which is clearly seen in the thermal dust emissivity map; the products presented here do not take into account spatially correlated noise. Second, the full posterior is significantly non-Gaussian due to the presence of non-Gaussian spectral parameters and the positivity amplitude prior, as well as strongly correlated between components. The mean and RMS maps provided in this data release should therefore be understood as a convenient representation of the full posterior, rather than a precise description of each component; if very high statistical precision is required, one should resort to the original ensemble of individual Monte Carlo samples.

8.2.4. *Planck* observations of dust polarization

The *Planck* satellite will produce the first all-sky map of dust polarization in emission. The current level of data analysis is already revealing a new sky that we have just started to explore. At 353 GHz, the observations have the sensitivity to image dust polarization over the whole sky. The maps of Stokes parameters I, Q & U provide the data needed to characterize the structure of the Galactic magnetic field and its coupling with interstellar matter as well as turbulence in the diffuse interstellar medium (ISM). With an angular resolution of 5′, the maps also reveal the magnetic field structure in molecular clouds and star forming regions. The data analysis is intertwined with the characterization of the polarization properties of dust. From the perspective of dust phsysics, we seek to understand which grains contribute to the observed polarization, where in the ISM they are aligned with the Galactic magnetic field, and with what efficiency.

While the state of understanding of *Planck*'s polarization data is still not adequate for analysis of CMB polarization (Sect.9.3), it is advancing fast for the much brighter polarized foregrounds at 353 GHz. A first set of *Planck* Galactic polarization papers will be published shortly after this 2013 release. These papers will report results based on the study of the degree of dust polarization (P/I) over the whole sky, and first comparisons with maps of synchrotron polarization and Faraday rotation. One highlight that arises readily out of these maps is the unexpectedly high degree of polarization of the dust emission from the diffuse interstellar medium, in many locations reaching $P/I > 15$ % at 353 GHz. These studies will also address the statistics of P/I and ϕ for selected field towards nearby molecular clouds (see, e.g., Fig. 24), especially in relation with MHD simulations; the spectral dependence of the polarized emission; the comparison of the degree of polarization in the submm range with the optical (from stellar observations); and the characterization of its angular structure and spectral dependence, aiming at component separation for CMB studies.

8.2.5. All-sky Sunyaev-Zeldovich emission

Using the *Planck* frequency maps from 100 to 857 GHz and specially tailored component separation methods we have constructed an all-sky map of the Compton parameter, y, estimated from the thermal Sunyaev-Zeldovich (tSZ) effect (Sunyaev & Zeldovich 1972), and constructed its angular power spectrum (Planck Collaboration XXI 2013).

We estimated instrumental noise uncertainties and foreground contamination. We find that diffuse thermal dust emission is the major foreground contaminant at low multipoles ($\ell < 30$), whereas at high multipoles ($\ell > 500$) the clustered CIB, together with radio and IR point sources dominate. These foreground contributions are significantly reduced by computing the cross-power spectrum from two y-maps obtained with the adapted component separation methods.

A further subtraction of the residual foreground spectra results in the first estimate of a clean tSZ power spectrum spanning a wide range of multipoles from $\ell = 30$ to $\ell = 1000$. The measured tSZ spectrum is composed of the total signal from resolved clusters in the *Planck* catalogue of SZ sources and of the contribution from unresolved clusters of galaxies and hot diffuse gas (Sect. 9.7).

9. *Planck* 2013 cosmology results

9.1. Parameter estimation, lensing, and inflation

Since their discovery, anisotropies in the CMB have contributed significantly to defining our cosmological model and measuring its key parameters. The standard model of cosmology is based upon a spatially flat, expanding Universe whose dynamics are governed by General Relativity and dominated by cold dark matter and a cosmological constant (Λ). The seeds of structure have Gaussian statistics and form an almost scale-invariant spectrum of adiabatic fluctuations.

Planck's measurements of the cosmological parameters derived from the nominal mission are presented and discussed in Planck Collaboration XVI (2013). The most important conclusion from this paper is the excellent agreement between the *Planck* temperature spectrum at high ℓ and the predictions of the ΛCDM model. All of our current observations can be fit remarkably well by a six parameter ΛCDM model and we provide strong constraints on deviations from this model. The best-fit cosmological parameters are not affected by foreground modeling uncertainties and the best-fit model provides an excellent fit to the spectra from *Planck*, ACT and SPT (see Fig. 25). The ACT and SPT bandpowers plotted are from Calabrese et al. (2013).

In some cases we find significant changes compared to previous CMB experiments, as discussed in detail in Planck Collaboration XVI (2013). In particular, when we compare models based on CMB data only we find that the *Planck* best-fit model retrieves lower Ω_Λ (by $\sim$6 %), higher $\Omega_{baryons}$ (by $\sim$9 %), and higher Ω_{CDM} (by $\sim$18 %) than the corresponding WMAP9[12] model. However, when adding BAO to both sets of data, the gap reduces by a factor of $\sim$3 in all three components.

Among the constraints that we are able to determine, several are notable. The angular size of the acoustic scale is determined to better than 0.1 %, as $\theta_\star = (1.19355 \pm 0.00078)^\circ$, which leads to a 0.3 % constraint in the $\Omega_\mathrm{m} - h - \Omega_\mathrm{b}h^2$ subspace for ΛCDM models (all confidence intervals are 68 %; Planck Collaboration XVI 2013). For ΛCDM the matter and baryon densities are well determined, with the latter being consistent with recent results from big-bang nucleosynthesis. We find excellent consistency with BBN even in extensions to the six-parameter model. The predictions of the baryon density from these two methods involve all of the known forces of nature and this highly non-trivial consistency provides strong evidence for the universality of those laws.

Lensing of the CMB enters the *Planck* parameter estimation results discussed in Planck Collaboration XVI (2013) in two ways. First, the power spectrum of the temperature anisotropies is modified at the few percent level by lensing, with the primary effect being a smoothing of the acoustic peaks on angular scales relevant for *Planck*. We detect this smoothing effect at $10\,\sigma$. We include this effect in our parameter constraints. Second, the measurements of the power spectrum of the reconstructed gravitational lensing potential, described in Planck Collaboration XVII (2013) and Sect. 7.2, can be combined with the main *Planck* likelihood developed in Planck Collaboration XV (2013) (see also Sect. 7.3). The lensing power spectrum measurements condense the cosmological signal contained in the non-Gaussian 4-point function of the CMB anisotropies in a near-optimal way. Combining the lensing likelihood with the main *Planck* likelihood is therefore equivalent to a joint analysis of the anisotropy power spectrum and that part of the 4-point function due to lensing.

The expected lensing power spectrum is tightly constrained in the six-parameter ΛCDM model by the *Planck* temperature power spectrum and the *WMAP* low-ℓ polarization data. The best-fitting model predicts a lensing power spectrum in good agreement with the *Planck* lensing reconstruction measurement, further validating the predictions of the ΛCDM model, calibrated on the CMB fluctuations at $z \approx 1100$. These predictions include clustering and the evolution of the geometry at low redshift. We express the amplitude of the lensing power spectrum in terms of a phenomenological power spectrum amplitude parameter, $A_\mathrm{L}^{\phi\phi}$, which scales the theoretical 4-point function (due to lensing) at each point in parameter space. From *Planck*'s best-fit model, the expected value of this scaling parameter is 1.0; for the nominal mission we find $A_\mathrm{L}^{\phi\phi} = 0.99 \pm 0.05$ (68 % CL; Planck Collaboration XVI 2013). The constraint is consistent with the expected value of unity, and represents a 20σ detection of lensing in the context of the ΛCDM model.

Without the low-ℓ polarization data, and in the absence of lensing, the amplitude of the primordial power spectrum, A_s, and the optical depth to reionization, τ, would be degenerate with only the combination $A_\mathrm{s}e^{-2\tau}$ being well determined by the (unlensed) temperature power spectrum. However, lensing partially breaks this degeneracy since the lensing power spectrum is independent of the optical depth. Combining the temperature power spectrum with the lensing likelihood, we determine $\tau = 0.089 \pm 0.032$ (68 % CL) *from the temperature anisotropies alone*. This constraint is consistent, though weaker, than that from *WMAP* polarization (Hinshaw et al. 2012b). Importantly, the lensing route does not depend on the challenging issue of removing large-scale polarized emission from our Galaxy that is critical for the *WMAP* measurement. At 95 % confidence, we can place a lower limit on the optical depth $\tau < 0.04$, which exceeds the value for instantaneous reionization at $z = 6$, further supporting the picture that reionization is an extended process.

Beyond the six-parameter ΛCDM model, the *Planck* lensing measurements strengthen the evidence reported by ACT (Sievers et al. 2013) and SPT (van Engelen et al. 2012; Story et al. 2012) for dark energy from the CMB alone in models with spatial curvature. Closed models with low energy density in dark energy can be found that produce unlensed CMB power spectra nearly identical to the best-fitting ΛCDM model. This "geometric" degeneracy is partially broken by lensing, since the closed models predict too much lensing power. Even without using the *Planck* lensing reconstruction, the 10σ detection of the smoothing of the temperature power spectrum allows *Planck*, used in combination with ACT and SPT at high-ℓ (to constrain better extra-Galactic foregrounds) and *WMAP* large scale polarization, to break the geometrical degeneracy and provides evidence for dark energy *purely from the CMB* (Planck Collaboration XVII 2013). Adding the lensing likelihood, we constrain any departures from spatial flatness at the percent level: $\Omega_K = -0.0096^{+0.010}_{-0.0082}$ (68 % CL) for the same data combination, improving earlier CMB-only constraints (Story et al. 2012) by around a factor of two, and setting our determination of dark energy from temperature anisotropies data alone to $\Omega_\Lambda = 0.67^{+0.027}_{-0.023}$ (68 % CL). Tighter constraints from the combination of *Planck* and other astrophysical data are given in Planck Collaboration XVI (2013).

Within the minimal, six-parameter model the expansion rate is well determined, independent of the distance ladder. One of the most striking results of the nominal mission is that the best-fit Hubble constant $H_0 = (67 \pm 1.2)$ km s^{-1} Mpc^{-1}, is lower

[12] We compare the model [*Planck* +WP+highL] of Table 5 in Planck Collaboration XVI (2013) with [WMAP+eCMB] of Table 4 of Hinshaw et al. (2012a).

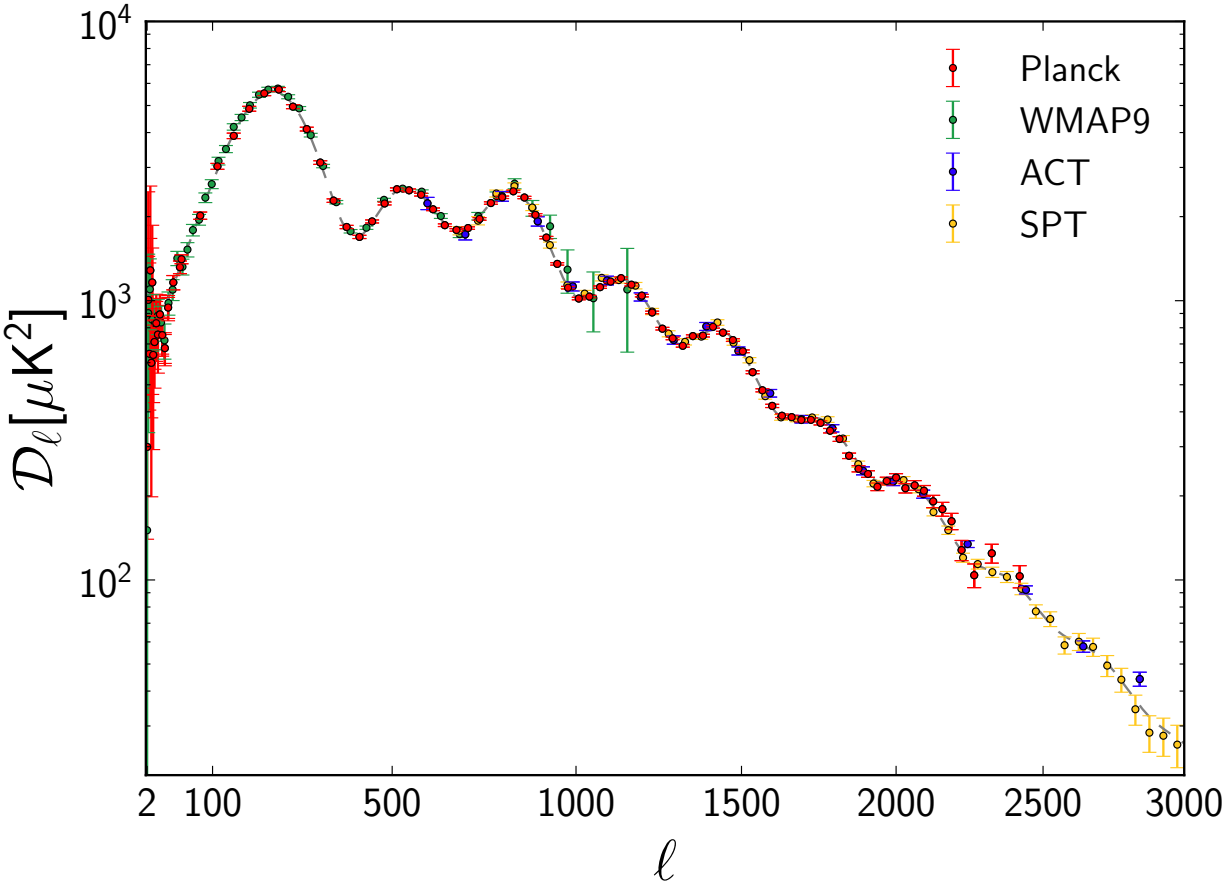

Fig. 25. Measured angular power spectra of *Planck*, WMAP9, ACT, and SPT. The model plotted is *Planck*'s best-fit model including *Planck* temperature, WMAP polarization, ACT, and SPT (the model is labelled [Planck+WP+HighL] in Planck Collaboration XVI (2013)). Error bars include cosmic variance. The horizontal axis is $\ell^{0.8}$.

than that measured using traditional techniques, though in agreement with that determined by other CMB experiments (e.g., most notably from the recent WMAP9 analysis where Hinshaw et al. 2012c find $H_0 = (69.7 \pm 2.4)$ km s^{-1} Mpc^{-1} consistent with the *Planck* value to within $\sim 1\,\sigma$). Freedman et al. (2012), as part of the *Carnegie Hubble Program*, use Spitzer Space Telescope mid-infrared observations to recalibrate secondary distance methods used in the HST Key Project. These authors find $H_0 = (74.3 \pm 1.5 \pm 2.1)$ km s^{-1} Mpc^{-1} where the first error is statistical and the second systematic. A parallel effort by Riess et al. (2011) used the Hubble Space Telescope observations of Cepheid variables in the host galaxies of eight SNe Ia to calibrate the supernova magnitude-redshift relation. Their 'best estimate' of the Hubble constant, from fitting the calibrated SNe magnitude-redshift relation is, $H_0 = (73.8 \pm 2.4)$ km s^{-1} Mpc^{-1} where the error is $1\,\sigma$ and includes known sources of systematic errors. At face value, these measurements are discrepant with the current *Planck* estimate at about the $2.5\,\sigma$ level. This discrepancy is discussed further in Planck Collaboration XVI (2013).

Extending the Hubble diagram to higher redshifts we note that the best-fit ΛCDM model provides strong predictions for the distance scale. This prediction can be compared to the measurements provided by studies of Type Ia SNe and baryon acoustic oscillations (BAO). Driven in large part by our preference for a higher matter density we find mild tension with the (relative) distance scale inferred from compilations of SNe (Conley et al. 2011; Suzuki et al. 2012). In contrast our results are in excellent agreement with the BAO distance scale compiled in Anderson et al. (2012).

The *Planck* data, in combination with polarization measured by *WMAP*, high-ℓ anisotropies from ACT and SPT and other, lower redshift data sets, provides strong constraints on deviations from the minimal model. The low redshift measurements provided by the BAO allow us to break some degeneracies still present in the *Planck* data and significantly tighten constraints on cosmological parameters in these model extensions. The ACT and SPT data help to fix our foreground model at high ℓ. The combination of these experiments provides our best constraints on the standard 6-parameter model; values of some key parameters in this model are summarized in Table 9.

From an analysis of an extensive grid of models, we find no strong evidence to favour any extension to the base ΛCDM cosmology, either from the CMB temperature power spectrum alone or in combination with *Planck* lensing power spectrum and other astrophysical datasets. For the wide range of extensions which we have considered, the posteriors for extra parameters generally overlap the fiducial model within $1\,\sigma$. The measured values of the ΛCDM parameters are relatively robust to the inclusion of different parameters, though a few do broaden significantly if additional degeneracies are introduced. When the *Planck* likelihood does provide marginal evidence for extensions to the base ΛCDM model, this comes predominantly from a deficit of power (compared to the base model) in the data at $\ell < 30$.

The primordial power spectrum is well described by a power-law over three decades in wave number, with no evidence

Table 9. Cosmological parameter values for the *Planck*-only best-fit 6-parameter ΛCDM model (*Planck* temperature data plus lensing) and for the *Planck* best-fit cosmology including external data sets (*Planck* temperature data, lensing, *WMAP* polarization [WP] at low multipoles, high-ℓ experiments, and BAO, labelled [Planck+WP+highL+BAO] in Planck Collaboration XVI (2013)). Definitions and units for all parameters can be found in Planck Collaboration XVI (2013).

	Planck (CMB+lensing)		*Planck*+WP+highL+BAO	
Parameter	Best fit	68 % limits	Best fit	68 % limits
$\Omega_b h^2$	0.022242	0.02217 ± 0.00033	0.022161	0.02214 ± 0.00024
$\Omega_c h^2$	0.11805	0.1186 ± 0.0031	0.11889	0.1187 ± 0.0017
$100\theta_{MC}$	1.04150	1.04141 ± 0.00067	1.04148	1.04147 ± 0.00056
τ	0.0949	0.089 ± 0.032	0.0952	0.092 ± 0.013
n_s	0.9675	0.9635 ± 0.0094	0.9611	0.9608 ± 0.0054
$\ln(10^{10} A_s)$	3.098	3.085 ± 0.057	3.0973	3.091 ± 0.025
Ω_Λ	0.6964	0.693 ± 0.019	0.6914	0.692 ± 0.010
σ_8	0.8285	0.823 ± 0.018	0.8288	0.826 ± 0.012
z_{re}	11.45	$10.8^{+3.1}_{-2.5}$	11.52	11.3 ± 1.1
H_0	68.14	67.9 ± 1.5	67.77	67.80 ± 0.77
Age/Gyr	13.784	13.796 ± 0.058	13.7965	13.798 ± 0.037
$100\theta_*$	1.04164	1.04156 ± 0.00066	1.04163	1.04162 ± 0.00056
r_{drag}	147.74	147.70 ± 0.63	147.611	147.68 ± 0.45
$r_{drag}/D_V(0.57)$	0.07207	0.0719 ± 0.0011		

for "running" of the spectral index. The spectrum does, however, deviate significantly ($6\,\sigma$) from scale invariance, as predicted by most models of inflation (see below). The unique contribution of *Planck*, compared to previous experiments, is that the departure from scale invariance is robust to changes in the underlying theoretical model.

We find no evidence for extra relativistic species, beyond the three species of (almost) massless neutrinos and photons. The main effect of massive neutrinos is a suppression of clustering on scales larger than the horizon size at the non-relativisitic transition. This affects both $C_L^{\phi\phi}$ with a damping for $L > 10$, and C_ℓ^{TT} reducing the lensing induced smoothing of the acoustic peaks. Using *Planck* data in combination with polarization measured by *WMAP* and high-ℓ anisotropies from ACT and SPT allows for a constraint of $\sum m_\nu < 0.66\,\mathrm{eV}$ (95 % CL) based on the [*Planck*+WP+highL] model. Curiously, this constraint is weakened by the addition of the lensing likelihood $\sum m_\nu < 0.85\,\mathrm{eV}$ (95 % CL), reflecting mild tensions between the measured lensing and temperature power spectra, with the former preferring larger neutrino masses than the latter. Possible origins of this tension are explored further in Planck Collaboration XVI (2013) and are thought to involve both the $C_L^{\phi\phi}$ measurements and features in the measured C_ℓ^{TT} on large scales ($\ell < 40$) and small scales $\ell > 2000$ that are not fit well by the ΛCDM+foreground model. The signal-to-noise on the lensing measurement will improve with the full mission data, including polarization, and it will be interesting to see how this story develops.

The combination of large lever arm, sensitivity to isocurvature fluctuations and non-Gaussianity makes *Planck* particularly powerful at probing inflation. Constraints on inflationary models are presented in Planck Collaboration XXII (2013) and overwhelmingly favor a single, weakly coupled, neutral scalar field driving the accelerated expansion and generating curvature perturbations. The models that fit best have a canonical kinetic term and a field slowly rolling down a featureless potential.

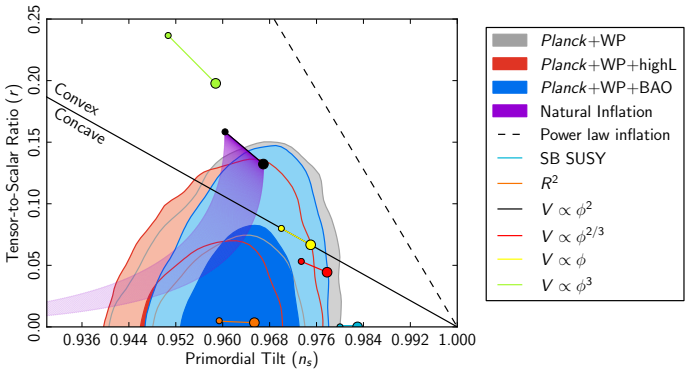

Fig. 26. Marginalized 68 % and 95 % confidence levels for n_s and r from Planck+WP and BAO data, compared to the theoretical predictions of selected inflationary models.

Of the models considered, those with locally concave potentials are favored and occupy most of the region in the ns,r plane allowed at 95 % confidence level (see Fig. 23). Power law inflation, hybrid models driven by a quadratic term and monomial large field potentials with a power larger than two lie outside the 95 % confidence contours. The quadratic large field model, in the past often cited as the simplest inflationary model, is now at the boundary of the 95 % confidence contours of Planck + WP + CMB high ℓ data.

The axion and curvaton scenarios, in which the CDM isocurvature mode is uncorrelated or fully correlated with the adiabatic mode, respectively, are not favored by *Planck*, which constrains the contribution of the isocurvature mode to the primordial spectra at $k = 0.05\mathrm{Mpc}^{-1}$ to be less than 3.9 % and 0.25 % (at 95 % CL), respectively.

The *Planck* results come close to the tightest upper limit on the tensor-to-scalar amplitude possible from temperature data alone. The precise determination of the higher acoustic peaks breaks degeneracies that have weakened earlier measurements.

The bound ($r < 0.11$ at 95 %CL) implies an upper limit for the energy scale of standard inflation of 1.9×10^{16} GeV (95 %CL).

The power spectrum of the best fit base ΛCDM cosmology has a higher amplitude than the observed power spectrum at multipoles $\ell < 30$. The low-ℓ difference is in turn related to the preference for a higher lensing amplitude when fitting to the temperature anisotropy power spectrum through a chain of parameter degeneracies (see Planck Collaboration XVI 2013, for discussion). There are other indications for 'anomalies' at low ℓ (Section 9.2, Planck Collaboration XXIII (2013)), which may be indicative of new physics operating on the largest scales. However the interpretation of such anomalies is difficult in the absence of a compelling theoretical framework. In addition, our determination of the power spectrum amplitude is in weak tension with that derived from the abundance of rich clusters found with the Sunyaev-Zeldovich effect in the *Planck* data (Planck Collaboration XX 2013) and from measurements of cosmic shear from the CFHTLenS survey (Heymans et al. 2012; Erben et al. 2012).

9.2. Non-Gaussianity

Two of the fundamental assumptions of the standard cosmological model — that the initial fluctuations are statistically isotropic and Gaussian in nature — have been rigorously examined in the four CMB maps described in Section 7.1 (Planck Collaboration XXIII 2013)). Realistic simulations incorporating essential aspects of the *Planck* measurement process have been used to support the analysis. Deviations from isotropy have been found in the data, which are robust against changes in the component separation algorithm or mask used, or frequency examined. Many of these anomalies were previously observed in the *WMAP* data on large angular scales (e.g., an alignment between the quadrupole and octopole moments, an asymmetry of power between two preferred hemispheres, and a region of significant decrement, the so-called Cold Spot), and are now confirmed at similar levels of significance ($\sim 3\sigma$) but a higher level of confidence. In spite of the presence of strong non-Gaussian or anisotropic emissions coming from Galactic and extragalactic sources, the consistency of the tests performed on the four CMB maps produced by the component separation algorithms strongly favors a cosmological origin for the anomalies. Moreover, the agreement between *WMAP* and the two independent instruments of *Planck* rules out a possible explanation based on systematic artifacts.

On the other hand, we find little evidence for non-Gaussianity (see also Planck Collaboration XXIV (2013)), with the exception of a few statistical signatures that seem to be associated with specific anomalies. In particular, we find that the quadrupole-octopole alignment is also connected to a low observed variance of the CMB signal with respect to the standard ΛCDM model. In addition, the hemispherical asymmetry is now found to persist to much smaller angular scales, and can be described in the low-ℓ regime at a statistically significant level by a phenomenological dipole modulation model. It is plausible that some of these features may be reflected in the angular power spectrum of the data, which shows a deficit of power on these scales. Indeed, when the two opposing hemispheres defined by the preferred direction are considered separately, the power spectrum shows a clear power asymmetry, as well as oscillations between odd and even modes that may be related to parity violation and phase correlations also detected in the data. While these analyses represent a step forward in building an understanding of the anomalies, a satisfactory explanation based on physically motivated models is still lacking.

The search for specific types of non-Gaussianity (NG) in the statistics of the CMB anisotropies provides important clues to the physical mechanism that originated the cosmological perturbations. Indeed, perturbations generated during inflation are expected to display specific forms of NG. Different inflationary models, firmly rooted in modern theoretical particle physics, predict different *amplitudes* and *shapes* of NG. Thus, constraints on primordial NG are complementary to constraints on the scalar spectral index of curvature perturbations and the tensor-to-scalar ratio, lifting the degeneracy among inflationary models that predict the same power-spectra. The level of NG predicted by the simplest models of inflation, consisting of a single slowly-rolling scalar field, is low and undetectable even by *Planck*. However, extensions of the simplest paradigm generically lead to levels of NG in CMB anisotropies that should be detectable. A detection of primordial NG would rule out *all* canonical single-field slow-roll models of inflation, pointing to physics beyond the simplest inflation model. Conversely, a significant upper bound on the level of primordial NG, as we have obtained, severely limits extensions of the simplest paradigm.

Inflationary NG can be characterized by the dimensionless non-linearity parameter $f_{\rm NL}$ (see Planck Collaboration XXIV (2013) for more details), which measures the amplitude of primordial NG of quadratic type in the comoving curvature perturbation mode. We have estimated $f_{\rm NL}$ for various NG shapes – including the three fundamental ones, *local*, *equilateral*, and *orthogonal* – predicted by different classes of inflationary models. Results for these three fundamental shapes are reported in Table 10, which gives independent estimates for each contribution. These results have been obtained using a suite of optimal bispectrum estimators (see (Planck Collaboration XXIV 2013), where a full description of the procedure, as well as of the validation tests can also be found). The reported values have been obtained after marginalizing over the Poissonian bispectrum contribution of diffuse point-sources and subtracting the bias due to the secondary bispectrum arising from the coupling of the Integrated Sachs-Wolfe (ISW) effect and the weak gravitational lensing of CMB photons (see Planck Collaboration XIX (2013) for more details). We also obtain constraints on key, primordial, non-Gaussian paradigms, including non-separable single-field models, excited initial states (non-Bunch-Davies vacua), and directionally-dependent vector field models, and we provide an initial survey of scale-dependent features and resonance models. The absence of significant non-Gaussianity implies that the speed of sound of the inflaton field in these models must be within two orders of magnitude of the speed of light.

Moreover, we derive bispectrum constraints on a selection of specific inflationary mechanisms, including both general single-field inflationary models and multifield ones. Our results lead to a lower bound on the speed of sound, $c_s > 0.02$ (95 % CL), in the effective field theory parametrization of the inflationary model space. Moving beyond the bispectrum, *Planck* data also provide an upper limit on the amplitude of the trispectrum in the local NG model, $\tau_{\rm NL} < 2800$ (95 % CL).

The *Planck* data have been used to provide stringent new constraints on cosmic strings and other defects (see (Planck Collaboration XXV 2013)). Using CMB power-spectrum forecasts for cosmic strings, we have used the *Planck* likelihoods to obtain the new limits $G\mu/c^2 < 1.5 \times 10^{-7}$ for Nambu strings and $G\mu/c^2 < 3.2 \times 10^{-7}$ for field theory strings. Tighter constraints for joint analysis with high$-\ell$ data are also described, along with results for textures and semi-local strings. Complementary non-Gaussian searches using different methodologies also find no evidence for cosmic strings with somewhat weaker constraints.

Table 10. Separable template-fitting estimates of primordial $f_{\rm NL}$ for local, equilateral, orthogonal shapes, as obtained from SMICA foreground cleaned maps, after marginalizing over the Poissonian point-source bispectrum contribution and subtracting the ISW-lensing bias. Uncertainties are 1σ.

$f_{\rm NL}$		
Local	Equilateral	Orthogonal
2.7 ± 5.8	-42 ± 75	-25 ± 39

Alternative geometries and non-trivial topologies have also been analyzed (see (Planck Collaboration XXVI 2013) for more details). The Bianchi VII$_h$ models, including global rotation and shear, have been constrained, with the vorticity parameter $\omega_0 < 10^{-9} H_0$ at 95 % confidence. Topological models are constrained by the lack of matched circles or other evidence of large-scale correlation signatures, limiting the scale of the fundamental domain to the size of the diameter of the scattering surface in a variety of specific models.

9.3. CMB polarization

The current data release and scientific results are based on CMB temperature data only. *Planck* measures polarization from 30 to 353 GHz, and both Data Processing Centres routinely produce polarization products. The analysis of polarization data is more complicated than that of temperature data, and is therefore in a less advanced state. There are several reasons for this: the response of each detector to polarization is difficult to calibrate due to the lack of celestial standard sources; the amplitude of the polarized CMB signal is low and astrophysical foregrounds dominate over the CMB over the whole sky; and the detection of polarized signals is subject to specific systematic effects. An example of the last of these is leakage of total intensity into the polarization maps. This can occur because *Planck* measures polarization by differentiating a common intensity mode from detectors sensitive to linear polarization with different orientations, and there are differential calibration errors between pairs of detectors. Nevertheless, strong polarized synchrotron and thermal dust emission from the Galaxy are currently being imaged with high significance (see Sect. 8.2.4).

These issues are not yet resolved at a level satisfactory for cosmological analysis at large angular scales (ℓ <100). At smaller angular scales, however, systematic effects are subdominant and uncertainties are dominated by residual detector noise. At high Galactic latitudes, CMB polarization is being measured by *Planck* with unprecedented sensitivity at angular scales smaller than a few degrees.

Planck's capability to detect polarization is well illustrated by the use of stacking to enhance the measurement of polarization around CMB peaks. Adiabatic scalar fluctuations predict a specific polarization pattern around cold and hot spots, and this pattern is what we seek to image. We used ILC estimates (Eriksen et al. 2004) of the CMB I, Q, and U maps from 100 to 353 GHz, degraded to an HEALPix resolution of $N_{\rm side} = 512$ and smoothed to 30 arc-minutes. After applying the *Planck* mask used for component separation (Planck Collaboration XII 2013), we find on the remaining 71 % of the sky 11 396 cold spots and 10 468 hot spots, consistent with the ΛCDM *Planck* best fit model prediction (which anticipates $4\pi f_{\rm sky} \bar{n}_{\rm peak} = 11073$ hot and cold spots each). Around each of these temperature extrema, we extract $5^\circ \times 5^\circ$ square maps that we co-add to produce stacked maps for I, Q and U. Q and U stacked maps are then rotated in the temperature extrema radial frame $Q_r(\theta)$ and $U_r(\theta)$ (Kamionkowski et al. 1997). In this reference frame the standard model predicts $Q_r(\theta)$ alternating between positive (radial polarization) and negative (tangential polarization) values and $U_r(\theta) = 0$.

Figure 27 shows the stacked I and Q_r (Q in the radial frame) maps for cold and hot spots, computed from the *Planck* data and compared to the ΛCDM *Planck* best fit. Measurements extracted from the stacked maps are in very good agreement with the *Planck* best-fit model. The combined best fit amplitude is 0.999 ± 0.010 (68 % CL) leading to a statistical significance of the detection larger than 95σ.

The most interesting cosmological signal visible in polarization is the very large-scale ($\ell < 10$) E-mode peak due to reionization, at a typical brightness level of $0.3\,\mu$K. At the present stage of analysis, and with the data currently available, there are unexplained residuals in the survey-to-survey difference maps that are comparable to or larger than an expected B-mode signal. For these reasons, we are delaying the use of CMB polarization measurements from *Planck* from cosmological analysis until we have a firmer understanding and control of such systematic effects.

9.4. The ISW effect

In the spatially flat Universe clearly established by *Planck*, the detection of the integrated Sachs-Wolfe (ISW) effect provides complementary evidence of the accelerated expansion of the universe, governed by some form of Dark Energy. The high sensitivity, high resolution and full-sky coverage of *Planck* has permitted us, for the first time, to obtain evidence of the ISW directly from CMB measurements, via the non-Gaussian signal induced by the cross-correlation of the secondary anisotropies due to the ISW itself and the lensing clearly detected by *Planck* (Planck Collaboration XVII 2013). Following this approach, we report an ISW detection of $\approx 2.5\sigma$ from the CMB alone.

In addition, we have also confirmed (Planck Collaboration XIX 2013) the ISW signal by cross-correlating the clean CMB maps produced by *Planck* with several galaxy catalogues, which act as tracers of the gravitational potential. This standard technique provides an overall detection of $\approx 3\,\sigma$, by combining information from all the surveys at the same time. This figure is somewhat weaker than previous claims made from *WMAP* data (e.g., Ho et al. 2008; Giannantonio et al. 2012). Differences do not seem to be related to the CMB data itself, but rather to the way in which the uncertainties are computed and, especially, to the characterization of the galaxy catalogues. A clear agreement with previous detection claims ($\lesssim 3\,\sigma$) using the NVSS data is reported. The ISW amplitude estimation made with *Planck* is in very good agreement with the theoretical expectation (which depends on such characterizations), whereas deviations of more than $1\,\sigma$ were found in previous works. These results give support and robustness to our findings.

The ISW signal induced by isolated features in the large-scale structure of the universe has also been studied. In particular, we have stacked the CMB fluctuations in the positions of voids and super-clusters, showing a clear detection (above $3\,\sigma$ and almost $3\,\sigma$ for voids and clusters, respectively) of a secondary anisotropy. The results are compatible with previous claims made with *WMAP* data (Granett et al. 2008), and the most likely origin of the secondary anisotropy is the time evolution of the gravitational potential associated to those structures. However, the signal initially detected is at odds in scale and am-

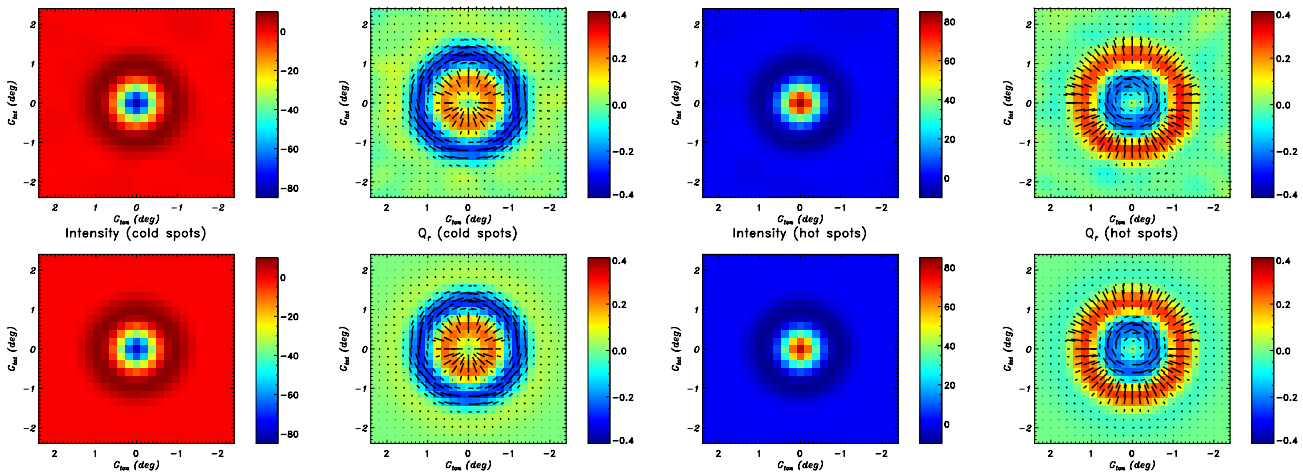

Fig. 27. Stacked maps of the CMB intensity I and polarization Q_r at the position of the temperature extrema, at a common resolution of 30 arcmin. Maps are displayed for CMB temperature cold spots (left) and hot spots (right) for the *Planck* CMB estimates (top row) and for the ΛCDM*Planck* best fit model prediction (bottom row).

plitude with expectations of a pure ISW effect. Using more recent void catalogues leads to the detection of a signal at up to $2.5\,\sigma$ with scales and amplitudes more consistent with expectations of the ISW effect. Taking advantage of the large frequency coverage of *Planck*, we have confirmed that the stacked signal is stable from 44 to 353 GHz, supporting the cosmological origin of this detection.

9.5. The cosmic infrared background

CIB anisotropies are expected to trace large-scale structures and probe the clustering properties of galaxies, which in turn are linked to those of their host dark matter halos. Because the clustering of dark matter is well understood, observations of anisotropies in the CIB constrain the relationship between dusty, star-forming galaxies and the dark matter distribution. Correlated anisotropies also depend on the mean emissivity per comoving unit volume of dusty, star-forming galaxies and can be used to measure the star formation history.

The extraction of CIB anisotropies in *Planck*/HFI (Planck Collaboration XVIII 2011; Planck Collaboration XXXII 2013) is limited by our ability to separate the CIB from the CMB and the Galactic dust. At multipole ℓ=100, the power spectrum of the CIB anisotropies has an amplitude less than 0.2 % of the CMB power spectrum at 217 GHz, and less than 25 % of the dust power spectrum in very diffuse regions of the sky ($N_{HI} < 2.5 \times 10^{20} cm^{-2}$) at 857 GHz. Using HI data from three radio telescopes (Parkes, GBT and Effelsberg) and cleaning the CMB using the 100 GHz map as a template, it has been possible to obtain new measurements of the CIB anisotropies with *Planck*/HFI. The CIB has been extracted from the maps on roughly 2300 square degrees (Planck Collaboration XXXII 2013). Auto- and cross-power spectra have been computed, from 217 to 3000 GHz, using both *Planck*HFI and *IRAS*. Two approaches have been developed to model the power spectra. The first one uses only the linear part of the clustering and gives strong constraints on the evolution of the star formation rate up to high redshift. The second one is based on a parametrized relation between the dust-processed infrared luminosity and (sub-)halo mass, probing the interplay between baryonic and dark matter throughout cosmic times at an unmatched redshift depth, complementing current and foreseeable optical or near-infrared measurements.

9.6. Lensing and the cosmic infrared background

Planck's multi-frequency observations provide information on both the integrated history of star formation (via the CIB) and the distribution of dark matter (via the lensing effect on the cosmic microwave background, or CMB). In the upper frequency bands (353, 545, and 857 GHz), the dominant extragalactic signal is not the CMB, but the CIB, composed of redshifted thermal radiation from UV-heated dust, enshrouding young stars. The CIB contains much of the energy from processes involved in structure formation. According to current models, the dusty star-forming galaxies (DSFGs) that give rise to the CIB have a redshift distribution peaked between $z \sim 1$ and $z \sim 2$, and tend to live in 10^{11}–10^{13} $M_\odot$ dark matter halos.

Gravitational lensing by large-scale structure produces small shear and magnification effects in the observed fluctuations, which can be exploited to reconstruct an integrated measure of the gravitational potential along the line of sight. This "CMB lensing potential" is sourced primarily by dark matter halos located at $1 \lesssim z \lesssim 3$, halfway between ourselves and the last scattering surface.

The conjunction of these two unique probes allows us to measure directly the connection between dark and luminous matter in the high redshift ($1 \leq z \leq 3$) Universe (Planck Collaboration XVIII 2013). We use a three-point statistic optimized to detect the correlation between these two tracers. We report the first detection of the correlation between the CIB and CMB lensing using *Planck* data only. The well matched redshift distribution of these two signals leads to a detection significance with a peak value of $42\,\sigma$ at 545 GHz. Equivalently, we measure a correlation as high as 80 % across these two tracers. Our full set of multi-frequency measurements (both CIB auto- and CIB-lensing cross-spectra) are consistent with a simple halo-based model, with a characteristic mass scale for the halos hosting CIB sources of $\log_{10}(M/M_\odot) = 11.6 \pm 1.5$. Leveraging the frequency dependence of our signal, we isolate the high redshift contribution to the CIB, and constrain the star formation rate (SFR) density at $z \geq 1$. We measure directly the SFR density with around $4\,\sigma$ significance for three redshift bins between $z = 1$ and 7, thus

opening a new window into the study of the formation of stars at early times.

To get a better intuition for this detection, we show in Fig. 28 the real-space correlation between the observed temperature and the lens deflection angles. This figure allows us to visualize the correlation between the CIB and the CMB lensing deflection angles for the first time. These images were generated using a stacking technique, as described in Planck Collaboration XVIII (2013). We select ∼20000 local maxima and an equal number of local minima, stack them in one-degree squares, then take the gradient of the stacked lensing potential to calculate the deflection angles, which we display in Fig. 28 as arrows. The result of the stacking over the maxima, minima and random points is displayed from left to right in Fig. 28. The strong correlation seen already in the cross-power spectrum is clearly visible in both the 545 and 857 GHz extrema, while the stacking on random locations leads to a lensing signal consistent with noise. As expected, we see that the temperature maxima of the CIB, which contain a larger than average number of galaxies, deflect light inward, i.e., they correspond to gravitational potential wells, while temperature minima trace regions with fewer galaxies and deflect light outward, i.e., they correspond to gravitational potential hills.

9.7. Cosmology from Planck Sunyaev–Zeldovich emission

Clusters of galaxies are good tracers of the evolution and content of the Universe. In paper (Planck Collaboration XX 2013), we present constraints obtained with a well defined sample of 189 clusters (see also Sect. 8.1.2) for which we have computed the selection function. This sample has a high S/N threshold (7) to ensure 100 % reliability and to maximize the number of redshifts (188). Using a relation between mass and SZ signal based on comparison to X-ray measurements, we derive constraints on the matter power spectrum amplitude σ_8 and matter density parameter Ω_m in a flat ΛCDM model. Assuming a bias between the X-ray determined mass and the true mass of 20 %, motivated by comparison of the observed mass scaling relations to those from several sets of numerical simulations, we find that $\sigma_8(\Omega_m/0.27)^{0.3} = 0.78 \pm 0.01$, with one-dimensional ranges $\sigma_8 = 0.77 \pm 0.02$ and $\Omega_m = 0.29 \pm 0.02$. This result appears to be robust against the S/N cut, choice of sub-sample, mass function or completeness assumptions.

In addition to the above analysis based on cluster counts, we can derive cosmological constraints from the power spectrum of tSZ emission (see Sect. 8.2.5, Planck Collaboration XXI (2013)). We have compared the *Planck* angular power spectrum of the diffuse thermal SZ emission (tSZ) to theoretical models in order to set cosmological constraints. The two analyses exhibit a similar degeneracy relation between σ_8 and Ω_m. In particular, we measure $\sigma_8(\Omega_m/0.28)^{3.2/8.1} = 0.772 \pm 0.013$, with one-dimensional ranges $\sigma_8 = 0.76 \pm 0.04$ and $\Omega_m = 0.29 \pm 0.03$ in full agreement the constraints derived from SZ cluster counts.

The tSZ effect secondary anisotropies are expected to be non-Gaussian and thus extra and independent cosmological information can be extracted from the higher-order moments of their distribution and from their bispectrum. By computing the 1D probability distribution function of the tSZ map we find $\sigma_8 = 0.78 \pm 0.02$, compatible with the bispectrum-based estimate of $\sigma_8 = 0.74 \pm 0.04$.

While these analyses show good consistency on the constraints from the SZ signal detected by *Planck* (and with other cluster measurements), they favour somewhat low values of σ_8 and Ω_m as compared to the CMB analysis (Sect. 9.1. This tension can be alleviated either by relaxing our assumption on the bias between X-ray mass and true mass, and/or by assuming massive neutrinos.

10. Summary and Conclusions

This paper summarises the data products and scientific results of the *Planck* satellite based on its first 15.5 months of survey operations. Detailed descriptions of all aspects of the *Planck* science in this 2013 release are provided in accompanying papers (Planck Collaboration 2013 II - XXIX).

Considering that the *Planck* satellite and its complex cryogenic payload have operated without interruption over a lifetime that is longer than initially planned by a factor of ∼2, and that the performance of its payload is the same or better than expected from pre-launch ground testing, we can conclude that it has been a tremendous technical success. And it continues in fact to operate, albeit with a reduced instrumental capability.

The 2013 release of data products from *Planck* fulfills the promise made at the mission's inception in 1995 by delivering: (a) a set of nine well-characterised frequency maps in which systematic effects do not play the dominant role, and with subpercent calibration accuracy across the CMB channels; (b) mapping of the temperature anisotropies of the CMB that is limited only by unresolved foregrounds down to an angular resolution of 5 arcminutes; (c) a catalogue of compact Galactic and extragalactic sources that represents an important improvement over the Early Release Compact Source Catalogue released in January 2011; (d) a list of extragalactic sources detected via the Sunyaev-Zeldovich effect, which increases by a factor of ∼10 the number of galaxy clusters previously detected by this technique; (e) a first-generation set of maps of diffuse foregrounds that absorb the main sources of Galactic emission - thermal dust and the cosmic infrared background at high frequencies and synchrotron, free-free, and anomalous emission at low frequencies.

In addition to these "promised" products, *Planck* is providing in this release: an all-sky map of dust opacity that represents an important improvement over the best previous *IRAS*-based product; an all-sky map of the CMB lensing deflection field that, although dominated by noise, represents the first ever in its category; all-sky maps of the integrated emission of carbon monoxide, an important tracer of the interstellar medium; and the first measurement of the angular power spectrum of the diffuse Sunyaev-Zeldovich emission over a large part of the sky.

The main cosmological results of *Planck* at the current time can be summarised as follows:

- using a likelihood approach that combines *Planck* CMB and lensing data, CMB data from ACT and SPT at high ℓs, and *WMAP* polarized CMB data at low ℓs, we have estimated the values of a "vanilla" 6-parameter ΛCDM model with the highest accuracy ever. These estimates are highly robust, as demonstrated by the use of multiple methods based both on likelihood and on component-separated maps.
- The parameters of the *Planck* best-fit 6-parameter ΛCDM are significantly different than previously estimated. In particular, with respect to pre-*Planck* values, we find a weaker cosmological constant (by ∼2 %), more baryons (by ∼3 %), and more cold dark matter (by ∼5 %). The spectral index of primordial fluctuations is firmly established to be below unity, even when extending the ΛCDM model to more parameters.
- we find no significant improvements to the best-fit model when extending the set of parameters beyond 6, implying no need for new physics to explain the *Planck* measurements.

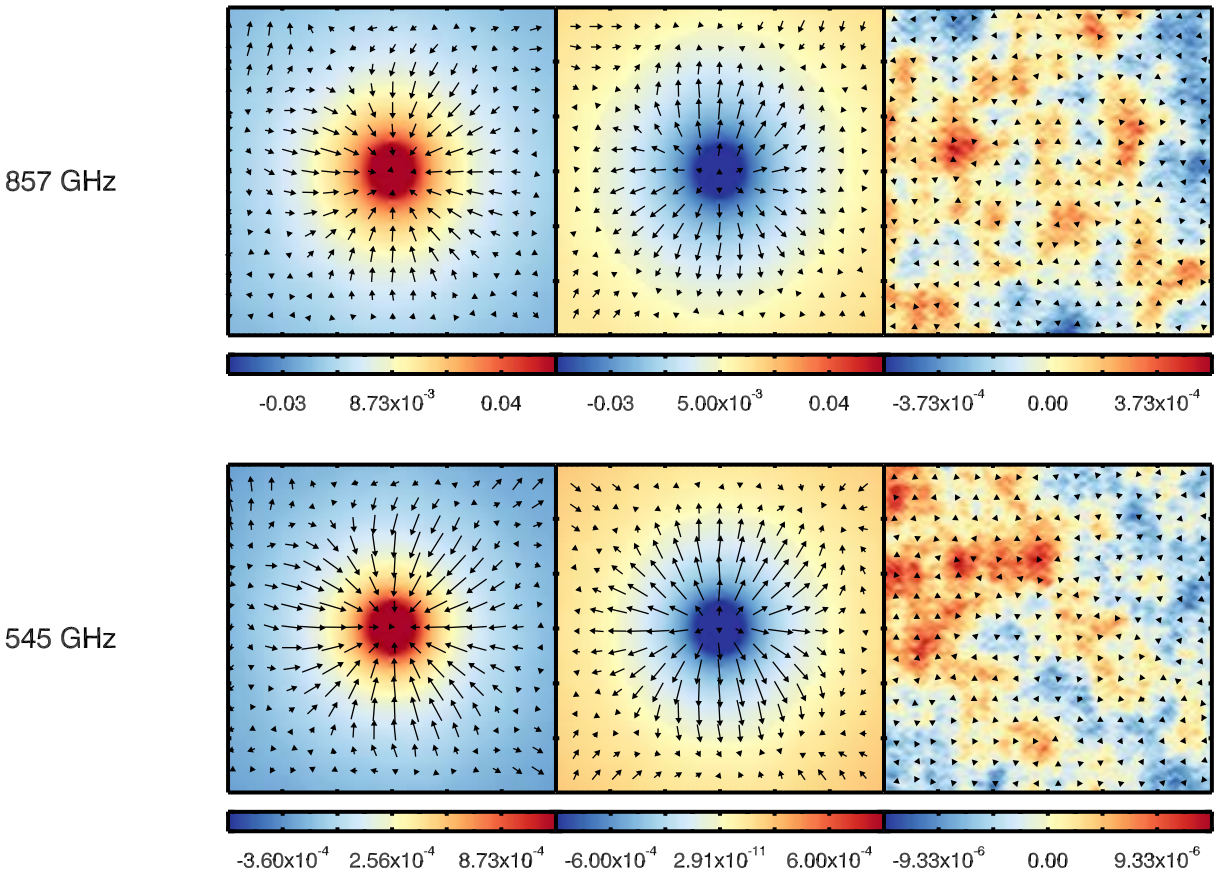

Fig. 28. Temperature maps of size 1 deg^2 at 545 and 857 GHz stacked on the 20,000 brightest peaks (left column), troughs (centre column) and random map locations (right column). The stacked (averaged) temperature maps is in K. The arrows indicate the lensing deflection angle deduced from the gradient of the band-pass filtered lensing potential map stacked on the same peaks. The longest arrow corresponds to a deflection of 6.3′′, which is only a fraction of the total deflection angle because of our filtering. This stacking allows us to visualize in real space the lensing of the CMB by the galaxies that generate the CIB. The small offset between the peak of the lensing potential and the CIB is due to noise in the stacked lensing potential map. We choose the same random locations for both frequencies, hence the similar pattern seen in the top and bottom right panels.

- The *Planck* best-fit model is in excellent agreement with the most current BAO data. However, it requires a Hubble constant that is significantly lower (∼67 km s^{-1} Mpc^{-1}) than expected from traditional measurement techniques, raising the possibility of systematic effects in the latter.
- An exploration of parameter space beyond the basic set leads to: (a) firmly establishing the effective number of relativistic species (neutrinos) at 3; (b) constraining the flatness of space-time to a level of 0.1%; (c) setting significantly improved constraints on the total mass of neutrinos, the abundance of primordial Helium, and the running of the spectral index of the power spectrum.
- we find no evidence at the current level of analysis for tensor modes, nor for a dynamical form of dark energy, nor for time variations of the fine structure constant.
- we find some tension between the amplitude of matter fluctuations (σ_8) derived from CMB data and that derived from Sunyaev-Zeldovich data; we attribute this tension to uncertainties in cluster physics that affect the latter.
- we find important support for single-field slow-roll inflation via our constraints on running of the spectral index, curvature and f_{NL}.
- The *Planck* data squeezes the region of the allowed standard inflationary models, preferring a concave potential: power law inflation, the simplest hybrid inflationary models, and simple monomial models with $n > 2$, do not provide a good fit to the data.
- we find no evidence for statistical deviations from isotropy at ℓ >50, to very high precision.
- we do find evidence for deviations from isotropy at low ℓs. In particular, we find a coherent deficit of power with respect to our best-fit ΛCDMmodel at ℓs between ∼20 and 30.
- We confirm the existence of the so-called *WMAP* anomalies.

These results highlight the maturity and high precision being achieved in our understanding of the Universe, and at the same time herald a new era in which we can no longer ignore tiny but significant deviations at low ℓs from our current standard model.

Other results for which the current *Planck* data are making unique contributions are:

- a 25σ detection of the distortion of the CMB due to lensing by intervening structure yields a (noisy but highly significant) map over most of the sky of the integrated distribution of mass back to the CMB last-scattering surface. The detection of lensing helps *Planck* to break parameter degeneracies, in particular to constrain the reionization optical depth without the help of polarization data.

- the first detection at high significance (42σ) of the cross-correlation between CMB lensing and the cosmic infrared background, which allows us to constrain the star formation rate at high redshifts.
- the measurement of the angular power spectrum of the cosmic infrared background over a large area and at frequencies as low as 217 GHz, which allows us to constrain the properties of dark matter halos at high redshifts.
- the first all-sky map of the diffuse Sunyaev-Zeldovich emission, which has been used to build a corresponding angular power spectrum between ℓs ∼20-1000, and used to constrain the amplitude of matter fluctuations (σ_8).
- the first robust (2.5σ) detection of the Integrated Sachs-Wolfe effect via its cross-correlation with *Planck*-detected lensing, providing independent evidence for Ω_Λ ∼0.7.

The *Planck* 2013 release does not include polarization products, and our current cosmological analysis does not rely on *Planck* polarization, and only mildly on *WMAP* polarization data. However, we have shown that quite basic processing of the CMB polarization already yields angular power spectra in excellent consistency with the *Planck* best-fit cosmology, derived from temperature data only. Analysis of the stacking of hot and cold CMB peaks shows spectacular agreement with expectations, and demonstrates the potential of the *Planck*'s CMB polarization measurements. A number of papers on polarized dust emission are due to be published within a few months. All these points show that the processing of *Planck* polarization data is well advanced, with the goal to release polarized data and associated CMB-based results in mid-2014.

Acknowledgements. *Planck* is too large a project to allow full acknowledgement of all contributions by individuals, institutions, industries, and funding agencies. The main entities involved in the mission operations are as follows. The European Space Agency operates the satellite via its Mission Operations Centre located at ESOC (Darmstadt, Germany) and coordinates scientific operations via the *Planck* Science Office located at ESAC (Madrid, Spain). Two Consortia, comprising around 100 scientific institutes within Europe, the USA, and Canada, and funded by agencies from the participating countries, developed the scientific instruments LFI and HFI, and continue to operate them via Instrument Operations Teams located in Trieste (Italy) and Orsay (France). The Consortia are also responsible for scientific processing of the acquired data. The Consortia are led by the Principal Investigators: J.-L. Puget in France for HFI (funded principally by CNES and CNRS/INSU-IN2P3) and N. Mandolesi in Italy for LFI (funded principally via ASI). NASA's US *Planck* Project, based at JPL and involving scientists at many US institutions, contributes significantly to the efforts of these two Consortia. A third Consortium, led by H. U. Norgaard-Nielsen and supported by the Danish Natural Research Council, contributed to the reflector programme. The author list for this paper has been selected by the *Planck* Science Team from the Planck Collaboration, and is composed of individuals from all of the above entities who have made multi-year contributions to the development of the mission. It does not pretend to be inclusive of all contributions to *Planck*. A description of the Planck Collaboration and a list of its members, indicating which technical or scientific activities they have been involved in, can be found at *(http://www.rssd.esa.int/index.php?project=PLANCK& page=Planck_Collaboration)*. The Planck Collaboration acknowledges the support of: ESA; CNES and CNRS/INSU-IN2P3-INP (France); ASI, CNR, and INAF (Italy); NASA and DoE (USA); STFC and UKSA (UK); CSIC, MICINN and JA (Spain); Tekes, AoF and CSC (Finland); DLR and MPG (Germany); CSA (Canada); DTU Space (Denmark); SER/SSO (Switzerland); RCN (Norway); SFI (Ireland); FCT/MCTES (Portugal); and PRACE (EU).

References

Anderson, L., Aubourg, E., Bailey, S., et al. 2012, MNRAS, 427, 3435
Bennett, C. L., Halpern, M., Hinshaw, G., et al. 2003, ApJS, 148, 1
Bennett, C. L., Larson, D., Weiland, J. L., et al. 2012, ArXiv e-prints
Bersanelli, M., Mandolesi, N., Butler, R. C., et al. 2010, A&A, 520, A4+
Böhringer, H., Schuecker, P., Guzzo, L., et al. 2004, A&A, 425, 367
Böhringer, H., Voges, W., Huchra, J. P., et al. 2000, ApJS, 129, 435
Burenin, R. A., Vikhlinin, A., Hornstrup, A., et al. 2007, ApJS, 172, 561
Calabrese, E., Hlozek, R. A., Battaglia, N., et al. 2013, ArXiv e-prints
Condon, J. J., Cotton, W. D., Greisen, E. W., et al. 1998, AJ, 115, 1693
Conley, A., Guy, J., Sullivan, M., et al. 2011, ApJS, 192, 1
Dunkley, J., Calabrese, E., Sievers, J., et al. 2013, ArXiv e-prints
Dunkley, J., Hlozek, R., Sievers, J., et al. 2011, ApJ, 739, 52
Eales, S., Dunne, L., Clements, D., et al. 2010, PASP, 122, 499
Ebeling, H., Barrett, E., Donovan, D., et al. 2007, ApJ, 661, L33
Erben, T., Hildebrandt, H., Miller, L., et al. 2012, ArXiv e-prints
Eriksen, H. K., Banday, A. J., Górski, K. M., & Lilje, P. B. 2004, ApJ, 612, 633
Finkbeiner, D. P., Davis, M., & Schlegel, D. J. 1999, ApJ, 524, 867
Fixsen, D. J. 2009, ApJ, 707, 916
Fraisse, A. A., Ade, P. A. R., Amiri, M., et al. 2011, ArXiv e-prints
Freedman, W. L., Madore, B. F., Scowcroft, V., et al. 2012, ApJ, 758, 24
Giannantonio, T., Crittenden, R., Nichol, R., & Ross, A. J. 2012, MNRAS, 426, 2581
González-Nuevo, J., Argüeso, F., López-Caniego, M., et al. 2006, MNRAS, 369, 1603
Górski, K. M., Hivon, E., Banday, A. J., et al. 2005, ApJ, 622, 759
Granett, B. R., Neyrinck, M. C., & Szapudi, I. 2008, ApJ, 683, L99
Griffin, M. J., Abergel, A., Abreu, A., et al. 2010, A&A, 518, L3
Healey, S. E., Romani, R. W., Taylor, G. B., et al. 2007, ApJS, 171, 61
Heymans, C., Van Waerbeke, L., Miller, L., et al. 2012, MNRAS, 427, 146
Hinshaw, G., Larson, D., Komatsu, E., et al. 2012a, ArXiv e-prints
Hinshaw, G., Larson, D., Komatsu, E., et al. 2012b, ArXiv e-prints
Hinshaw, G., Larson, D., Komatsu, E., et al. 2012c, ArXiv e-prints
Hinshaw, G., Weiland, J. L., Hill, R. S., et al. 2009, ApJS, 180, 225
Ho, S., Hirata, C., Padmanabhan, N., Seljak, U., & Bahcall, N. 2008, Phys. Rev. D, 78, 043519
Jarosik, N., Bennett, C. L., Dunkley, J., et al. 2011, ApJS, 192, 14
Kalberla, P. M. W., Burton, W. B., Hartmann, D., et al. 2005, A&A, 440, 775
Kamionkowski, M., Kosowsky, A., & Stebbins, A. 1997, Phys. Rev. D, 55, 7368
Keihänen, E., Keskitalo, R., Kurki-Suonio, H., Poutanen, T., & Sirviö, A. 2010, A&A, 510, A57+
Keisler, R., Reichardt, C. L., Aird, K. A., et al. 2011, ApJ, 743, 28
Kelsall, T., Weiland, J. L., Franz, B. A., et al. 1998, ApJ, 508, 44
Koester, B. et al. 2007, Astrophys.J., 660, 239
Kosowsky, A. 2003, New A Rev., 47, 939
Lamarre, J., Puget, J., Ade, P. A. R., et al. 2010, A&A, 520, A9+
López-Caniego, M., Herranz, D., González-Nuevo, J., et al. 2006, MNRAS, 370, 2047
Massardi, M., López-Caniego, M., González-Nuevo, J., et al. 2009, MNRAS, 392, 733
Mather, J. C., Fixsen, D. J., Shafer, R. A., Mosier, C., & Wilkinson, D. T. 1999, ApJ, 512, 511
Mennella, A., Butler, R. C., Curto, A., et al. 2011, A&A, 536, A3
Mitra, S., Rocha, G., Górski, K. M., et al. 2011, ApJS, 193, 5
Miville-Deschênes, M.-A. & Lagache, G. 2005, ApJS, 157, 302
Murphy, T., Sadler, E. M., Ekers, R. D., et al. 2010, MNRAS, 402, 2403
Planck Collaboration. 2005, ESA publication ESA-SCI(2005)/01
Planck Collaboration. 2011, The Explanatory Supplement to the Planck Early Release Compact Source Catalogue (ESA)
Planck Collaboration. 2013, Submitted to A&A
Planck Collaboration ES. 2013, The Explanatory Supplement to the Planck 2013 results (ESA)
Planck Collaboration I. 2011, A&A, 536, A1
Planck Collaboration II. 2011, A&A, 536, A2
Planck Collaboration II. 2013, Submitted to A&A
Planck Collaboration III. 2013, Submitted to A&A
Planck Collaboration Int. VII. 2013, A&A, 550, A133
Planck Collaboration IV. 2013, Submitted to A&A
Planck Collaboration IX. 2011, A&A, 536, A9
Planck Collaboration IX. 2013, Submitted to A&A
Planck Collaboration V. 2013, Submitted to A&A
Planck Collaboration VI. 2013, Submitted to A&A
Planck Collaboration VII. 2011, A&A, 536, A7
Planck Collaboration VII. 2013, Submitted to A&A
Planck Collaboration VIII. 2011, A&A, 536, A8
Planck Collaboration VIII. 2013, Submitted to A&A
Planck Collaboration X. 2011, A&A, 536, A10
Planck Collaboration X. 2013, Submitted to A&A
Planck Collaboration XI. 2011, A&A, 536, A11
Planck Collaboration XI. 2013, Submitted to A&A
Planck Collaboration XII. 2011, A&A, 536, A12
Planck Collaboration XII. 2013, Submitted to A&A
Planck Collaboration XIII. 2011, A&A, 536, A13
Planck Collaboration XIII. 2013, Submitted to A&A
Planck Collaboration XIV. 2011, A&A, 536, A14
Planck Collaboration XIV. 2013, Submitted to A&A

Planck Collaboration XIX. 2011, A&A, 536, A19
Planck Collaboration XIX. 2013, Submitted to A&A
Planck Collaboration XV. 2011, A&A, 536, A15
Planck Collaboration XV. 2013, Submitted to A&A
Planck Collaboration XVI. 2011, A&A, 536, A16
Planck Collaboration XVI. 2013, Submitted to A&A
Planck Collaboration XVII. 2011, A&A, 536, A17
Planck Collaboration XVII. 2013, Submitted to A&A
Planck Collaboration XVIII. 2011, A&A, 536, A18
Planck Collaboration XVIII. 2013, Submitted to A&A
Planck Collaboration XX. 2011, A&A, 536, A20
Planck Collaboration XX. 2013, Submitted to A&A
Planck Collaboration XXI. 2011, A&A, 536, A21
Planck Collaboration XXI. 2013, Submitted to A&A
Planck Collaboration XXII. 2011, A&A, 536, A22
Planck Collaboration XXII. 2013, Submitted to A&A
Planck Collaboration XXIII. 2011, A&A, 536, A23
Planck Collaboration XXIII. 2013, Submitted to A&A
Planck Collaboration XXIV. 2011, A&A, 536, A24
Planck Collaboration XXIV. 2013, Submitted to A&A
Planck Collaboration XXIX. 2013, Submitted to A&A
Planck Collaboration XXV. 2011, A&A, 536, A25
Planck Collaboration XXV. 2013, Submitted to A&A
Planck Collaboration XXVI. 2013, Submitted to A&A
Planck Collaboration XXVIII. 2013, Submitted to A&A
Planck Collaboration XXXII. 2013, In preparation
Planck HFI Core Team. 2011a, A&A, 536, A4
Planck HFI Core Team. 2011b, A&A, 536, A6
Reichardt, C. L., Shaw, L., Zahn, O., et al. 2012, ApJ, 755, 70
Reichborn-Kjennerud, B., Aboobaker, A. M., Ade, P., et al. 2010, in Society of Photo-Optical Instrumentation Engineers (SPIE) Conference Series, Vol. 7741, Society of Photo-Optical Instrumentation Engineers (SPIE) Conference Series
Riess, A. G., Macri, L., Casertano, S., et al. 2011, Astrophys.J., 730, 119
Ross, A. J., Ho, S., Cuesta, A. J., et al. 2011, Mon.Not.Roy.Astron.Soc., 417, 1350
Ruhl, J., Ade, P. A. R., Carlstrom, J. E., et al. 2004, in Society of Photo-Optical Instrumentation Engineers (SPIE) Conference Series, Vol. 5498, Society of Photo-Optical Instrumentation Engineers (SPIE) Conference Series, ed. C. M. Bradford, P. A. R. Ade, J. E. Aguirre, J. J. Bock, M. Dragovan, L. Duband, L. Earle, J. Glenn, H. Matsuhara, B. J. Naylor, H. T. Nguyen, M. Yun, & J. Zmuidzinas, 11–29
Schlegel, D. J., Finkbeiner, D. P., & Davis, M. 1998, ApJ, 500, 525
Sievers, J. L., Hlozek, R. A., Nolta, M. R., et al. 2013, ArXiv e-prints
Smoot, G. F., Bennett, C. L., Kogut, A., et al. 1992, ApJ, 396, L1
Spergel, D. N., Bean, R., Doré, O., et al. 2007, ApJS, 170, 377
Story, K. T., Reichardt, C. L., Hou, Z., et al. 2012, ArXiv e-prints
Sunyaev, R. A. & Zeldovich, Y. B. 1972, Comments on Astrophysics and Space Physics, 4, 173
Suzuki, N., Rubin, D., Lidman, C., et al. 2012, ApJ, 746, 85
Tauber, J. A., Mandolesi, N., Puget, J., et al. 2010a, A&A, 520, A1+
Tauber, J. A., Norgaard-Nielsen, H. U., Ade, P. A. R., et al. 2010b, A&A, 520, A2+
Tristram, M., Filliard, C., Perdereau, O., et al. 2011, A&A, 534, A88
van Engelen, A., Keisler, R., Zahn, O., et al. 2012, ApJ, 756, 142
Wright, E. L., Eisenhardt, P. R., Mainzer, A., et al. 2010, Astron.J., 140, 1868
Zacchei, A., Maino, D., Baccigalupi, C., et al. 2011, A&A, 536, A5

[1] APC, AstroParticule et Cosmologie, Université Paris Diderot, CNRS/IN2P3, CEA/lrfu, Observatoire de Paris, Sorbonne Paris Cité, 10, rue Alice Domon et Léonie Duquet, 75205 Paris Cedex 13, France
[2] Aalto University Metsähovi Radio Observatory, Metsähovintie 114, FIN-02540 Kylmälä, Finland
[3] African Institute for Mathematical Sciences, 6-8 Melrose Road, Muizenberg, Cape Town, South Africa
[4] Agenzia Spaziale Italiana Science Data Center, c/o ESRIN, via Galileo Galilei, Frascati, Italy
[5] Agenzia Spaziale Italiana, Viale Liegi 26, Roma, Italy
[6] Astrophysics Group, Cavendish Laboratory, University of Cambridge, J J Thomson Avenue, Cambridge CB3 0HE, U.K.
[7] Astrophysics & Cosmology Research Unit, School of Mathematics, Statistics & Computer Science, University of KwaZulu-Natal, Westville Campus, Private Bag X54001, Durban 4000, South Africa
[8] Atacama Large Millimeter/submillimeter Array, ALMA Santiago Central Offices, Alonso de Cordova 3107, Vitacura, Casilla 763 0355, Santiago, Chile
[9] CITA, University of Toronto, 60 St. George St., Toronto, ON M5S 3H8, Canada
[10] CNR - ISTI, Area della Ricerca, via G. Moruzzi 1, Pisa, Italy
[11] CNRS, IRAP, 9 Av. colonel Roche, BP 44346, F-31028 Toulouse cedex 4, France
[12] California Institute of Technology, Pasadena, California, U.S.A.
[13] Centre for Theoretical Cosmology, DAMTP, University of Cambridge, Wilberforce Road, Cambridge CB3 0WA U.K.
[14] Centro de Estudios de Física del Cosmos de Aragón (CEFCA), Plaza San Juan, 1, planta 2, E-44001, Teruel, Spain
[15] Computational Cosmology Center, Lawrence Berkeley National Laboratory, Berkeley, California, U.S.A.
[16] Consejo Superior de Investigaciones Científicas (CSIC), Madrid, Spain
[17] DSM/Irfu/SPP, CEA-Saclay, F-91191 Gif-sur-Yvette Cedex, France
[18] DTU Space, National Space Institute, Technical University of Denmark, Elektrovej 327, DK-2800 Kgs. Lyngby, Denmark
[19] Département de Physique Théorique, Université de Genève, 24, Quai E. Ansermet,1211 Genève 4, Switzerland
[20] Departamento de Física Fundamental, Facultad de Ciencias, Universidad de Salamanca, 37008 Salamanca, Spain
[21] Departamento de Física, Universidad de Oviedo, Avda. Calvo Sotelo s/n, Oviedo, Spain
[22] Department of Astronomy and Astrophysics, University of Toronto, 50 Saint George Street, Toronto, Ontario, Canada
[23] Department of Astrophysics/IMAPP, Radboud University Nijmegen, P.O. Box 9010, 6500 GL Nijmegen, The Netherlands
[24] Department of Electrical Engineering and Computer Sciences, University of California, Berkeley, California, U.S.A.
[25] Department of Physics & Astronomy, University of British Columbia, 6224 Agricultural Road, Vancouver, British Columbia, Canada
[26] Department of Physics and Astronomy, Dana and David Dornsife College of Letter, Arts and Sciences, University of Southern California, Los Angeles, CA 90089, U.S.A.
[27] Department of Physics and Astronomy, University College London, London WC1E 6BT, U.K.
[28] Department of Physics, Gustaf Hällströmin katu 2a, University of Helsinki, Helsinki, Finland
[29] Department of Physics, Princeton University, Princeton, New Jersey, U.S.A.
[30] Department of Physics, University of California, Berkeley, California, U.S.A.
[31] Department of Physics, University of California, One Shields Avenue, Davis, California, U.S.A.
[32] Department of Physics, University of California, Santa Barbara, California, U.S.A.
[33] Department of Physics, University of Illinois at Urbana-Champaign, 1110 West Green Street, Urbana, Illinois, U.S.A.
[34] Dipartimento di Fisica e Astronomia G. Galilei, Università degli Studi di Padova, via Marzolo 8, 35131 Padova, Italy
[35] Dipartimento di Fisica e Scienze della Terra, Università di Ferrara, Via Saragat 1, 44122 Ferrara, Italy
[36] Dipartimento di Fisica, Università La Sapienza, P. le A. Moro 2, Roma, Italy
[37] Dipartimento di Fisica, Università degli Studi di Milano, Via Celoria, 16, Milano, Italy
[38] Dipartimento di Fisica, Università degli Studi di Trieste, via A. Valerio 2, Trieste, Italy
[39] Dipartimento di Fisica, Università di Roma Tor Vergata, Via della Ricerca Scientifica, 1, Roma, Italy
[40] Discovery Center, Niels Bohr Institute, Blegdamsvej 17, Copenhagen, Denmark
[41] Dpto. Astrofísica, Universidad de La Laguna (ULL), E-38206 La Laguna, Tenerife, Spain

[42] European Southern Observatory, ESO Vitacura, Alonso de Cordova 3107, Vitacura, Casilla 19001, Santiago, Chile
[43] European Space Agency, ESAC, Camino bajo del Castillo, s/n, Urbanización Villafranca del Castillo, Villanueva de la Cañada, Madrid, Spain
[44] European Space Agency, ESAC, Planck Science Office, Camino bajo del Castillo, s/n, Urbanización Villafranca del Castillo, Villanueva de la Cañada, Madrid, Spain
[45] European Space Agency, ESOC, Robert-Bosch-Str. 5, Darmstadt, Germany
[46] European Space Agency, ESTEC, Keplerlaan 1, 2201 AZ Noordwijk, The Netherlands
[47] Finnish Centre for Astronomy with ESO (FINCA), University of Turku, Väisäläntie 20, FIN-21500, Piikkiö, Finland
[48] Haverford College Astronomy Department, 370 Lancaster Avenue, Haverford, Pennsylvania, U.S.A.
[49] Helsinki Institute of Physics, Gustaf Hällströmin katu 2, University of Helsinki, Helsinki, Finland
[50] INAF - Osservatorio Astrofisico di Catania, Via S. Sofia 78, Catania, Italy
[51] INAF - Osservatorio Astronomico di Padova, Vicolo dell'Osservatorio 5, Padova, Italy
[52] INAF - Osservatorio Astronomico di Roma, via di Frascati 33, Monte Porzio Catone, Italy
[53] INAF - Osservatorio Astronomico di Trieste, Via G.B. Tiepolo 11, Trieste, Italy
[54] INAF/IASF Bologna, Via Gobetti 101, Bologna, Italy
[55] INAF/IASF Milano, Via E. Bassini 15, Milano, Italy
[56] INFN, Sezione di Bologna, Via Irnerio 46, I-40126, Bologna, Italy
[57] INFN, Sezione di Roma 1, Università di Roma Sapienza, Piazzale Aldo Moro 2, 00185, Roma, Italy
[58] IPAG: Institut de Planétologie et d'Astrophysique de Grenoble, Université Joseph Fourier, Grenoble 1 / CNRS-INSU, UMR 5274, Grenoble, F-38041, France
[59] ISDC Data Centre for Astrophysics, University of Geneva, ch. d'Ecogia 16, Versoix, Switzerland
[60] IUCAA, Post Bag 4, Ganeshkhind, Pune University Campus, Pune 411 007, India
[61] Imperial College London, Astrophysics group, Blackett Laboratory, Prince Consort Road, London, SW7 2AZ, U.K.
[62] Infrared Processing and Analysis Center, California Institute of Technology, Pasadena, CA 91125, U.S.A.
[63] Institut Néel, CNRS, Université Joseph Fourier Grenoble I, 25 rue des Martyrs, Grenoble, France
[64] Institut Universitaire de France, 103, bd Saint-Michel, 75005, Paris, France
[65] Institut d'Astrophysique Spatiale, CNRS (UMR8617) Université Paris-Sud 11, Bâtiment 121, Orsay, France
[66] Institut d'Astrophysique de Paris, CNRS (UMR7095), 98 bis Boulevard Arago, F-75014, Paris, France
[67] Institute for Space Sciences, Bucharest-Magurale, Romania
[68] Institute of Astronomy and Astrophysics, Academia Sinica, Taipei, Taiwan
[69] Institute of Astronomy, University of Cambridge, Madingley Road, Cambridge CB3 0HA, U.K.
[70] Institute of Theoretical Astrophysics, University of Oslo, Blindern, Oslo, Norway
[71] Instituto de Astrofísica de Canarias, C/Vía Láctea s/n, La Laguna, Tenerife, Spain
[72] Instituto de Física de Cantabria (CSIC-Universidad de Cantabria), Avda. de los Castros s/n, Santander, Spain
[73] Istituto di Fisica del Plasma, CNR-ENEA-EURATOM Association, Via R. Cozzi 53, Milano, Italy
[74] Jet Propulsion Laboratory, California Institute of Technology, 4800 Oak Grove Drive, Pasadena, California, U.S.A.
[75] Jodrell Bank Centre for Astrophysics, Alan Turing Building, School of Physics and Astronomy, The University of Manchester, Oxford Road, Manchester, M13 9PL, U.K.
[76] Kavli Institute for Cosmology Cambridge, Madingley Road, Cambridge, CB3 0HA, U.K.
[77] LAL, Université Paris-Sud, CNRS/IN2P3, Orsay, France
[78] LERMA, CNRS, Observatoire de Paris, 61 Avenue de l'Observatoire, Paris, France
[79] Laboratoire AIM, IRFU/Service d'Astrophysique - CEA/DSM - CNRS - Université Paris Diderot, Bât. 709, CEA-Saclay, F-91191 Gif-sur-Yvette Cedex, France
[80] Laboratoire Traitement et Communication de l'Information, CNRS (UMR 5141) and Télécom ParisTech, 46 rue Barrault F-75634 Paris Cedex 13, France
[81] Laboratoire de Physique Subatomique et de Cosmologie, Université Joseph Fourier Grenoble I, CNRS/IN2P3, Institut National Polytechnique de Grenoble, 53 rue des Martyrs, 38026 Grenoble cedex, France
[82] Laboratoire de Physique Théorique, Université Paris-Sud 11 & CNRS, Bâtiment 210, 91405 Orsay, France
[83] Lawrence Berkeley National Laboratory, Berkeley, California, U.S.A.
[84] Max-Planck-Institut für Astrophysik, Karl-Schwarzschild-Str. 1, 85741 Garching, Germany
[85] McGill Physics, Ernest Rutherford Physics Building, McGill University, 3600 rue University, Montréal, QC, H3A 2T8, Canada
[86] MilliLab, VTT Technical Research Centre of Finland, Tietotie 3, Espoo, Finland
[87] National University of Ireland, Department of Experimental Physics, Maynooth, Co. Kildare, Ireland
[88] Niels Bohr Institute, Blegdamsvej 17, Copenhagen, Denmark
[89] Observational Cosmology, Mail Stop 367-17, California Institute of Technology, Pasadena, CA, 91125, U.S.A.
[90] Optical Science Laboratory, University College London, Gower Street, London, U.K.
[91] SB-ITP-LPPC, EPFL, CH-1015, Lausanne, Switzerland
[92] SISSA, Astrophysics Sector, via Bonomea 265, 34136, Trieste, Italy
[93] School of Physics and Astronomy, Cardiff University, Queens Buildings, The Parade, Cardiff, CF24 3AA, U.K.
[94] School of Physics and Astronomy, University of Nottingham, Nottingham NG7 2RD, U.K.
[95] Space Research Institute (IKI), Russian Academy of Sciences, Profsoyuznaya Str, 84/32, Moscow, 117997, Russia
[96] Space Sciences Laboratory, University of California, Berkeley, California, U.S.A.
[97] Special Astrophysical Observatory, Russian Academy of Sciences, Nizhnij Arkhyz, Zelenchukskiy region, Karachai-Cherkessian Republic, 369167, Russia
[98] Stanford University, Dept of Physics, Varian Physics Bldg, 382 Via Pueblo Mall, Stanford, California, U.S.A.
[99] Sub-Department of Astrophysics, University of Oxford, Keble Road, Oxford OX1 3RH, U.K.
[100] Theory Division, PH-TH, CERN, CH-1211, Geneva 23, Switzerland
[101] UPMC Univ Paris 06, UMR7095, 98 bis Boulevard Arago, F-75014, Paris, France
[102] Universität Heidelberg, Institut für Theoretische Astrophysik, Philosophenweg 12, 69120 Heidelberg, Germany
[103] Université de Toulouse, UPS-OMP, IRAP, F-31028 Toulouse cedex 4, France
[104] Universities Space Research Association, Stratospheric Observatory for Infrared Astronomy, MS 232-11, Moffett Field, CA 94035, U.S.A.
[105] University of Granada, Departamento de Física Teórica y del Cosmos, Facultad de Ciencias, Granada, Spain
[106] University of Miami, Knight Physics Building, 1320 Campo Sano Dr., Coral Gables, Florida, U.S.A.
[107] Warsaw University Observatory, Aleje Ujazdowskie 4, 00-478 Warszawa, Poland